Sedimentological, Structural and Geochemical Investigations of the Suevite of the Impact Crater Nördlinger Ries, Germany

D i s s e r t a t i o n

zur Erlangung des akademischen Grades

d o c t o r r e r u m n a t u r a l i u m
(Dr. rer. nat.)
im Fach Geowissenschaften

eingereicht am: 4.3.2011
im Fachbereich Geowissenschaften
der Freien Universität Berlin

vorgelegt von: Dipl.-Min., Dipl.-Chem.
Cornelia Meyer

1. Gutachter:	J.-Prof. Stephan van Gasselt
2. Gutachter:	Prof. Michel Jébrak
3. Gutachter:	Prof. Bruno Lafrance
3. Gutachter:	Prof. Falko Langenhorst

Tag der mündlichen Prüfung: 11.5.2012

Wer es einmal soweit gebracht hat, dass er nicht mehr irrt, der hat auch zu arbeiten aufgehört.
(Max Planck)

Prolog

Anmutig schlängelt sich die Straße durch die hügelige Landschaft der schwäbischen Alb. Umrahmt von Wäldern überquert sie kleine Flussläufe und die Idylle lässt nichts von der Katastrophe ahnen, die sich ganz in der Nähe abspielte. Doch plötzlich hat die Hochfläche ein Ende und die Straße führt 100 m tief in ein 24 km großes Loch. Kein Wald mehr. Nur vereinzelt wachsen ein paar Bäume auf weiten Feldern. Eine ringförmige Hügelkette im Inneren stellt den einzigen Kontrast zur eintönigen Landschaft dar. In einem dieser Hügel befinden sich die Ofnethöhlen. Vor diesen Höhlen saßen einst die Steinzeitmenschen und schauten in den Himmel, um dessen Schönheit zu bewundern, ohne zu wissen, dass ein Teil dessen, was sie über sich sahen, einst ihre einzigartige Landschaft formte. Was war passiert? Seit Anfang des 19. Jahrhunderts stellten sich Geologen genau diese Frage. Doch lange Zeit blieb die außergewöhnliche Rieser Landschaft ein Rätsel für die Geologen: “die Sphinx der europäischen Geologie”. Eugene Shoemaker reiste als Tourist in seinen Flitterwochen 1960 nach Nördlingen und läutete durch Zufall die kopernikanische Wende in den Geowissenschaften ein. Wie alle Touristen besuchte auch er den Daniel, den Kirchturm der St. Georgs Kirche in Nördlingen, der so berühmt ist für sein außergewöhnliches Baumaterial. Wie erstaunt muss Eugene Shoemaker gewesen sein, als er die Bausubstanz genauer betrachtete. Wo kam das Gestein her? Viele Sagen und Legenden rankten um den Turm. Und doch hatte er ähnliches Gestein schon einmal gesehen: in einem Meteoritenkrater. Als er den 15 km entfernten Steinbruch Otting sah, lag es vor ihm, das Rieser Geheimnis. In diesem grauen mit schwarzen Glasfetzen durchsetzten Gestein lag ein Schatz: Coesit, der Schlüssel zur Erkenntnis: das Nördlinger Ries - ein Meteoritenkrater.

Abstract

The processes of formation and transport of particles in suevite during impact crater formation remain poorly understood and are investigated at the 15 Ma old, 25 km wide Ries crater in southern Germany. The suevite of the Ries crater occurs in three different geological settings: 1) crater suevite in the central crater cavity inside the inner ring, 2) outer suevite on top of the continuous ejecta blanket, and 3) dikes in the crater basement and in displaced megablocks. For suevite genesis, the following processes have been discussed to-date in literature: 1) Fall-back of material into the crater and its periphery upon collapse of an ejecta plume, and 2) Horizontal transport of ejected material,akin to a) an impact melt flow, b) a pyroclastic flow, or c) initiated by phreatomagmatic explosion.

In order to differentiate between the two emplacement modes of fall-back and horizontal transport, the shape fabrics of suevite components from two localities outside the Ries crater were analyzed by fitting shape fabric ellipsoids to measured shape fabric ellipses and by applying high-resolution X-ray computed tomography to analyze the three-dimensional shape and orientation of the suevite particles. It could be shown that the preferred orientation of long axes of elongate particles is aligned either radially or concentrically with respect to the crater center. These observations indicate that suevite material was not only derived from an ejecta plume but was transported by lateral flow under viscous conditions, upon fall-back, similar to pyroclastic flows.

For the further differentiation of this emplacement mode the grain shape, grain size distribution, and content of particles in several drill core sections inside and outside the crater were investigated. These stereometric results imply a secondary comminution process after the shock wave passage, pressure release, and transient cavity formation, where the clasts will be comminuted and sorted as a function of their size, density, and distance to the crater center, and where particle-particle interactions could occur. A secondary milling and sorting process in a gas dominated suspension seems to be reasonable. Only the upper most portion of the inner crater suevite seems to be have fallen out of the ejecta plume.

Today, the hydrothermal formation of the suevite matrix is widely accepted. However, which primary material was transformed into the clayey matrix is still a matter of discussion. On one hand, finely comminuted gneiss, small glass particles, or condensates from vaporized crystalline rocks are proposed as source materials of the suevite matrix. On the other hand, the suevite matrix is interpreted as original impact melt, which would explain the lacking impact melt in the crater. This work compares the chemical composition of the melt particles of suevites at the four different suevite drill cores with their corresponding matrix to identify the original composition of the suevite matrix. Finally, the primary melt content of the Ries suevite is estimated. The results show that the suevite can be distinguished in the following subunits: 1) Strongly altered suevite, with similar melt and matrix composition, 2) Inhomogeneous suevite, with differentiation in K-poor and K-rich melt with either silicate matrix similar in

chemistry to the melt or non existing silicate matrix, 3) Chemical homogeneous suevite, with similar melt and matrix composition, which can be considered as original impact melt, and 4) Chemical homogeneous suevite, with different melt and matrix composition. The volume of the impact melt of the Ries crater is estimated to be $\sim$4 km^3, which is still less compared to impact craters similar in size to the Ries crater.

The following five stages can be distinguished for the formation and deposition of the Ries suevite: 1) An early ejecta plume, mainly composed of projectile and sediments, is formed during the excavation stage and is deposited as a < 2 m thick layer inside and outside the crater on top of the Bunte Breccia after crater formation, 2) After a hiatus, the interaction of surface water and/or ground water with the impact melt lake induce a phreatomagmatic explosion of the upper melt lake, 3) A basal, non erosive pyroclastic surge, initiated by the explosion, moves radially outward and is deposited as the first suevite deposition inside and outside the crater, 4) At the same time an ejection column rises. After its collapse, a pyroclastic flow is initiated which propagates to the crater margin and is superimposed as a second suevite layer, partially covering the first deposited suevite layer, 5) The collapse of the ejection column creates contemporaneously an upward rising ejecta plume, where accretionary lapilli are formed. Finally, these lapilli, together with the residual plume material, are deposited in the inner crater a) into an existing water layer, or b) reworked by incoming water in the crater at a later time.

Zusammenfassung

Die Prozesse die zur Bildung und zum Transport der Partikel im Suevit während der Impaktkraterbildung führen, sind bisher wenig verstanden und wurden an dem 15 Ma alten Rieskrater in Süddeutschland untersucht. Den Suevit des Rieskraters findet man in drei verschiedenen geologischen Anordnungen: 1.) den Kratersuevit in der zentralen Kraterhohlform innerhalb des inneren Rings, 2.) den äußeren Suevit, der die Bunte Brekkzie überlagert, und 3.) Gänge im kristallinen Untergrund und umgelagerten Megablöcken. Folgende Prozesse sind bisher im Zusammenhang mit der Suevitgenese diskutiert wurden: 1.) Rückfall von Auswurfsmaterial in den Krater und dessen Umgebung nach dem Kollabieren der Ejektionswolke, 2.) lateraler Transport von Auswurfsmaterial a) in einem Schmelzfluss, b) in einem pyroklastischen Strom, und c) ausgelöst durch eine "phreatomagmatische" Explosion.

Um zunächst zwischen den beiden Ablagerungsmechanismen Rückfall und lateraler Transport zu unterscheiden, wurden die Formgefüge der Suevitkomponenten aus zwei Lokalitäten außerhalb des Rieskraters bestimmt. Formgefügeellipsoide wurden hierfür aus Formgefügeellipsen berechnet und hochauflösende Röntgencomputertomographie auf die Suevitproben angewandt, um die dreidimensionale Form und Orientierung der Suevitpartikel zu bestimmen. Dabei konnte gezeigt werden, dass die Hauptachsen der länglichen Suevitpartikel bevorzugt radial oder konzentrisch zum Kraterzentrum orientiert sind. Diese Anordnung lässt darauf schließen, dass die Suevitpartikel nicht einzig allein aus dem Rückfall einer Ejektionswolke stammen, sondern nachdem Rückfall weiter horizontal unter viskosen Bedingungen transportiert wurden sind, ähnlich einem pyroklastischen Strom.

Um diesen Prozess weiter zu differenzieren, wurden daraufhin verschiedene Bohrkerne innerhalb und außerhalb des Rieskraters auf Kornform, Korngrößenverteilung und Anteil der Suevitkomponenten untersucht. Die stereometrischen Ergebnisse implizieren einen sekundären Zerrüttungsprozess der Suevitkomponenten nach Stoßwellendurchgang, Entlastung und transienter Kraterbildung. Es handelt sich hierbei um einen Prozess, in dem die Komponenten zermahlen sowie nach Größe, Dichte und Abstand zum Kraterzentrum sortiert werden, ein Prozess in dem Partikel-Partikel-Interaktionen vorkommen. Ein sekundärer Zermahlungs- und Sortierungsprozess in einer gasdominierten Suspension scheint hierbei am plausibelsten. Nur die obersten Meter des Suevits im inneren Krater stellen offensichtlich das Rückfallprodukt aus der Ejektionswolke dar.

Die hydrothermale Überprägung des Suevits nach seiner Ablagerung ist heute weitestgehend akzeptiert. Jedoch welches Ausgangsmaterial zur Bildung der tonmineralhaltigen Matrix führte, wird noch immer kontrovers diskutiert. Zermahlene Gesteine und feine Glaspartikel werden einerseits als Ausgangmaterial vorgeschlagen, andere interpretieren die Suevitmatrix als ursprüngliche Impaktschmelze und erklären damit den ungewöhnlich niedrigen Anteil an Impaktschmelze im Rieskrater. In der vorliegenden Arbeit wurde die chemische Zusammensetzung der Schmelzpartikel in den Sueviten der verschiedenen Riesbohrkerne und ihrer

zugehörigen Matrix bestimmt, um deren ursprüngliche Zusammensetzung zu identifizieren. Zusätzlich konnte der Schmelzanteil der Suevite vor der Alteration abgeschätzt werden. Es zeigt sich, dass die Suevite chemisch in folgende Untereineiten aufgeteilt werden können: 1.) stark alterierter Suevit mit gleicher Schmelz- und Matrixzusammensetzung, 2.) inhomogener Suevit mit Differentiation in K-arme und K-reiche Schmelze und entweder chemisch ähnlicher oder nicht vorhandener silikatischer Matrix, 3.) chemisch homogener Suevit mit gleicher Schmelz- und Matrixzusammensetzung, der als ursprüngliche Impaktschmelze betrachtet werden kann, und 4.) chemisch homogener Suevit mit unterschiedlicher Schmelz- und Matrixzusammensetzung. Das Volumen an Impaktschmelze im Krater konnte auf $\sim$4 km^3 neu abgeschätzt werden, liegt dabei aber immer noch deutlich unter dem Schmelzvolumen größenvergleichbarer Krater.

Die folgenden fünf Prozesse können aus den oben dargestellten Ergebnissen schlussfolgernd für die Bildung und Ablagerung der Riessuevite unterschieden werden: 1.) eine frühe Ejektionswolke, vorrangig zusammengesetzt aus Projektil und Sedimenten, bildet sich während der Exkavationsphase und lagert sich nach der Kraterbildung als eine $<$ 2 m dicke Schicht im Krater und außerhalb des Kraters auf der Bunten Brekkzie ab, 2.) die Interaktion von Oberflächenwasser und/oder Grundwasser mit dem Impaktschmelzsee führt nach einem Hiatus zur phreatomagmatischen Explosion des oberen Impaktschmelzsees, 3.) ein durch die Explosion erzeugter basaler, nicht erosiver Dichtestrom bewegt sich radial aus dem Krater heraus und lagert sich als erste Suevitlage im Krater und außerhalb des Kraters ab, 4.) gleichzeitig steigt eine Ejektionssäule auf, die nach ihrem Kollabieren einen pyroklastischen Strom erzeugt, der sich maximal bis zum Kraterrand fortpflanzt und als zweite Suevitlage die erste Lage teilweise überlagert, 5.) das Kollabieren der Ejektionssäule erzeugt gleichzeitig eine aufsteigende Ejektionswolke, in der sich akkretionäre Lapilli bilden, die sich zusammen mit dem restlichen Wolkenmaterial anschließend im inneren Krater entweder a) auf eine bereits bestehende Wasserschicht ablagern oder b) zu einem späteren Zeitpunkt durch in den Krater einfließendes Wasser aufgearbeitet und aus dieser Wassersäule neu abgelagert werden.

Contents

List of Figures

List of Tables

1. Organization of the thesis and aims of the study

1.1. General preface

This thesis presents sedimentological, structural, and geochemical studies of suevites from the Ries crater, Germany. The thesis starts with an overview about the impact cratering process, in general, followed by the formation process of the Ries crater, in detail. The structure of the Ries crater is explained and several theories of suevite formation are introduced. A deeper insight into numerical modelling of the genesis of the suevite is given.

This work resembles a semi-cumulative thesis, where Chapter 4 represents a manuscript that is accepted for publishing in GSA Bulletin

Meyer, C., Jébrak, M., Stöffler, D., Riller, U. Lateral transport of suevite inferred from 3D shape fabric analysis: evidence from the Ries impact crater, Germany. GSA Bulletin, Vol. 123, 2312-2319.

and Chapters 5 and 6 will be submitted to impact-related journals which ones not have been decided yet. Thus, Chapters 4 to 6 have their own introduction, methodology, discussion, and conclusion. According to publication standards, methodologies are described completely in few words. The sample description of these chapters is contained to Chapter 3. Comparable to a monograph, all processed data are contained in Appendix 1 to 6 and in Chapter 7, all results are summarized through a new definition of the suevite subunits of the Ries crater and the genesis of the Ries suevite is reconstructed.

Chapter 4 is the first application of X-ray computed tomography and of 2D shape fabric ellipsoid fitting to investigate the shape-preferred orientation of breccia components, in general, and impact breccias, in particular. Photo prints of this paper were produced by A. Dittmann (MfN). L. Harris (Institut National de Recherche Scientifique-Eau-Terre-Environnement (INRS-ETE), Québec City, Canada) assisted with the X-ray computed tomography. Image analyses, data processing, text, and interpretation were performed by the author. The processing of the data was carried out by using standard image processing software (Adobe Photoshop, Adobe Illustrator, ImageJ), StereoNett, XACT, MS Excel, and MatLab. Methods

and results were discussed with Michel Jébrak and Ulrich Riller. Venetia Bodycomb and Ulrich Riller helped with English correction.

Due to discordances with the former supervisor of the thesis Chapter 5 and 6 not have been submitted yet. Thin sections were prepared for these parts of the thesis by R. Knöfler (Museum für Naturkunde, Berlin (MfN)) and photo prints were produced by H. J. Götz, A. Dittmann (MfN) and the author. J. Jacob (MfN) helped with the thin section templates for stereometric analyses. K. Born and P. Czaja (MfN) assisted with the electron microprobe (EMPA) and scanning electron microscopy (SEM) measurements. All scanning electron microscopy imaging and mapping, optical microscopy, image analyses, text, and interpretation were performed by the author. The processing of the data was carried out by using standard image processing software, MS Excel, and MatLab. Richard Grieve helped with English correction.

The drill core FBN73, Wörnitzostheim, and Otting are stored at the ZERIN (Zentrum für Rieskrater- und Impaktforschung Nördlingen) in Nördlingen, Germany. The drill core Enkingen is stored at the Bayrisches Geologisches Landesamt in Munich, Germany.

This thesis was prepared at the Museum für Naturkunde, Berlin, and was supported by the Deutsche Forschungsgemeinschaft (RE 528/4-1).

1.2. Aims of the study

The mass flux of impact ejecta is difficult, or even almost impossible, to quantify due to the fact that the formation of impact craters, except for impact experiments (e.g., Schultz 1987, Kenkmann et al. 2010), is not witnessed. Hence, sedimentological, geochemical, structural and numerical modelling studies of the ejecta deposits are the principal means of understanding the ejection dynamics. To understand impact processes and the history of their ejected materials, it is essential that reworking, which likely affects the clast population, is considered and understood. The clast population of impact ejected material typically comprises particles with extremely diverse shapes, sizes, and densities (e.g., Wittmann et al. 2004, Reimold et al. 2009, Pohl et al. 2010). Transport and sedimentation of these particles probably result in sorting and progressive deposition and in grain size and shape modification, as observed in comparable sedimentological transport systems (Kokelaar and Romagnoli 1995). The original ejected clast shapes are no longer recognizable due to transportation processes.

Thus, the goal of this work is to study the clast populations of the Ries suevite geochemically, structurally and sedimentologically. The reworking, sedimentation and alteration processes of the lithic clasts and melt particles of the suevite is indicated and discussed. Conclusions regarding the formation, transport, and deposition of the Ries suevite are drawn from the obtained results and the role of the ejecta plume in the genesis of the suevite is illustrated.

2. Introduction into impact cratering

2.1. Crater formation process

The formation of impact craters is a fundamental process in the solar system. The results of the cratering process have been documented on Earth as well as on neighboring planets and moons. Impacts are inseparably connected to the history of our home planet. Four point five billion years ago the proto-Earth collided with a planet of approximately Mars-size and formed the Moon (Stevenson 1987), which is a main supporter of the life promoting climate on Earth. Large-scale impacts influenced negatively the biological evolution with the initiation of mass extinctions. Sixty five million years ago, at the Cretaceous-Tertiary boundary, 50% of all animal species died, including the dinosaurs, triggered by a meteorite impact on the Yucatan peninsula in Mexico (Alvarez et al. 1980). In addition, some authors have suggested that the hydrotherm system related to the impact cratering process could have been the source of new life (e.g., an overview is given by Cockell and Lee 2002). However, a notable part of solid material was ejected into the space during the Cretaceous-Tertiary event. Under assumption that terrestrial rocks are inhabited by microorganisms, beside the mass extinction, this event could have provide a population of the materials to space with terrestrial microorganisms (Mileikowsky et al. 2000, Meyer et al. 2011). Hence, the impact process is not only fundamental for the formation of the planets but also for the cycle of life.

For an understanding of crater formation processes, the following methodologies have been used:

1. Field investigations (e.g., an overview about the Nördlinger Ries is given by e.g., Kring 2005;

2. Remote sensing of impact craters (e.g., on Moon and Mars (Hartmann and Neukum 2001));

3. Shock and cratering experiments (e.g., Stöffler 1975; Schultz 1987);

4. Numerical Modeling (e.g., Ivanov 2005; Wünnemann et al. 2005).

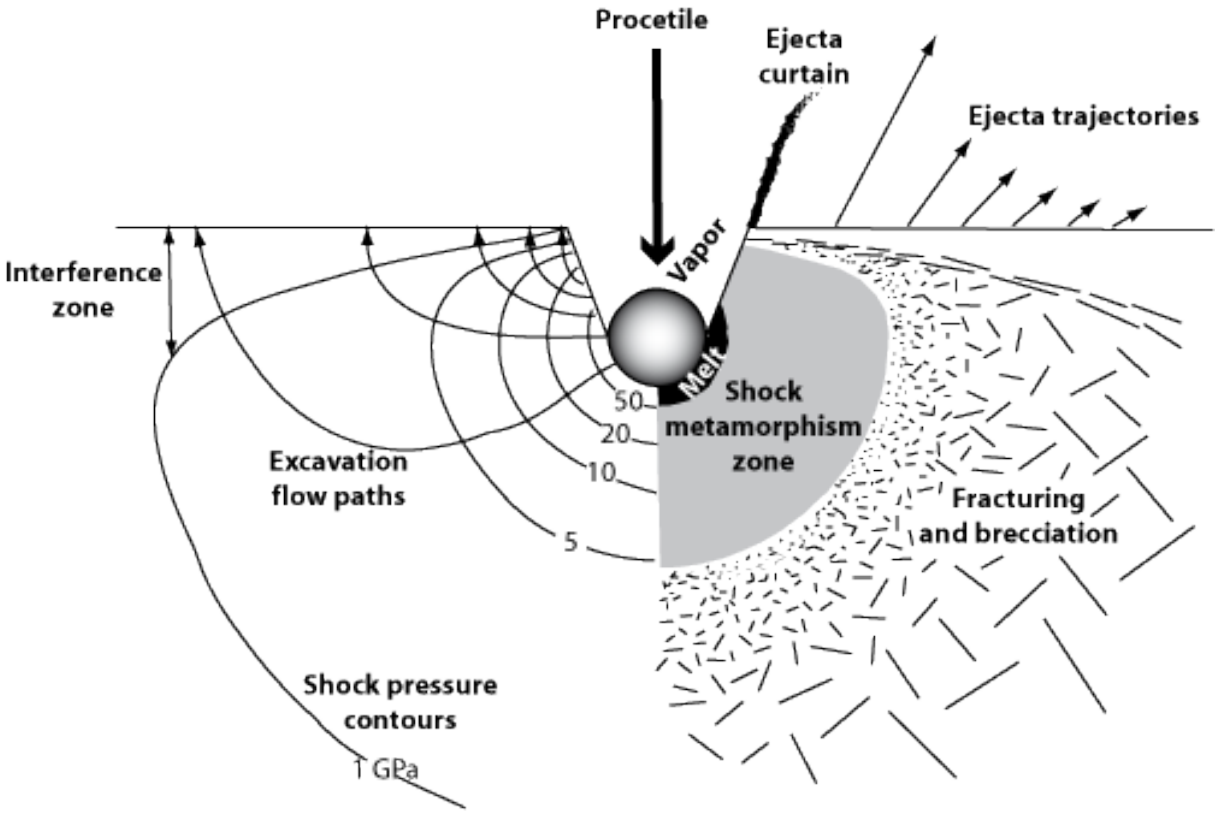

Fig. 2.1.: Schematic illustration of the contact - and compression stage during impact crater formation: Initial shock pressure and excavation flow lines around impact point. Pressure contours are approximately hemispherical and grade outward from vapor to melt to the limit of crushing. Near the surface, in the interference zone, rarefraction reduce the maximum pressure. After penetrating about two diameters into the target the projectile has been almost completely converted to melt and vapor (modified from Melosh 1989)

2.1.1. Contact and compression phase

The first phase of the crater formation process is the contact and compression phase. A cosmic projectile (asteroid or comet), which is large and stable enough to penetrate the Earth's atmosphere, hits the target at almost its original cosmic velocity. Due to the impact velocity being supersonic, a shock wave is generated and propagates radially from the impact point into the target. The projectile penetrates another one to two times its own diameter into the target, until it transformed all its kinetic energy into shock wave energy. The expanding shock wave interacts with the target. By heating, deformation, and displacement of the target material, the peak shock pressure (>100 GPa) decreases exponentially with distance from the crater center. The duration of the so-called compression stage (several seconds at a maximum) is determined by the size of the projectile. As soon as the shock wave reaches the back side of the projectile, a refractory wave is reflected into the projectile that cancels the high shock pressures. Because of the high shock pressures and corresponding shock temperatures inside the projectile, the shock wave passage results in the complete melting and vaporizing of the projectile. The refractory wave continues to propagate into the target and also cancels the shock pressure inside the target. The physical consequences of the shock

wave can be observed in the irreversible deformations in the rock-forming minerals e.g., as planar deformation structures and high pressure polymorphs (Melosh 1989, Stöffler and Langenhorst 1994, Grieve et al. 1996, French 1998), (Fig. 2.1)

2.1.2. Excavation stage

During the interaction of the expanding shock wave with the target a hemispherical cavity starts to open. The shock wave, which starts from the center of the cavity and reaches the surface of the target, will also be reflected as a refractory wave in the target. The near-surface rocks are broken and due to the transformation of shock energy, i.e. into kinetic energy, they are accelerated outwards. The outward ejection of this material leads to the formation of the transient cavity. The material of the upper layer of the transient crater will be ballistically ejected exceeding the rim of the later final crater. In the lower units of the transient crater, the refractory wave is not strong enough to eject material. The latter broken material inside the target moves downwards and outwards. Both zones propagate further accompanied by elevation of the near surface rock to form the transient crater rim. The formation of the transient crater is finished once the shock and refractory waves stop ejecting or moving material (Melosh 1989, French 1998). Together with broken material from the crater, the projectile forms an upwards rising ejecta plume which extends hemispherically outwards (Pierazzo et al. 1998). The time of the excavation stage varies from several seconds to several minutes, depending of the crater size (Fig. 2.2).

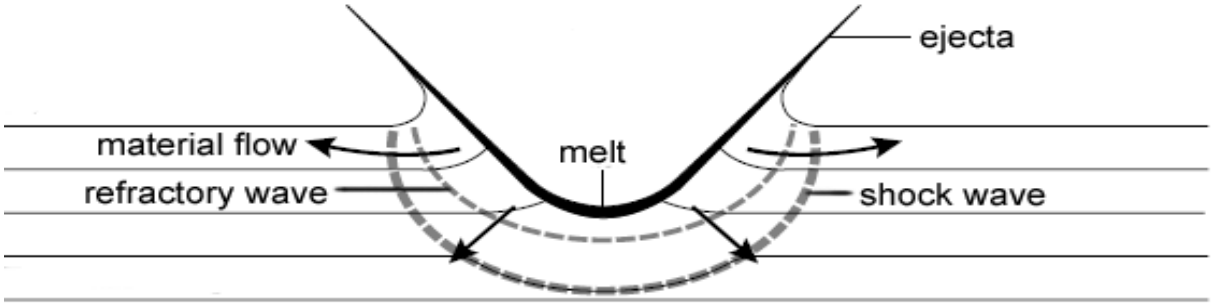

Fig. 2.2.: Schematic illustration of the excavation stage during impact crater formation: Interactions of the shock wave, surface, and the refractory wave produce an outward excavation flow that opens up the transient crater. In the upper part, target material is fractured, excavated, and ejected beyond the transient crater rim. In the lower part, target material is driven downward and outward (modified from French, 1998).

2.1.3. Modification stage

The transient crater is modified by gravitation. The crater collapse forms the final crater structure. Simple craters are formed by debris sliding down along the transient crater rim and walls into the crater. Large transient craters have to compensate gravitational instability and

their collapse includes the slumping of the transient cavity walls and the elastic rebound of the crater floor. Complex craters with central peaks, annular troughs, and terraced walls are produced. The central peak itself can collapse and form an annular ridge inside the crater. On Earth, the transition from simple to complex craters occurs between 2 and 4 km final crater diameter, depending on the target material (Melosh 1989, French 1998, Wünnemann and Ivanov 2003), (Fig. 2.3).

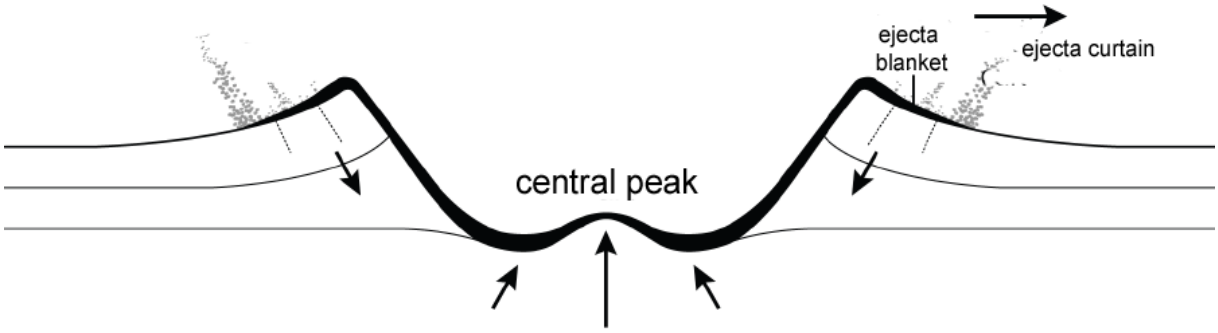

Fig. 2.3.: Schematic illustration of the modification stage during impact crater formation: Oversteepened walls of transient crater collapse back into cavity as well as near-crater ejecta. Large transient craters additionally compensate the gravitational instability by an elastic rebound of the crater floor (modified from French, 1998).

2.2. The Ries crater

The 15 Ma old, 25 km diameter Ries impact structure in southern Germany ($48°53'N, 10°37'E$) is unique in its preservation, in comparison to other large impact structures on Earth. In particular, the excellent preservation of suevites provides an important tool for understanding the dynamics of impact ejection, in general and the dynamics of ejection material, in particular.

2.2.1. Formation and structure of the Ries crater

The Nördlinger Ries was formed by a 1.1 to 1.5 km large meteorite, probably of achondritic composition, by an oblique impact (Stöffler et al. 2002; Wünnemann et al. 2005, Morgan et al. 1979). The stratigraphy of target material at the impact point consists of a 620 - 750 m thick sediment layer of Permian to Tertiary materials. This is underlain by ca. 320 million year old crystalline basement rocks, composed of granites, gneisses, and amphibolites (Hüttner and Schmidt-Kaler 1999, Graup 1977). Shortly before impact, in the upper Tertiary, the sediment layer was strongly eroded by numerous rivers crossing the former Ries area from NW to SE (Gall et al. 1977).

The Ries crater belongs to the class of complex craters with an inner ring composed of rocks from the crystalline target Fig. 3.1. The inner ring is surrounded by a mega-block zone, with up to 1 km large blocks of sedimentary or crystalline origin, followed by the tectonic

crater rim. A polymict lithic breccia, which is composed of clastic material of all stratigraphic units (Bunte Breccia), overlies the mega-block zone and continues radially out to a distance of 45 km from the crater center. Up to a distance of 23 km from the crater center the Bunte Breccia is sporadically overlain by suevite deposits from several meters to tens of meters in thickness. In the inner crater, the suevite overlies the crystalline basement with a thickness of 300 - 400 m. Impact melt rocks can be found as isolated meter-sized blocks or as melt fragments in the suevite. Lake sediments of the post-impact crater lake overly the ejected material inside the crater (Pohl et al. 1977), Fig. 3.1.

According to Wünnemann et al. (2005), the transient crater cavity reached a maximal depth of 5 km and 10 - 12 km in diameter. Due to the following gravitational collapse, the Ries crater achieved its present-day size of 25 km in diameter. The gravitational rebound of the crater floor resulted in the upwards movement of the crater floor and the formation of the inner ring. The modification stage of the Ries crater was finished after 120 s. Furthermore, in their model, Wünnemann et al. (2005) suggest a 200 m thick impact melt layer on the crater floor.

2.2.2. Models of suevite formation

Suevite is a "polymict impact breccia with particulate matrix containing lithic and mineral clasts in all stages of shock metamorphism including cogenetic melt particles, which are in a glassy or crystallized state" (Stöffler and Grieve 2007). The Ries suevite consists mainly of lithic clasts and melt particles derived from the crystalline basement, with the sediment content of the Ries suevite amounting to just a few percent. The suevite of the Ries crater occurs in three different settings:

1. As crater suevite inside the inner ring,
2. As outer suevite outside the inner ring deposited on top of the Bunte Breccia, and
3. As dike suevite in the crater basement and in displaced crystalline mega-blocks (Stöffler et al. 2009).

Although suevite deposits have been studied extensively (e.g., Hörz 1965; Förstner 1967; Stöffler et al. 1977; von Engelhardt et al. 1995; Wittmann et al. 2004; Stöffler et al. 2004), there is no consensus as to their formation, particularly regarding their genetic relationship to ejecta plumes. In particular, the mechanisms of transport of particles in the suevite remain poorly understood.
In the literature, four different kinds of transport processes have been discussed:

1. The hypervelocity meteorite impact into the solid target leads to instantaneous vaporization, melting, and comminution of target rocks in the central excavation cavity. A

substantial portion of this cavity will immediately become engulfed in an upward-rising plume composed of shocked solid matter, melt, and vapor (Pierazzo and Melosh 2000). Upon collapse of this ejecta plume, the plume material falls back into the crater and also covers ballistically ejected material outside the crater, collectively forming suevite (e.g., Stöffler 1977; von Engelhardt and Graup 1984; von Engelhardt 1997).

2. Horizontal transport of ejected material:

2a. Suevite is formed by series of unmixed impact-generated melts resulting from different target lithologies, which were still molten at the time of, and after deposition. These melts were emplaced as ground-hugging impact melt flows that emanated from central uplift, during the modification of the transient crater (Osinski et al. 2004).

2b. At least the outer suevite was transported predominantly horizontally. This transport occurs in the form of a suevitic flow similar to a pyroclastic flow (Newsom et al. 1986, 1990; Bringemeier 1994).

2c. Artemieva et al. (2009) also concluded that the suevite has to be transported by a kind of pyroclastic flow. However, the amount of natural volatiles in the melt is too low to initiate such a flow. Hence a "melt-coolant-interaction", similar to a phreatomagmatic explosion, has to occur to trigger such a flow, with the explosive efficiency depending on the volatile-melt ratio. Artemieva et al. (2009) suggests that incoming surface water (particulary from rivers), after the crater formation process, could be the initiating medium.

2.2.3. Numerical modeling to the genesis of suevites

Artemieva et al. (in preperation) modeled the Ries impact process to get insights in the formation of the suevite. Initial conditions were a 600 m thick cover layer of calcite mixed with water underlain by granitic rocks. The projectile was assumed to be a 1.1 km diameter stone meteorite, impacting the target at 18 km/s.

The results of the numerical modeling show that the ejecta plume is mainly composed of sediment particles and projectile material, with a minor fraction of crystalline material and melt. After the deposition of the ejecta plume, these particles form a layer of 1 - 2 m thickness of fine grained material. Under the assumption that the upwards rising ejecta plume could also carry larger blocks and collapse, after 150 s at the latest, the thickness of the deposited suevite could increase to 10 m.

Furthermore, at the end of the modification stage, the numerical model predicts a crater floor covered by a thick layer of impact melt, which has the same thickness of today's crater suevite. How could the melt lake transform into suevite? The idea of a phreatomagmatic

explosion, the explosive interaction of the melt lake with water, can explain a small percentage of the transformed impact melt (Artemieva et al. in preperation). For the solution to this problem, the numerical modeling sets boundaries for the moment and field observations have to be performed to find a satisfying answer.

3. Samples and their geological settings

Samples for this work have been obtained from four cores drilled through the suevite inside and outside of the Ries crater (Fig. 3.1)

1. “Nördlingen 1973” (FBN 73), 3.5 km from the crater center, with a 300 m thick suevite sequence,
2. “Enkingen” (SUBO 18), 5 km from the crater center, with a 65 m thick suevite sequence and a 13 m thick section of an impact melt rock,
3. “Wörnitzostheim”, 8 km from the crater center, with an 80 m thick suevite sequence, and
4. “Otting”, outside the crater, 17 km from the crater center, with 9 m of suevite.

In contrast to most of the other drill cores of the Nördlinger Ries, the four selected ones are all characterized by the fact that the suevite sequence is drilled through completely. The drill cores FBN 73 (drilled in 1973) and Wörnitzostheim (drilled in 1965) have been extensively described in papers in Geologica Bavarica 72 (1974),75 (1977) and Förstner (1967), Dressler and Graup (1974), respectively. On the contrary the Otting core was drilled in 1976 and, although the Bunte Breccia of the core was studied by Chao et al. (1977), the suevite of the drill core has not yet been investigated in detail. After the 70’s, studies of the Ries suevite were continued almost exclusively on the numerous suevite outcrops inside and outside the crater. Due to the fact that the analytical methods for drill core analyses have significantly improved, since 1970’s a reinvestigation of the drill core by using of modern methods appears in order. The most recent drill core of the Ries crater is the 100 m drill core of Enkingen, drilled in November-December 2006. Until now, an overview about this drill core is only given by Pohl et al. (2010).

All sampled half cores and thin sections are listed in Table 3.1.

Samples from the suevite quarries are from “Aumühle”, 11 km from the crater center to NE, and from “Seelbronn”, 17 km from the crater center to SW. The suevite quarries are situated at the crater rim and outside the crater and are the only ones in operation hosting suevite.

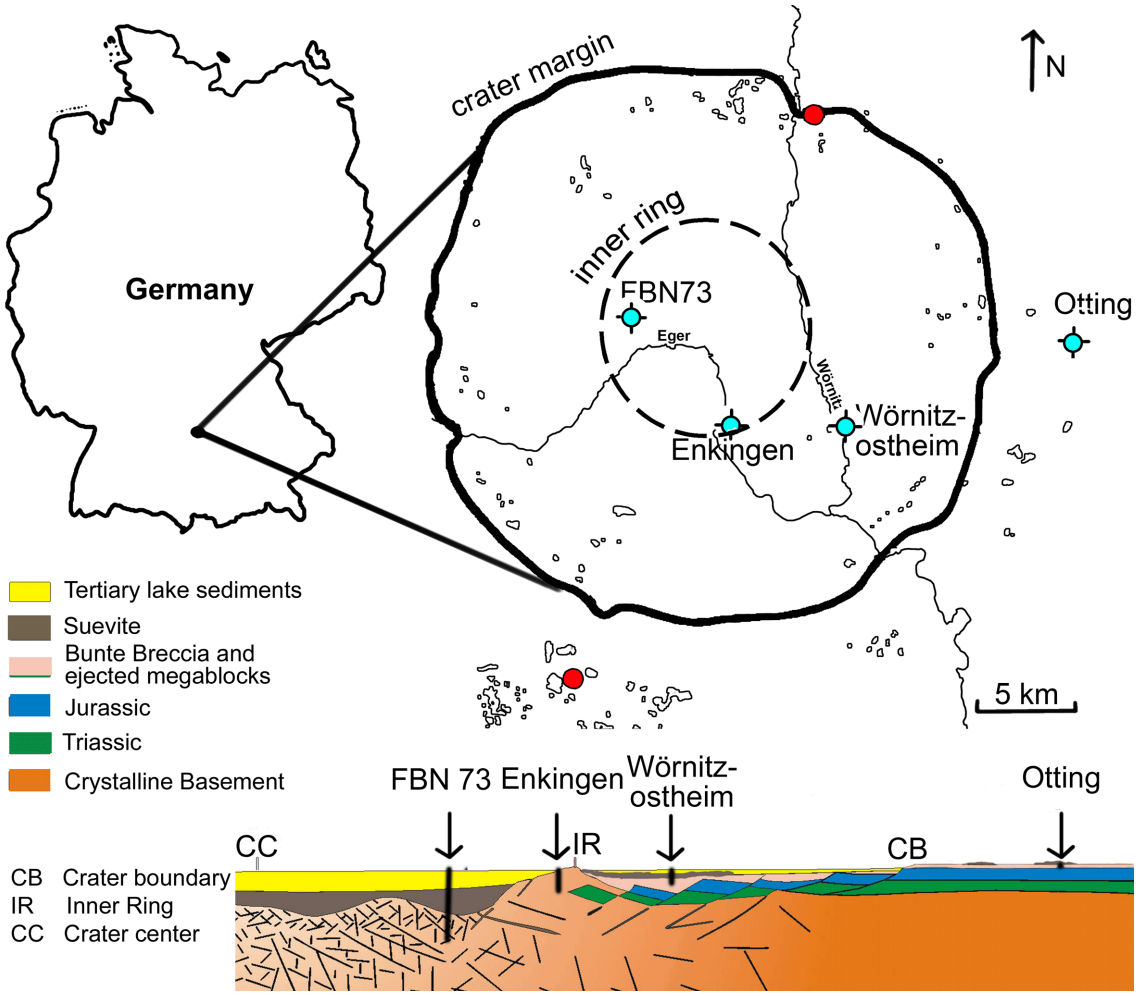

Fig. 3.1.: Location of drill cores (blue circles) and suevite quarries (red circles) with respect to inner ring and crater boundary of the Ries crater. Patch-like suevite occurrences are shown as outlines (according to Hüttner and Schmidt-Kaler 1999); stratigraphic profile according to Pohl et al. (1977); FBN73 = research drilling of Nördlingen 1973.

Table 3.1.: List of analyzed suevite samples for image analysis. Numbers showing depth of drill core in [m], depth represents the center of a 10 cm wide sample, * analyzed by SEM (Scanning electron microscopy).

FBN73		Enkingen		Wörnitzostheim		Otting	
half cores	thin sections	half cores	thin sections	half cores	thin sections	half cores	thin sections
	294.4*	22.6		16.4	16.4*	0.3	0.3*
296.5	296.5		25.7*		18.1*	0.8	
300.9	301.4*		30.7	19.2		1.3	1.3*
304.8	304.8*	33.9	33.8*	21.8		1.8	1.8*
307.4	307.4*	38.5		22.6		2.3	2.3*
309.1	309.1*	39.3		22.7	22.7*	2.7	2.8*
309.5		39.6		25.2	25.2*	3.2	3.2*
314.0		40.5	42.3	26.0		3.8	3.8*
	318.1*	43.8	43.7	29.5	29.5*	4.3	4.2*
	319.3*	49.8	49.7*	30.2		4.7	4.7*
	320.0*	50.6		32.0		5.3	5.3*
321.1	321.1*	52.4	53.9	33.2	35.5*	5.7	5.8*
	321.4*	55.9		35.5		6.3	6.3*
323.9	323.3*	56.5		36.9		6.7	
325.0	325.0	58.2	58.9	38.9	39.8*	7.3	7.2*
326.3		59.3		39.8		8.2	8.0
327.3	327.0*	60.8		41.4			8.1*
328.3	328.9*	62.6		44.3	45.6*	8.8	8.7*
329.7	329.7*	63.1	63.1	45.6			
330.6		64.2		46.4			
330.8	*	65.9		47.5			
332.7		66.8	66.6*	49.2	51.0*		
334.6	334.6*	67.6		51.0	57.8*		
336.2		68.5	68.0	57.3			
343.5		69.5		60.5	65.8*		
352.1		70.3		65.8			
360.3	360.3*	72.3	71.8	68.7	72.3*		
362.8		73.9	73.8		77.4*		
372.2		75.4		77.4	80.5*		
378.6	378.5*	76.7		83.3			
380.4	380.4*	77.9		84.2	86.3*		
382.1		79.2	78.8*	86.8			
405.1		80.1	80.8	87.6			
410.2		81.2		88.3			
418.2		82.1	82.4*	90.2	91.9*		
436.2		83.1		91.9	95.2*		
447.1		84.1		95.2	98.4*		
457.4		85.2	85.1	98.5			
467.2	465.1*	86.1					
477.2		87.1					
487.1	485.1*	88.4					
499.7	495.3*	89.3					
505.6		90.2					
516.6	516.1*						
521.1	525.4*						
532.5	531.5*						
546.5							
550.1	550.1*						
551.1							
568.4	569.1*						
596.5	596.4*						
601.9	601.9*						
642.5	642.9*						

3.1. Samples from suevite quarries

The suevite of the surface outcrops and quarries of the Ries crater consists of centimeter to decimeter large lithic clasts and melt particles embedded in a fine grained matrix. This suevite variant is devoid of sorting or layering and on average consists of 15.8 % melt particles, 79.5 % groundmass, 4.3 % crystalline rock fragments, and 0.4 % sedimentary rock fragments (von Engelhardt et al. 1995). The groundmass consists of melt particles, mineral and rock fragments embedded in a matrix of mainly montmorillonite (von Engelhardt and Graup 1984; von Engelhardt et al. 1995). The preferred orientation of elongate melt particles of the outer suevite is visible in hand samples.

For this study, oriented suevite samples from Aumühle and Seelbronn quarries were taken. In both localities suevite overlies the "Bunte Breccia". The contact between the two breccia deposits is well defined, but may be gradational over a distance of a few centimeters (Hüttner and Schmidt-Kaler 2003) and varies in orientation from horizontal to sub-vertical. At the base of the suevite unit, melt particles are quenched and smaller in size than particles of the overlying suevite deposits (von Engelhardt et al. 1995). The presence of degassing pipes in the suevite, the overall uniform texture of the suevite, and the obviously non-erosive base of the suevite unit suggest that the suevite was deposited almost instantaneously and derived from a turbulent gas-rich medium (Newsom et al. 1986).

3.2. Drill core samples

3.2.1. Research drilling Nördlingen 1973 (FBN 73)

The core stratigraphy of the FBN 73 drill core is based on papers in Geologica Bavarica 75 (1977) and involves, from top to bottom: sediments of the Ries crater lake from 0 to 314 m, graded suevite from 314 to 331 m, melt-rich suevite from 331 m to 520 m, and melt-poor suevite from 520 to 602 m, underlain by crystalline basement rocks intersected by breccia dikes (Fig. 3.2).

Upper sedimentary unit (256 - 314 m):

Füchtbauer et al. (1977) and Jankowski (1977a) considered the drill core section from 256 m to 314 m (unit A) as a basal unit of the Palaeogene lake sediments, which contains suevitic components produced by reworking of suevite deposited outside the inner crater. This unit is composed of sedimentary cycles, where the cycles become coarser grained, less rounded and less sorted with depth. Coarse grained sections of suevitic composition are overlain by finer grained dolomitic and calcitic layers in each cycle. The lowermost cycle from 307 to 314 m is, in mineral composition, consistent with underlying so-called graded suevite and is interpreted

as the result of irregular and local water flows (Jankowski 1977a). A layer with accretionary lapilli occurs at 309 m inside this cycle. Former melt particles are transformed to analcime and montmorillonite (Jankowski 1977a). An additional suevitic layer, with accretionary lapilli, was encountered at 296 m.

Graded suevite (314 - 331 m):

The so-called graded suevite between 314 and 331 m was interpreted as fall-back material by Jankowski (1977b). The lowest layer of the upper sedimentary unit is distinguished from the graded suevite unit by an erosion discordance. Between 314 and 318 m, this unit is composed of a grey, fine grained siltstone, which is cemented by dolomite. The minerals are sub-horizontally orientated and elongated to rounded dolomite concretions can be observed sporadically. Between 318 and 323 m, graded, grey sandstone can be observed. The weathering of the melt particles decreases with depth, as well as the sub-horizontal orientation of the minerals. Below 323 m, this unit of the graded suevite is a grey, graded, gravel-bearing sandstone, which is also cemented by dolomite. The mineral and lithic clast content is consistent with the suevite unit below the graded suevite. The maximum grain size of the melt particles in this part of the graded suevite is in the upper level larger than the lithic clasts and in lower lever slightly smaller than the lithic clasts. The suevite of this unit grades into a relatively well sorted layer of some decimeters at 330.5 m, with grain sizes of some centimeters. At the interface to the melt-rich suevite unit a graded, grey 2.5 cm layer with maximum grain sizes of 2 mm can be observed. The elongated particles in this layer are also sub-horizontally orientated (Jankowski 1977b).

Melt-rich suevite (331 - 520 m):

In contrast to Jankowski (1977b), who considered the graded suevite as fall-back material, Stöffler (1977) interpreted melt-rich suevite section as fall-back material (from the ejecta plume); whereas, von Engelhardt (1997) expressed the view that this suevite was formed inside the transient crater. This part of the drill core contains two layers of suevite: 331 - 390 m and 436 - 520 m. Between 390 and 436 m, the unit can be described as suevite intersected by blocks of crystalline basement rocks (Bauberger et al. 1974). Between 331 and 390 m, the melt content as well as the lithic clast content, is constant with depth and the maximum grain size slightly increases. Sedimentary rock clasts can just be observed in this part of the middle suevite unit. At 378.5 m, a some decimeters thick layer of sorted suevite, similar to the sorted layer in the upper graded suevite at 330 m, can be observed. From 436 m, a decrease of the melt content can be observed down to 520 m, where macroscopically no melt can be observed anymore. The suevite between 436 and 520 m can be described as a fine particulated matrix,

with inclusions of lithic clasts varying in size. The total content of lithic clasts increases with depth (Stöffler 1977).

Melt-poor suevite (520 - 602 m):

Between 520 to 602 m, the core section can be considered as a zone of basement rocks disrupted by suevite intercalations. Melt particles are macroscopically not detectable. The melt-poor suevite sequences are characterized by decreasing grain size with depth and were interpreted as formed by ground surging (Stöffler 1977).

Dike suevite:

Another type of suevite occurs as dikes in the crystalline basement below the crater or in displaced megablocks of the basement. This type of melt-poor suevite was interpreted as formed by lateral intrusions by highly turbulent flow (Stöffler et al. 1977; Stöffler 1977).

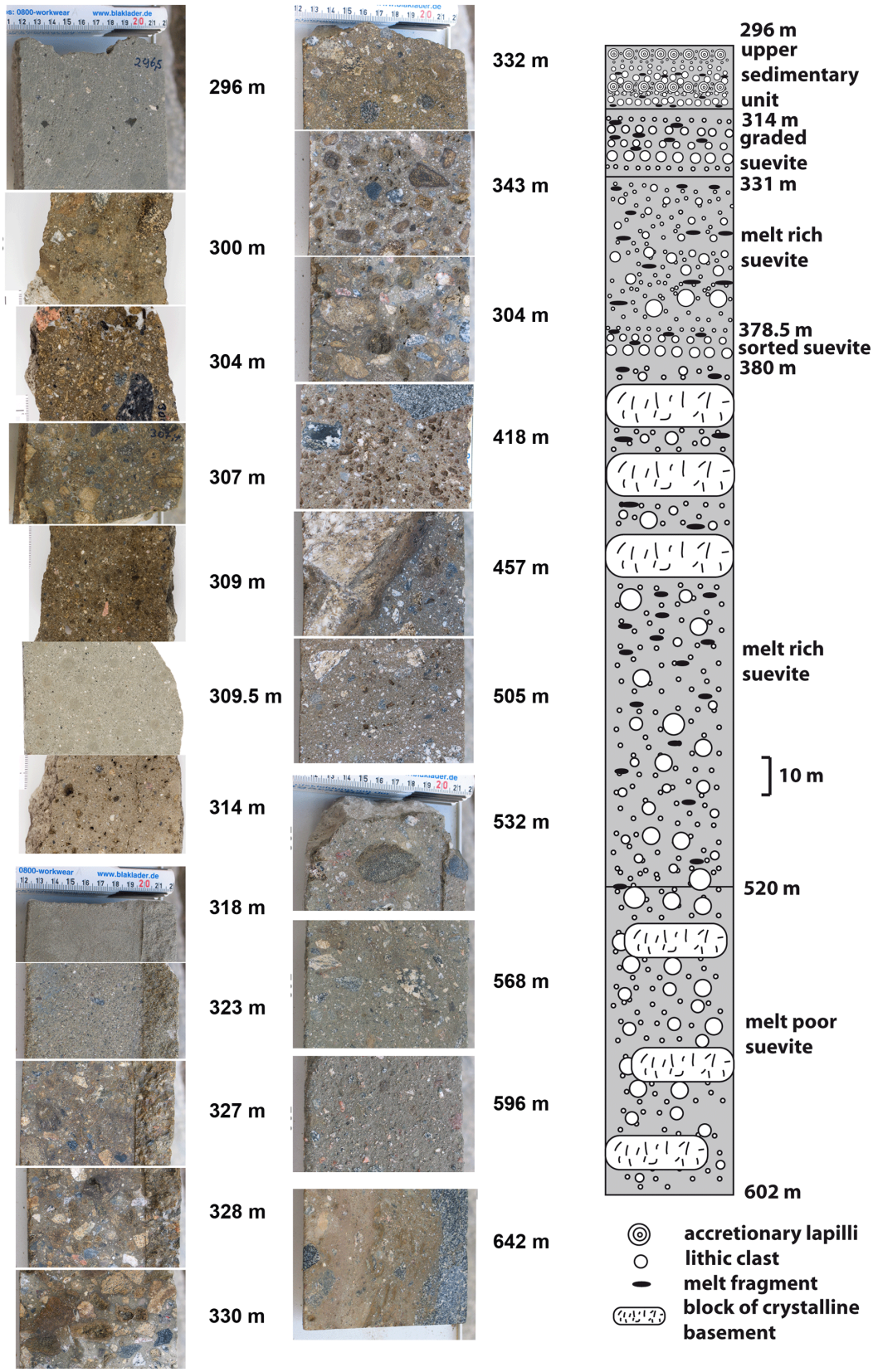

Fig. 3.2.: Drill core photographs of FBN73. upper sedimentary unit: 296 - 314 m. Grain size is increasing with depth down to 307 m and than decreasing up to314 m. At 296 m and 309 m accretionary lapilli can be observed (dark round particles). Graded suevite: 314 - 330 m. Grain size is increasing with depth. Melt-rich suevite: 330 - 520m. Grain size is increasing with depth down to 390 m. Below 390 m, the suevite is composed of a fine grained matrix with inclusions of lithic clasts, with variable grain sizes. Melt-poor suevite: 520 - 602 m. Grain size is decreasing with depth. Right: Schematic profile of the suevite section of the drill core.

3.2.2. Research drilling Enkingen SUBO 18

The core stratigraphy of the Enkingen drill core involves, from top to bottom: 0 to 4.5 m - fluvial Quaternary deposits, clay and gravel; 4.5 to 21 m - Palaeocene clays of the Ries crater lake; from 21 to 100 m suevite with gradational transition to massive impact melt rock. The Enkingen suevite and melt body is located on the inner flank of the inner ring. A detailed macroscopic description of the drill core and the Enkingen magnetic anomaly is given by Pohl et al. (2010). The drill core of Enkingen can be divided in 3 suevite subtypes and a compact impact melt rock below 85 m. The subdivision is based on the color of the suevite, the grain size distribution of lithic clasts and melt particles, melt and lithic clast content, and the matrix composition studied by SEM analyses (Fig. 3.3).

Upper reworked suevite (21 - 40 m):

This suevite unit is composed of a grey suevite, with exponentially increasing melt content and maximum grain size of melt particles. The content and maximum grain size of lithic clasts increase slightly with depth and are always lower than melt content and particle size. The fine grained matrix is replaced partially by secondary carbonate. The sub-horizontal orientation to imbricate structure of the melt particles becomes stronger with depth.

Middle suevite unit (40 - 66 m):

The suevite pass from a red colored, carbonaceous cemented suevite to a brown colored, friable suevite with a particulate matrix. Whereas the melt content decreases abruptly at about 40 m depth, it increases with depth again down to 66 m. The lithic clast content is constant with depth. The suevite is intersected by large lithic clasts and melt particles of several cm in size. Beside these large inclusions, the maximum grain size of lithic clasts and melt particles is decreasing with depth.

Lower suevite unit with intersections of impact melt layers (66 - 86 m):

This brown to red suevite is intersected by coherent melt layers at 66 - 69 m, 75.5 - 76.5 m, and 82.5 - 84.5 m depth. The matrix is friable except for 82 m depth, where it is calcite cemented. The matrix is macroscopically similar to a suevite matrix but microscopically it is similar to a melt rock. No mineral fragments could be detected at the SEM scale and large mounts of pyrite can be observed frequently. Beside the coherent melt layers, the macroscopic lithic clasts and melt particles content show high variations at this core section. The maximum grain size is high, with small variations. The largest lithic clasts (up to several dm in size) can most frequently be observed outside of the coherent melt layers.

Coherent impact melt (86 - 100 m):

Below 86 m, the suevite passes into a compact impact melt rock. Inside the impact melt rock, isolated regions of suevitic-like structure (cm to dm size) can be observed. The melt rock shows variable colors from grey to red. The lithic clast content and sizes are constant inside the impact melt and several carbonate clasts, up to cm size, can be detected.

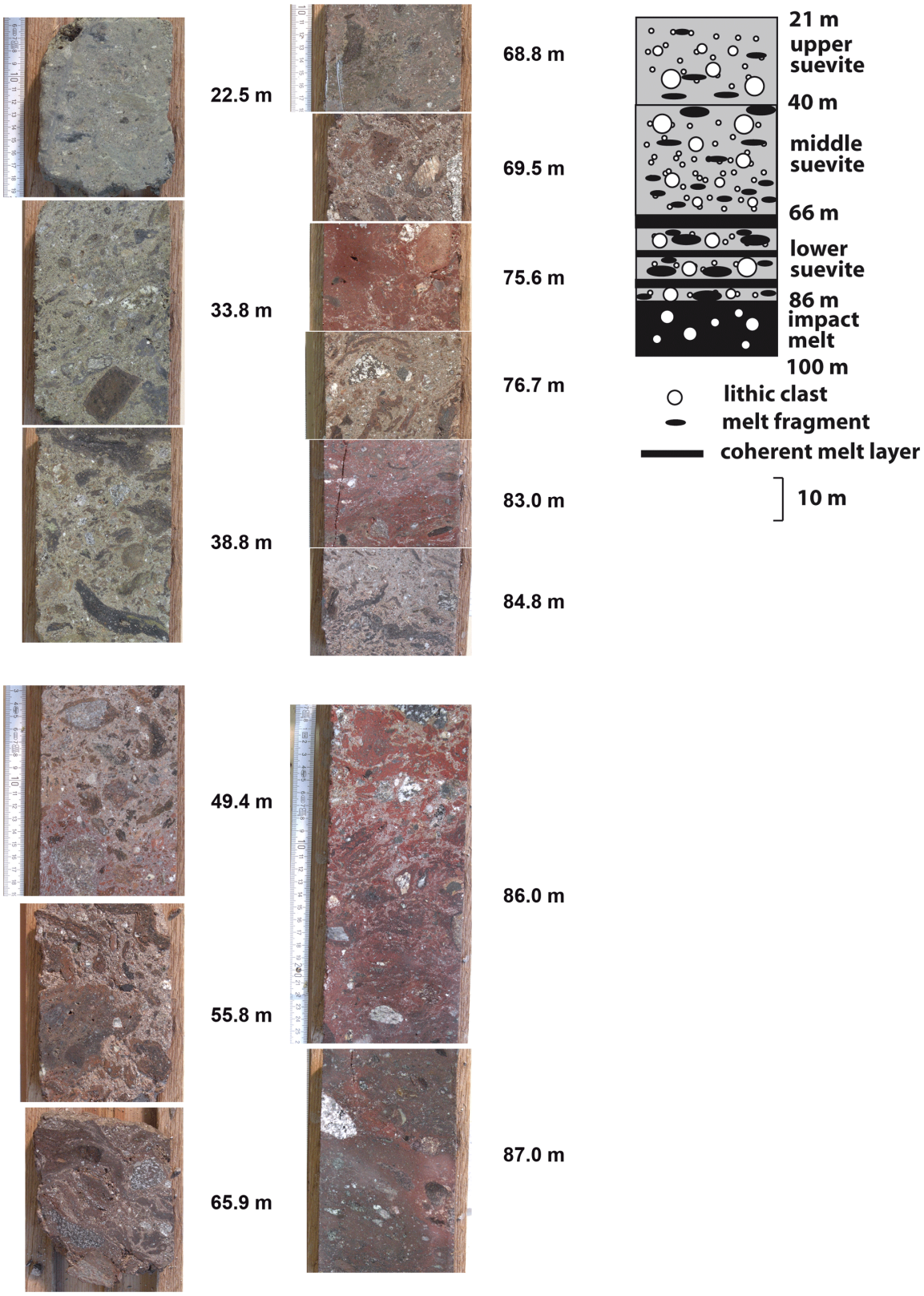

Fig. 3.3.: Drill core photographs of Enkingen. Upper reworked suevite: 20-40 m. Gray suevite with increasing melt content and increasing grain size of lithic clasts and melt particles with depth. Middle suevite unit: 40-66 m. Red suevite with increasing melt content with depth. Lower suevite unit with intersections of impact melt layers: 66-86 m. brown to red suevite with coherent melt layers intersecting the suevite at 66-69 m, 75.5-76.5 m, and 82.5-84.5 m. Coherent impact melt: below 86 m the suevite passes into a compact impact melt rock. Right: Schematic profile of the suevite section of the drill core.

3.2.3. Research drilling Wörnitzostheim

The description and subdivision of the Wörnitzostheim drill core is based on Förstner (1967) and Dressler and Graup (1974). 19 m of crater lake sediments are underlain by about 80 m of suevite followed by 80 m of Bunte Breccia (Fig. 3.4).

Upper reworked suevite (19 - 25 m):

This suevite unit is described as reworked suevite with calcite cemented groundmass (Förstner 1967). The maximum grain size of the lithic clasts and melt particles and the melt content increases with depth. On top of this suevite unit, a 3 m thick sedimentary layer, with inclusions of calcite altered crystalline clasts and rarely melt can be observed. The interface to the upper sedimentary unit forms a thin fine grained sediment layer (Förstner 1967; Dressler and Graup 1974).

Melt-rich suevite (25 - 80 m):

From 25 to 80 m, the suevite has a brown to red color and a friable, silt poor, groundmass. The content of carbonate is about 1 % (mostly Fe bearing dolomites). The maximum grain size of the lithic clasts and melt particles and the melt content increase with depth. The suevite of this unit is melt-rich and dominated by melt. Large lithic clasts can rarely be observed and don't exceed grain sizes of several cm. The sub-horizontal orientation to imbricate structure of the melt particles becomes stronger with depth (Förstner 1967; Dressler and Graup 1974).

Melt-poor suevite (80 - 100 m):

Below 80 m the drill core is described as altered suevite (Förstner 1967). The color fades from light brown to gray. Single melt particles, with large grain sizes, can be observed. The melt content decreases abruptly at 80 m depth and remains constant until the transition to Bunte Breccia, at 100 m depth. The lithic clast content increases slightly with depth, with increasing carbonaceous alteration of the lithic clasts (Förstner 1967; Dressler and Graup 1974).

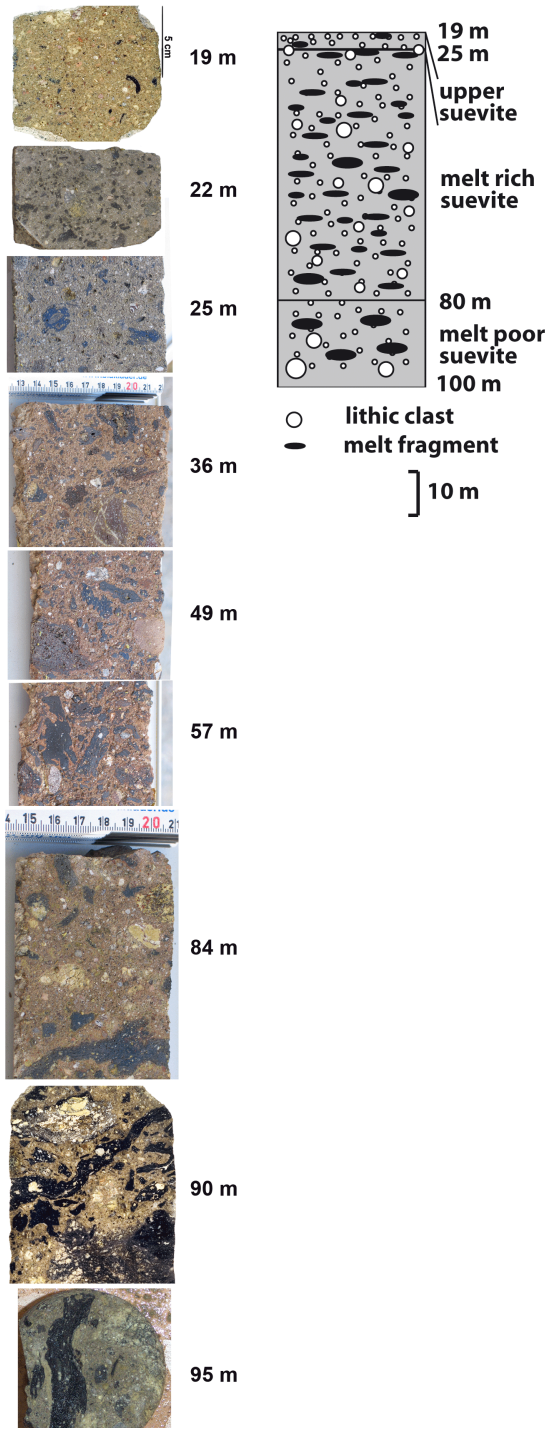

Fig. 3.4.: Drill core photographs of Wörnitzostheim. Upper reworked suevite: 19 - 25 m. Gray suevite, with increasing grain size of lithic clasts and melt particles and increasing melt content with depth. Melt-rich suevite: 25 - 80 m. Brown to red suevite, with high melt content. Slowly increase of grain size of lithic clasts and melt particles and melt content with depth. Melt-poor suevite: below 80 m. Color of suevite fades from light brown to gray. Single melt particles with large grain sizes can be observed. Right: Schematic profile of the suevite section of the drill core.

3.2.4. Research drilling Otting

The Otting core was drilled east of the crater rim. Fifty meters of Bunte Breccia is overlain by 9 m of suevite. The drill core was sunk into the quarry floor of the Otting quarry. According to Bringemeier (1994), there is a lack of at least 6 m overlying suevite in the drill core. The suevite of the Otting drill core is rather homogeneous throughout the core (Fig. 3.5). The suevite has a grey to yellow color and is rather homogeneous in lithic clasts and melt particles content and maximum grain size throughout down to 8 m depth. Inclusions of large lithic clasts (several cm in size) can be frequently observed. The largest particle can be observed at 6.8 m depth. The melt particles show a preferred orientation from almost horizontal to imbricate structure. Below 8 m depth, the maximum grain size of lithic clasts and melt particles decreases with depth.

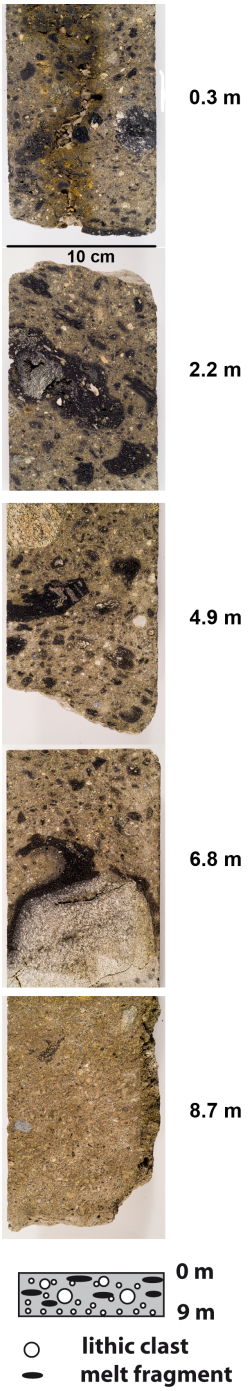

Fig. 3.5.: Drill core photographs of Otting. Gray to yellow suevite, homogeneous in melt content and melt grain size throughout the core down to 8 m depth. Inclusions of lithic clasts with increasing maximum grain size with depth. Largest particle can be observed at 6.8 m depth. Preferred orientation of the melt particles is almost horizontal to imbricate structure. The imbricate structure can best be observed at 2.2 m. Below 8 m depth decreasing grain size of lithic clasts and melt particles with depth. Below pictures: Schematic profile of the suevite section of the drill core.

4. 3D-shape fabric analysis of suevite quarry samples from the Ries crater

4.1. Abstract

In order to differentiate between the two emplacement modes of fall-back and horizontal transport, the shape fabrics of suevite components from two localities outside the Ries crater were analyzed by fitting shape fabric ellipsoids to measured shape fabric ellipses and by applying high-resolution X-ray computed tomography to analyze the three-dimensional shape and orientation of the suevite particles. It could be shown that the preferred orientation of long axes of elongate particles is aligned either radially or concentrically with respect to the crater center. These observations indicate that suevite material was not only derived from an ejecta plume, but was transported by lateral flow under viscous conditions upon fall-back similar to pyroclastic flows.

Photo prints were produced by A. Dittmann (MfN). L. Harris (Institut National de Recherche Scientifique-Eau-Terre-Environnement (INRS-ETE), Québec City, Canada) assisted with the X-ray computed tomography. Image analyses and data processing were performed by the author. Methods and results were discussed with Michel Jébrak and Ulrich Riller.

4.2. Introduction

For the determination and interpretation of shape fabrics of suevite deposits it is necessary to get an insight into the formation of known shape fabrics from different deposition conditions. The shape-preferred orientation, also known as shape fabrics, of components in pyroclastic rocks forms either during emplacement, subsequent compaction, or post-emplacement deformation (Fisher and Schmincke 1984). Shape fabrics formed by compaction are typically characterized by the alignment of flaky and elongate components in a horizontal plane (Fisher and Schmincke 1984). In contrast, shape fabric geometries resulting from viscous flow display a distinct shape-preferred orientation of elongate components, which can be used to identify the flow direction (Schmincke and Swanson 1967). Although components in suevite deposits have been rarely investigated in terms of shape fabrics (Hörz 1965; Bringemeier 1994), they

are excellent candidates for such an analysis to infer mode of transport and emplacement.

The mechanism of fabric development resulting from lateral particle transport, notably in sedimentary depositional environments, has been long debated. Notably, Jeffery (1922) suggested a mechanism in which the maximum diameters of elongate particles rotate transverse to the flow direction during transport. By contrast, Glen et al. (1957) concluded that there is a high probability that elongate particles will be oriented mainly parallel to the flow direction during transport. Moreover, Allen (1982) suggested that vertical variations in fabric orientations are chiefly controlled by variations of the Reynolds number at different levels in the transporting medium. Major (1998) analyzed the orientations of pebbles in experimental debris flow deposits and found that particle long axes, in the outer part of the deposit, are preferably aligned subparallel to debris flow margins, whereas those in the inner part are deposited parallel and normal to the primary flow direction. These fabric studies were used to analyze paleocurrent directions in fluvial, marine or volcanic sedimentary environments (e.g., Best 1992; Davies and Walker 1974; Rusnak 1957).

Information on particle shape fabrics in rocks is usually limited to two dimensions. In order to analyze shape fabrics in three dimensions (3D), rock samples are generally cut along at least two principal planes of the shape fabric ellipsoid. One plane will typically be concordant to the horizontal surface, whereas the other plane will be orthogonal to it and parallel to the apparent flow direction. These sections are then analyzed by digital imaging (e.g., Capaccioni et al. 2001), visual counting and measurement of the particle long axes (e.g., Tucker 1996), or by determining a best-fit ellipse using the center-to-center method (e.g., Seaman and Williams 1992). The flow direction is then determined from the pattern of shape-preferred orientation of elongate particles. These methods require some knowledge on the relationship of clast orientation and flow direction.

Ramsay (2003 (original 1967)) described a method for determining the orientations and magnitudes of the three principal axes of the strain ellipsoid. This method is based on the determination of three sectional strain ellipses that are mutually perpendicular to each other. A best-fit strain ellipsoid is determined using the principal axes and orientation of the sectional ellipses. This technique does not rely on assumptions regarding the orientation of the ellipsoid and has been specifically used to analyze strain directions in structural geological studies (De Paor 1990; Robin 2002; Launeau and Robin 2005).

We modified Ramsay (2003 (original 1967))'s technique to fit a shape fabric ellipsoid to measured shape fabric ellipses, thus providing information on the mean orientation of all suevite particles for a given location from the Ries crater. Moreover, we applied high-resolution X-ray computed tomography (CT) on the studied suevite deposits to determine the shape and preferred orientation of suevite particles. An overview of X-ray CT technology and its application to the geosciences can be found in Ketcham and Carlson (2001) and Cnudde et al. (2006). The first application of CT to the study of suevite samples was conducted by

Koeberl et al. (2002). O'Connor et al. (2009) recently developed the software that calculates a mean best-fit ellipsoid from CT images and determines the shape-preferred orientation of particles. In the present study we compare the two methods of 3D shape fabric analysis using samples of the Ries suevite from the suevite quarries Aumühle and Seelbronn (Fig. 3.1) and discuss the fabric data in terms of emplacement and transport of the suevite.

4.3. Analytical methods

4.3.1. Determination of shape fabric ellipsoids from sections

11 suevite cubes from the Aumühle quarry and 7 suevite cubes from the Seelbronn quarry were cut concordant to the principal shape fabric planes defined by the shape-preferred orientation of elongate melt and lithic particles. In addition, the orientations of the cubes in space were recorded. The three principal planes were photographed using 3.5x magnification and a resolution of 300 dpi. For each plane, a minimum of about 100 elongate particles (mainly melt particles), each of which at least 1.5 mm long, were highlighted using the software Adobe Photoshop. This template was processed using the software ImageJ and the main shape-preferred orientation of the particles' long axes was determined for each plane. Rose diagrams display the orientations for each plane of the suevite cubes (Figs. 4.1 and 4.2). Shape fabric ellipses were fitted to the mean orientations evident from the rose diagrams and followed by shape fabric ellipsoid fitting and reorientation. In the following the methodology is described in detail:

Fitting of shape fabric ellipsoid from 3 perpendicular cube planes

Shape fabric ellipse fitting

The main orientation of the particles was determined from the rose diagram and set to θ, the anticlockwise angle of the main axis of the ellipse. The major and minor axes of the shape fabric ellipses were determined as the deviation from the unit circle. The radius R of an un-deformed circle would be the number of measured particles N divided by the number of rose diagram segments S from 0 to 180.

$$R = \frac{N}{S} \tag{4.1}$$

The deviation from the unit circle of the semi-major axis $a = 1 + e_x$ (e expresses the eccentricity) is calculated by dividing of the length of the main orientation of rose diagram l by

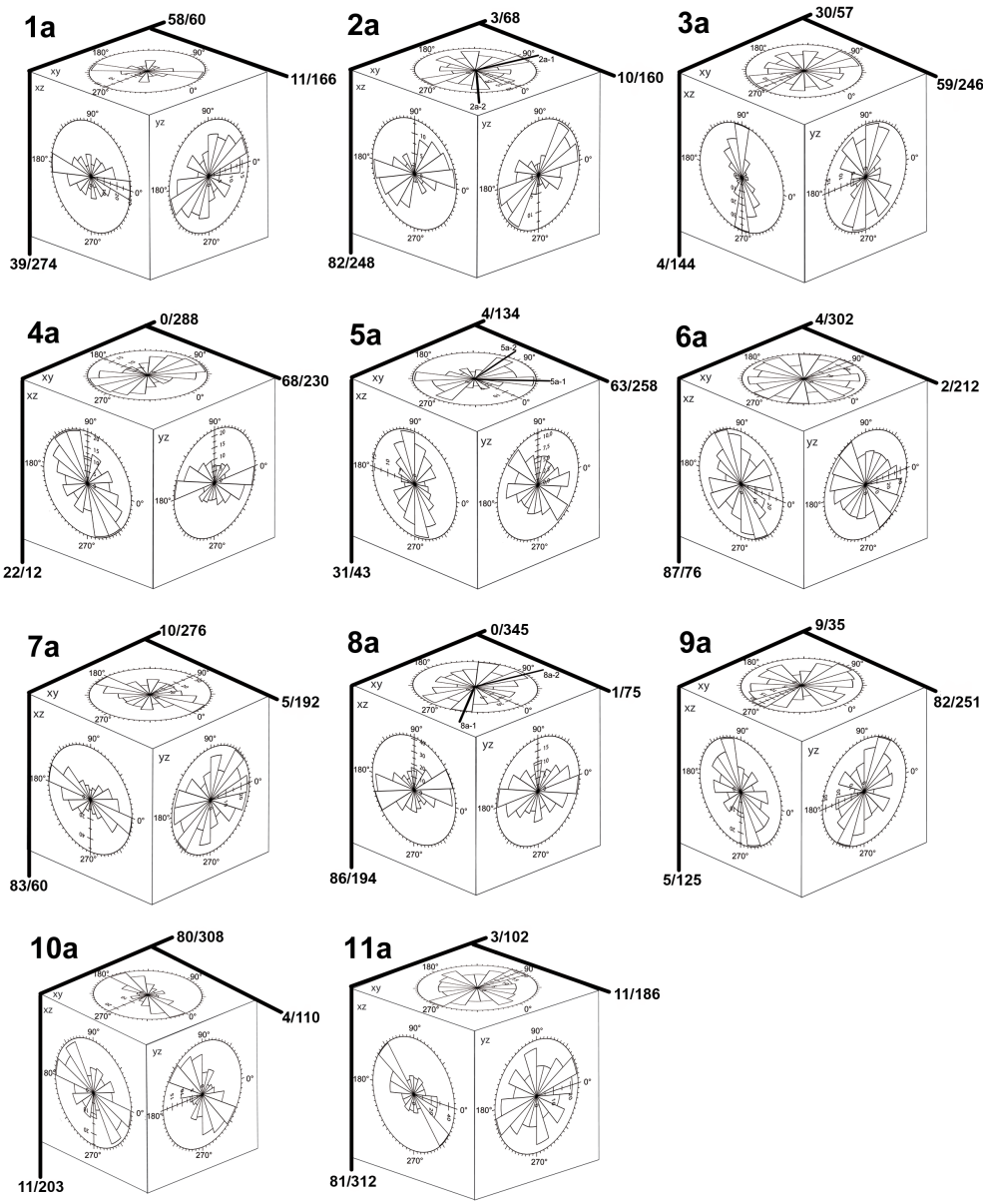

Fig. 4.1.: Suevite cubes from the Aumühle quarry with rose diagrams on each principal shape fabric plane. Particles in the xy, yz and xz planes display variable shape-preferred orientations. Numbers at bold lines are plunge and plunge direction of the cube axes.

radius R.

$$a = 1 + e_x = \frac{l}{R} \tag{4.2}$$

The deviation from the unit circle of the semi-minor axis $b = 1 + e_y$ is calculated by

$$b = 1 + \frac{1-a}{a} \tag{4.3}$$

These ellipses represent the deviation from an isotropic (completely random) orientation of all particles of each plane.

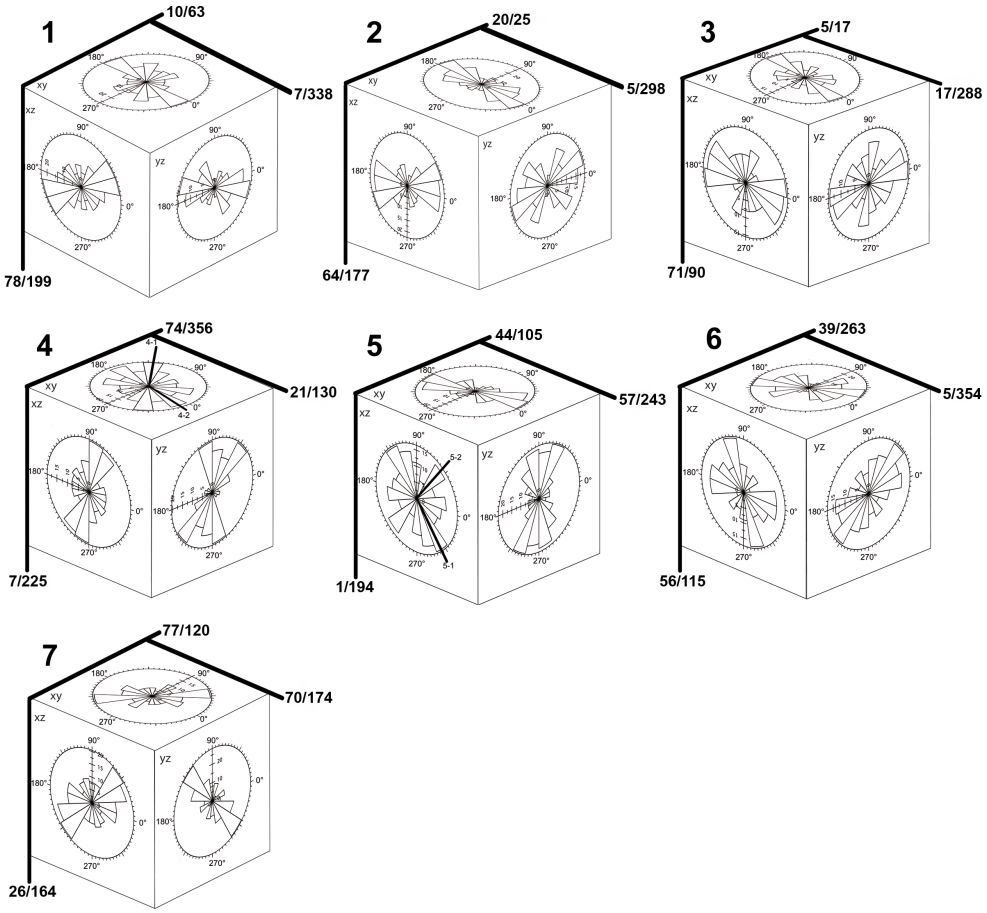

Fig. 4.2.: Suevite cubes from the Seelbronn quarry with rose diagrams for each principal shape fabric plane. Particles in the xy, yz, and xz planes display variable shape-preferred orientations. For sample 4 and 5, two preferred orientations were observed in the xy and xz plane, respectively. Numbers at bold lines are plunge and plunge direction of the cube axes.

Shape fabric ellipsoid fitting

The general equation for each shape fabric ellipse could also be written (for the *xy* plane) as

$$\left(\frac{\cos^2\theta}{a^2_{xy}}+\frac{\sin^2\theta}{b^2_{xy}}\right)x^2-2\sin\theta\cos\theta\left(\frac{1}{b^2_{xy}}-\frac{1}{a^2_{xy}}\right)xy+\left(\frac{\sin^2\theta}{a^2_{xy}}+\frac{\cos^2\theta}{b^2_{xy}}\right)y^2=1 \quad (4.4)$$

For a detailed derivation, see Ramsay (2003 (original 1967)). Simplifying this equation results in

$$\lambda'_x x^2-2\gamma'_{xy}xy+\lambda'_y y^2=1 \quad (4.5a)$$

$$\lambda'_y y^2-2\gamma'_{yz}yz+\lambda'_z z^2=1 \quad (4.5b)$$

$$\lambda'_z z^2-2\gamma'_{xz}xz+\lambda'_x x^2=1 \quad (4.5c)$$

for the *xy*, *yz*, and *xz* planes, respectively, with λ' and γ' replacing the first two coefficients of equation (3.4). The three finite-shape-fabric invariants could be obtained by

$$J_1 = \lambda'_x + \lambda'_y + \lambda'_z \tag{4.6a}$$
$$J_2 = \lambda'_x\lambda'_y + \lambda'_y\lambda'_z + \lambda'_z\lambda'_x - \gamma'_{xy}{}^2 - \gamma'_{yz}{}^2 - \gamma'_{xz}{}^2 \tag{4.6b}$$
$$J_3 = \lambda'_x\lambda'_y\lambda'_z - 2\gamma'_{xy}\gamma'_{yz}\gamma'_{xz} - \lambda'_x\gamma'_{yz}{}^2 - \lambda'_y\gamma'_{xz}{}^2 - \lambda'_z\gamma'_{xy}{}^2 \tag{4.6c}$$

where λ' is the reciprocal quadratic extension of the axis of the ellipsoid, with $\lambda = 1/\lambda'$ and λ'_1, λ'_2, and λ'_3, the reciprocal quadratic extension of the three principal axes of the ellipsoid, which could be obtained by solving the cubic equation

$$\lambda'^3 - J_1\lambda'^2 + J_2\lambda' - J_3 = 0 \tag{4.7}$$

Knowing that λ'_2 lies between the turning points of the cubic equation given by

$$3\lambda'^2 - 2J_1\lambda' + J_2 = 0 \tag{4.8}$$

the value λ'_2 could be obtained by Newton's method

$$\lambda'_{(2)_1} = \lambda'_{(2)_0} - \frac{\lambda'_{(2)_0}{}^3 - J_1\lambda'_{(2)_0}{}^2 + J_2\lambda'_{(2)_0} - J_3}{3\lambda'_{(2)_0}{}^2 - 2J_1\lambda'_{(2)_0} + J_2} \tag{4.9}$$

with a first guess of $\lambda'_{(2)_0}$ and a better approximation of $\lambda'_{(2)_1}$. After ten iterations, $\lambda'_{(2)_{10}} = \lambda'_2$. Values for λ'_1 and λ'_3 could be obtained by solving the quadratic expression

$$\lambda'^2 + (\lambda'_2 - J_1)\lambda' + (\lambda'^2_2 - J_1\lambda'_2 + J_2) = 0 \tag{4.10}$$

The endpoints of the three symmetry axes of the shape fabric ellipsoid could be established by solving the system of equations

$$\frac{x_1}{A} = \frac{-y_1}{B} = \frac{-z_1}{C} \tag{4.11a}$$
$$x_1{}^2 + y_1{}^2 + z_1{}^2 = \lambda_1 \tag{4.11b}$$

with

$$A = \lambda'_y\lambda'_z - \lambda'_1\lambda'_y - \lambda'_1\lambda'_z + \lambda'^2_1 - \gamma'_{yz}{}^2 \tag{4.12a}$$
$$B = \gamma'_{xy}\lambda'_z + \gamma'_{xy}\lambda'_1 - \gamma'_{zx}\gamma'_{yz} \tag{4.12b}$$
$$C = \gamma'_{xy}\gamma'_{yz} + \lambda'_y\gamma'_{zx} - \lambda'_1\gamma'_{zx} \tag{4.12c}$$

for the symmetry axis with the endpoint (x_1, y_1, z_1). Thus x_1, y_1, and z_1 are respectively

$$x_1 = -\frac{y_1 \cdot A}{B} \tag{4.13a}$$

$$y_1 = \sqrt{\frac{\lambda_1}{\frac{A^2}{B^2} + 1 + \frac{C^2}{B^2}}} \tag{4.13b}$$

$$z_1 = \frac{y_1 \cdot C}{B} \tag{4.13c}$$

The endpoint (x_2, y_2, z_2) of the second symmetry axis could be similarly obtained. Because the shape fabric ellipsoid is the deviation from the unit sphere, the length of the third symmetry axis r_3 can be obtained by

$$r_3 = \frac{1}{\sqrt{{x_1}^2 + {y_1}^2 + {z_1}^2} \cdot \sqrt{{x_2}^2 + {y_2}^2 + {z_2}^2}} \tag{4.14}$$

The endpoint of the third symmetry axis can be calculated using the cross-product of points 1 and 2 multiplied by a length factor.

$$\begin{pmatrix} {x_3}' \\ {y_3}' \\ {z_3}' \end{pmatrix} = \begin{pmatrix} x_1 \\ y_1 \\ z_1 \end{pmatrix} \times \begin{pmatrix} x_2 \\ y_2 \\ z_2 \end{pmatrix} \tag{4.15a}$$

$$\begin{pmatrix} x_3 \\ y_3 \\ z_3 \end{pmatrix} = \begin{pmatrix} {x_3}' \\ {y_3}' \\ {z_3}' \end{pmatrix} \cdot \sqrt{\frac{{r_3}^2}{({x_3}')^2 + ({y_3}')^2 + ({z_3}')^2}} \tag{4.15b}$$

Reorienting samples

The investigated samples have orientations recorded in the *plunge* and *plunge direction* convention. The *plunge* is the angle below the horizontal and has a value from 0 to 90°. The *plunge direction* is the azimuth of the direction of the plunge as projected to the horizontal. By determining the position of the *plunge* and the *plunge direction* of the suevite cube axes, the symmetry axes of the ellipsoid can be reoriented to their original geographical orientations.

The first step is to transform the plunge and plunge direction of the cube axis into polar coordinates. Whereas an azimuth of 0° represents north and is counted clockwise, 0° in mathematical expressions represents east and counting is anticlockwise. Angle α is the angle between the x axis and the projection of a space vector on the xy plane, and can be found by $\alpha = 90°$-[plunge direction]. Angle β is the angle between the z axis and a space vector and can be found by $\beta = 90°$+[plunge].

Assuming unit length for the coordinate axis of the suevite cube, coordinate axes could be

expressed as

$$\begin{pmatrix} x \\ y \\ z \end{pmatrix} = \begin{pmatrix} \sin\beta_x \cos\alpha_x & \sin\beta_x \sin\alpha_x & \cos\beta_x \\ \sin\beta_y \cos\alpha_y & \sin\beta_y \sin\alpha_y & \cos\beta_y \\ \sin\beta_z \cos\alpha_z & \sin\beta_z \sin\alpha_z & \cos\beta_z \end{pmatrix} \tag{4.16}$$

The endpoints of the shape fabric ellipsoids can be transformed into the coordinate system of the orientated suevite cube by

$$\begin{pmatrix} x'_1 & x'_2 & x'_2 \\ y'_1 & y'_2 & y'_3 \\ z'_1 & z'_2 & z'_3 \end{pmatrix} = \begin{pmatrix} \sin\beta_x \cos\alpha_x & \sin\beta_x \sin\alpha_x & \cos\beta_x \\ \sin\beta_y \cos\alpha_y & \sin\beta_y \sin\alpha_y & \cos\beta_y \\ \sin\beta_z \cos\alpha_z & \sin\beta_z \sin\alpha_z & \cos\beta_z \end{pmatrix} \bullet \begin{pmatrix} x_1 & x_2 & x_2 \\ y_1 & y_2 & y_3 \\ z_1 & z_2 & z_3 \end{pmatrix} \tag{4.17}$$

The cartesian coordinates must be transformed into polar coordinates for each symmetry axis of the shape fabric ellipsoid by

$$r_1 = \sqrt{{x'_1}^2 + {y'_1}^2 + {z'_1}^2} \tag{4.18a}$$

$$\alpha_1 = \arccos \frac{x'_1}{\sqrt{{x'_1}^2 + {y'_1}^2}} \tag{4.18b}$$

$$\beta_1 = \frac{\pi}{2} - \arctan \frac{z'_1}{\sqrt{{x'_1}^2 + {y'_1}^2}} \tag{4.18c}$$

The values α_1, α_2, α_3, β_1, β_2 and β_3 must be transformed into plunge and plunge direction expressions by applying [plunge direction]=$90^\circ - \alpha$ and [plunge]=$\beta - 90^\circ$.

4.3.2. Determination of particle orientations by X-ray computed tomography

The X-ray tomographic intensities were analyzed for samples 1a and 11a from Aumühle and samples 5 and 7 from Seelbronn using a Siemens Somatom Volume Access scanner at the Institut National de Recherche Scientifique-Eau-Terre-Environnement (INRS-ETE) in Quebec City, Canada. Each sample was run through a crown consisting of a rotating X-Ray source with 600 vertical receptors. This system emits X-rays from all angles across the samples, which are then recorded by the receptors. Attenuated intensities of the rays are then transmitted to the computer. The image is created by digital reconstruction of the signal received from each receptor (Ketcham and Carlson 2001, Cnudde et al. 2006).

Tomographic intensity values were represented as a function of a 4096-step gray scale corresponding to mass density. Longitudinal sections were generated for each sample using an X-ray source of 140 kV. Each resulting image has a resolution of 512 x 512 pixels, with 2.522 pixels per millimeter. These longitudinal images are spaced at 0.6 mm (i.e., transverse

distance = 0.6 mm).

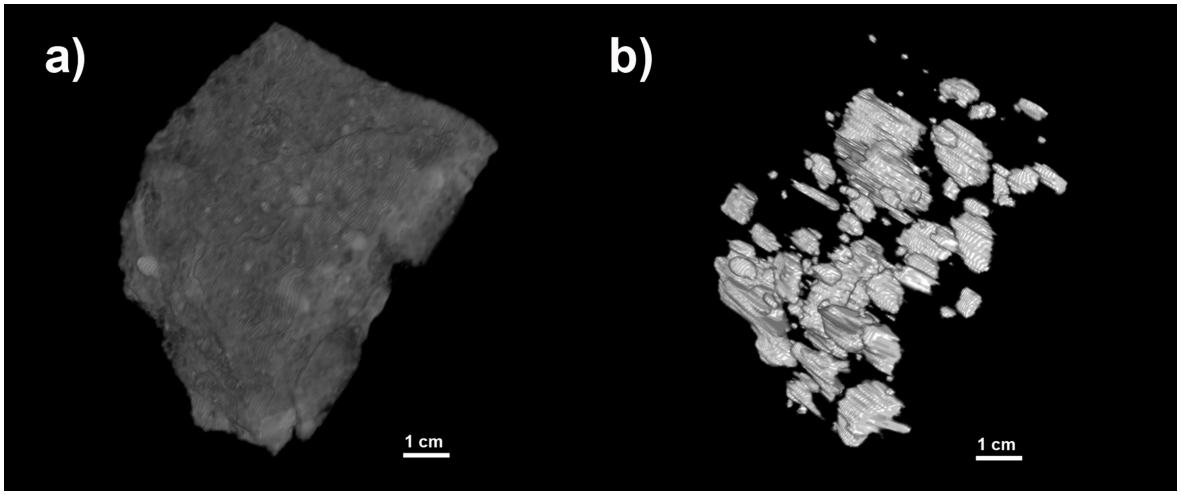

Fig. 4.3.: Three-dimensional reconstruction of the clast population in suevite sample Aumühle-1a: a) sample imaged by CT; b): isolated melt and rock particles after processing using the software Adobe Photoshop.

The gray-shades in CT images (e.g., Fig. 4.3) correspond to the attenuation characteristics of the component material. Because gray shade varies with particle type, each image was individually interpreted based on its gray shade and specific texture. The margins of particles with long axes larger than 1.5 mm were outlined using Adobe Photoshop without distinguishing between individual particle types. Particle geometry was analyzed with ImageJ. The orientations of each particle's long and short axes, as well as the particle's position and orientation, were measured on each CT image. The virtual stacking of all images resulted in a 3D image of fabric geometry that is displayed using the ImageJ 3D viewer (Schmid 2009) (Fig. 4.3). An ellipsoid was fitted for each particle and, collectively, these ellipsoids were used to quantify the shape fabric ellipsoid for each sample. In the following the methodology is described in detail:

Shape fabric ellipsoid fitting from X-ray tomography data

Ellipse fitting of each particle in the *xy*, *yz* and *xz* planes

For the *xy* plane:

The major (a) and minor (b) axes of one particle appearing in different CT images were fitted in a linear equation with slope m and intercept n. The maximum major axis of all images was set to a_{xy}. The minor axis b_{xy} was calculated from the linear equation below. Because

half-axes are used later in the ellipsoid fitting, a_{xy} and b_{xy} were divided by 2.

$$b = m \cdot a + n \tag{4.19a}$$

$$a_{xy} = \frac{\max(a)}{2} \tag{4.19b}$$

$$a_{xy} = \frac{m \cdot \max(a) + n}{2} \tag{4.19c}$$

The angle θ_{xy} of the xy plane was determined as the mean angle value of the major axes of the particle in each CT image, neglecting the values of the first and last three images for resolution reasons.
The distance of the endpoint of the major axis in the xy plane was determined by

$$dx = a_{xy} \cdot \cos(\theta_{xy}) \tag{4.20a}$$

$$dy = a_{xy} \cdot \sin(\theta_{xy}) \tag{4.20b}$$

The distance in the z direction was determined by the difference in the number N_z of the last and first CT images where the particle could be observed, multiplied by the distance between each plane (0.6 mm) divided by 2.

$$dz = \frac{(\max(N_z) - \min(N_z)) \cdot 0.6}{2} \tag{4.21}$$

For the yz plane:

The first step is to determine the length l_1 from the particle in the yz plane by

$$l_1 = \sqrt{dy^2 + dz^2} \tag{4.22}$$

The angle θ_1 of this vector was obtained by fitting the y position of the particle in each CT image with $N_z \cdot 0.6$. The slope of the linear equation is the tangent of θ_1. A second point of the ellipse in the yz plane can be obtained by the 90° value of the ellipse in the xy plane. The length l_2 of this vector is calculated from the ellipse equation

$$1 = \frac{(l_2 \cdot \cos(90 - \theta_{xy}))^2}{a_{xy}^2} + \frac{(l_2 \cdot \sin(90 - \theta_{xy}))^2}{b_{xy}^2} \tag{4.23}$$

The l_2 vector is parallel to the y axis and hence the angle in the yz plane is 0°. If $l_1 > l_2$, the major axis in the yz plane is $a_{yz} = l_1$ and the angle of a_{yz} to the y axis is $\theta_{yz} = \theta_1$. The

intermediate axis in the yz plane, b_{yz}, is again found by the ellipse equation

$$1 = \frac{(l_2 \cdot \cos(-\theta_1))^2}{a_{yz}^2} + \frac{(l_2 \cdot \sin(-\theta_1))^2}{b_{yz}^2} \tag{4.24}$$

If $l_1 < l_2$, the major axis in the yz plane is $a_{yz} = l_2$, and the angle of a_{yz} to the y axis is $\theta_{yz} = 0$. In this case, b_{yz} is found by equation 3.24 with positive θ_1 values.

For the zx plane:

Length l_1 and angle θ_1 of the zx plane are obtained in the same way as for the yz plane by substituting x for y. The second point of the ellipse in the xz plane will be obtained by the 0° value of the ellipse in the xy plane. The length l_2 of this vector is calculated from the ellipse equation

$$1 = \frac{(l_2 \cdot \cos(-\theta_{xy}))^2}{a_{xy}^2} + \frac{(l_2 \cdot \sin(-\theta_{xy}))^2}{b_{xy}^2} \tag{4.25}$$

Vector l_2 is parallel to the x axis and hence the angle in the zx plane is 0°. Values a_{zx}, b_{zx}, and θ_{zx} can be found in the same way as for the yz plane. Finally, it should be taken into account that the ordinate of the zx plane should be the z axis for the later ellipsoid fitting. For this reason $\theta_{zx} = \theta_{zx} + 90°$.

Shape fabric ellipsoid fitting

An ellipsoid is fitted from the three ellipses for each particle and reoriented as described in Section 4.3.1.
The particle ellipsoids are weighted by setting the major axis of each ellipsoid to 1. The average ellipsoid can be found by the mean value of all N particle ellipsoids according to

$$\begin{pmatrix} r_{1mean} & r_{2mean} & r_{3mean} \\ \alpha_{1mean} & \alpha_{2mean} & \alpha_{3mean} \\ \beta_{1mean} & \beta_{2mean} & \beta_{3mean} \end{pmatrix} = \frac{1}{N} \sum_{i=1}^{N} \begin{pmatrix} r_{1i} & r_{2i} & r_{3i} \\ \alpha_{1i} & \alpha_{2i} & \alpha_{3i} \\ \beta_{1i} & \beta_{2i} & \beta_{3i} \end{pmatrix} \tag{4.26}$$

4.4. Results

4.4.1. Shape fabric ellipsoids fitted from sections

The shape-preferred orientation of suevite components from Aumühle is less pronounced than that from Seelbronn (Figs. 4.1 and 4.2). Specifically, the majority of particles in the Aumühle samples (Fig. 4.1) show a preferred orientation on either one (sample 11a) or two cube surfaces (sample 1a), whereas a strong shape-preferred particle orientation is evident

on two (sample 5) or even all cube surfaces (sample 7) of the Seelbronn samples (Fig. 4.2). If two distinct maxima of shape-preferred orientations were observed on a single surface, two different shape fabric ellipses were calculated for the surface, and two different fabric ellipsoids thereby obtained for this sample. Maximum principal fabric ellipsoid axes at Aumühle are radial or concentric with respect to the crater center. Radially disposed axes plunge toward the crater center, and concentrically disposed axes plunge mostly to the SE, but sporadically also to the NW (Fig. 4.4a). Maximum principal ellipsoid axes at Seelbronn are concentric or radial with respect to the crater center. Although these ellipsoid axes do not display any preferred plunge direction, the intermediate and minimum axes tend to preferentially plunge away from the crater (Fig. 4.4b).

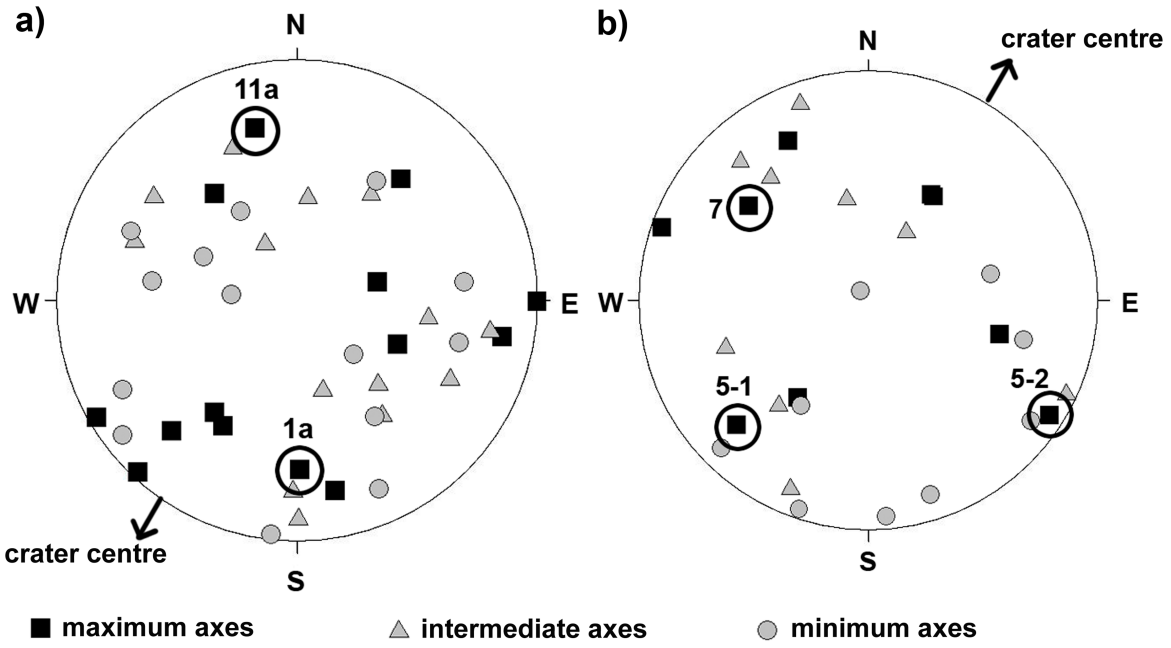

Fig. 4.4.: Lower-hemisphere equal-area projection showing the orientation of principal shape fabric ellipsoid axes for samples from Aumühle (a) and Seelbronn (b). Circles represent ellipsoid axes measured by CT (see also Figure 4.5).

4.4.2. Particle orientations from X-ray computed tomography

All particle long axes in sample Aumühle-1a are disposed either concentrically or radially with respect to the crater center (Figs. 4.5a, b). Most axes plunge moderately to the SE or to the NE. The intermediate and minimum fabric ellipsoid axes plunge to the SE and NW or to the SW. The maximum axis of the average fabric ellipsoid plunges shallowly to the SSE (Fig. 4.5b). The particle long axes of sample Aumühle-11a plunge at low angles to the N or to the S, i.e., at an angle of 30° with respect to crater margin (Figs. 4.5c, d). Conversely, the respective short axes plunge moderately or shallowly to the SE or NW. Similar to particle long axes, the maximum axis of the average ellipsoid plunges shallowly toward the N.

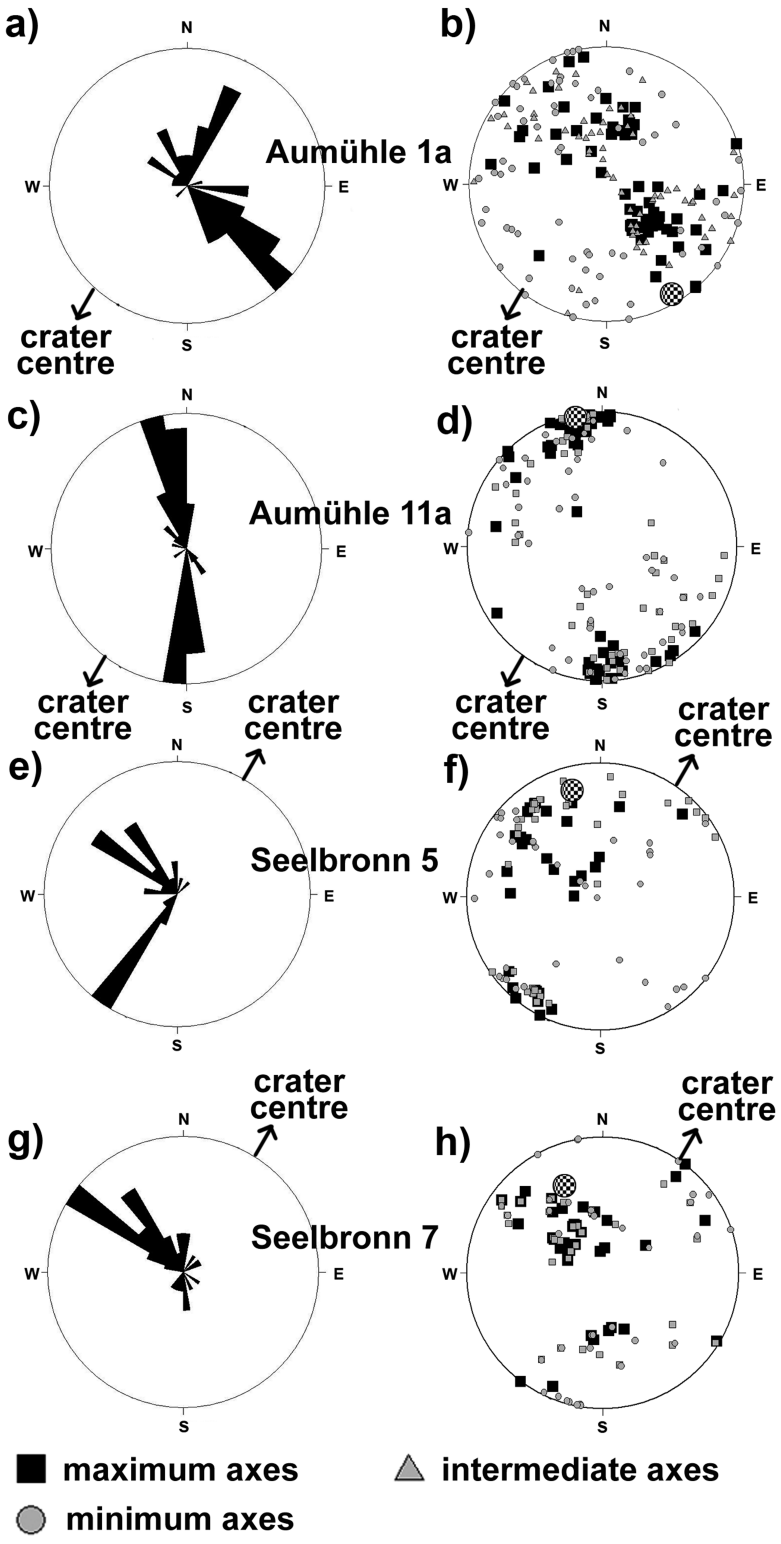

Fig. 4.5.: Left: Rose diagrams showing plunge direction in 10° bins for maximum principal ellipsoid axes as calculated by X-ray computed tomography; Right: corresponding lower-hemisphere equal-area projections showing the orientations of principal axes of particle shapes and the maximum principal axis of the shape fabric ellipsoid (large checkered circle). Note that the shape fabric ellipsoid represents an average of all particle ellipsoids. Sample numbers are: a, b) Aumühle-1a; c, d) Aumühle-11a; e, f) Seelbronn-5; g, h) Seelbronn-7.

Particle long axes of sample Seelbronn-5 are either concentric or radial with respect to the crater center (Figs. 4.5e, f). The concentric particle long axes plunge steeply to moderately to the NW. Most radial particle long axes are horizontal. Accordingly, the intermediate and short axes of particles are concentric or radial and plunge respectively shallowly or steeply. The maximum principal axis of the average fabric ellipsoid plunges moderately to the NNW (Fig. 4.5f).

Most of the particle long axes of sample Seelbronn-7 are concentric with respect to the crater center and plunge steeply to moderately to the NW (Fig. 4.5g, h). Intermediate and short particle axes are either concentric or radial with respect to the crater center and plunge moderately to shallowly. The maximum axis of the average fabric ellipsoid plunges moderately to the NNW (Fig. 4.5h).

4.4.3. Comparison of results from 2D shape fabric and CT data

Table 4.1.: Comparison of plunge and plunge direction from two-dimensional and computed tomography (CT) data of shape fabric ellipsoid maximum axes for samples Aumühle-1a, Aumühle-11a, Seelbronn-5 and Seelbronn-7 according to the rose diagrams and stereonets in Figures 4.4 and 4.5 and their position inside the quarry.

Sample	Position inside the quarry	Plunge/plunge direction from 2D data		Plunge/plunge direction from CT data		
		1st orientation	2nd orientation	average ellipsoid	1st orientation	2nd orientation
Aumühle 1a	1 m above quarry floor	30/179		4/150	moderate/135	moderate/025
Aumühle 11a	1 m above Bunte breccia	27/346		3/348	shallow/350	flat/180
Seelbronn 5	4 m above quarry floor	22/227	8/122	21/346	shallow/225	moderate/310
Seelbronn 7	2 m above Bunte breccia	34/308		31/337	moderate/305	

In terms of plunge direction, the orientations of the shape fabric ellipsoids derived from the 2D data are almost identical to the average ellipsoids derived from CT for samples Aumühle-1a, Aumühle-11a and Seelbronn-7 (Table 4.1). The two orientations computed for the Seelbronn-5 shape fabric ellipsoids using 2D shape fabric data are the same as the two preferred particle orientations derived from CT. For Aumühle-1a, the orientations of the average ellipsoid inferred from CT and the shape fabric ellipsoid obtained from 2D data are

mean values of the two preferred orientations of the particle long axes. The same holds for the average ellipsoid of Seelbronn-5. In these cases, calculating the shape fabric ellipsoid from 2D data and from CT would result in erroneous shape-preferred particle orientations.

If a large number of clasts is available, both techniques provide statistically significant results without tedious preparation or destruction of samples. In the best-fit ellipsoid method using 2D sections, it is theoretically possible to distinguish between types of rock and melt particles through optical observations. However, application of the CT method requires samples to be cut into slabs and thus to be destroyed (Koeberl et al. 2002), following microscopic inspection of particles. For the 2D ellipse fitting on each cube face, approximately 100 particles need to be counted to achieve a statistically meaningful result. By contrast, the CT technique requires counting particles of up to 300 sections and assembling the sections for analysis. This amounts to counting up to 1500 particles per sample. Despite the longer time necessary for imaging analysis, CT results are more accurate because the orientation of all particles is taken into account in this technique. By contrast, ellipsoid fitting from 2D sections provides only a mean value of the particle orientations. Moreover, if the particles of one sample show two or more preferred orientations, the fitted ellipsoid may result in erroneous shape fabric ellipsoids. In some cases, it may be possible to obtain two ellipse orientations with 2D fitting if two preferred orientations are observed in one plane. In this case, two shape fabric ellipses have to be fitted on this plane, which results in two shape fabric ellipsoids.

4.5. Discussion and Conclusions

Acquisition of 3D orientation data from rock samples is important, especially for sedimentologists studying the depositional conditions of sedimentary transport systems. The present study is the first application of X-ray computed tomography to investigate the shape-preferred orientation of breccia components in general, and impact breccias in particular. It is also the first study in which these fabric data are compared to those derived from 2D shape fabric ellipsoid fitting. It is shown in 3D that the long axes of elongate particles in the Ries suevite are orientated either radially or concentrically with respect to the crater center. The only other work of clast orientations in Ries suevite that is comparable to ours is the one by Bringemeier (1994) who detected a preferred orientation of clasts in suevite on a 6-meter tall planar section through the Otting quarry (Fig. 3.1). More than 80% of the suevite clasts are aligned in this site. Shape-preferred clast orientations have also been sporadically detected in suevite from other terrestrial impact craters. For example, Wittmann (2007) investigated suevites from the Yaxcopoil-1 drill core, which is located 60 km SSW of the center of the Chicxulub impact structure in Mexico. Here, the long axes of suevite melt particles are either subhorizontal or inclined. Furthermore, suevite particles in the Bosumtwi crater, Ghana, are also aligned in a subhorizontal plane, evident form analysis of drillcore (Morris et al. 2007).

With regard to atmospheric turbulence suevite deposition may be similar to that of volcanoclastic deposits. The transport, deposition and particle fabrics of volcanic materials have been studied in large detail. For example, Best (1992) found that grain fabrics in volcanoclastic mass flows depend on the flow regime, whereby particle long axes may be oriented either parallel or transverse to the flow direction. There is still considerable discussion regarding the cause for the observed disparate long axis orientations. Capaccioni et al. (2001) suggested that in gas-solid-suspensions, such as pyroclastic flows, alignment of elongate particles is achieved by shearing parallel to the depositional surface, either due to rotation transverse to flow direction or sliding and drag parallel to flow direction. With increasing particle density, long axes will undergo shearing, resulting in a preference of long axis alignment parallel to the flow direction. Branney and Kokelaar (1992) found that voluminous ignimbrite beds can form by incremental deposition, whereby observed shape fabrics within ignimbrites result from differential shearing caused by viscous flow between the individual ignimbrite flows. In this case, particle alignment will be well developed in the lower and upper parts of a flow unit, but poorly developed within a flow. The notion that particles in pyroclastic rocks display a distinct shape-preferred orientation (either concentric or radial) is widely accepted and used successfully to identify pyroclastic flow directions (Schmincke and Swanson 1967). Nonetheless, the reason for the generation of bi-modal alignment of particle long axes remains unclear.

There is no statistically significant preferred plunge of the ellipsoid long axes in the Seelbronn samples (Fig. 4.4b). By contrast, most of the long axes of the radially oriented shape fabric ellipsoids from Aumühle plunge toward the crater center. In pyroclastic deposits elongate clasts are typically radially disposed and indicate a change in the flow regime from turbulent to laminar with increasing distance to the eruptive source. Alternatively, laminar flow may arise due to the flow regime acting at the base of a pyroclastic flow (Kamata and Minura 1983). The variation in long axis orientations of suevite particles may well be due to fluctuations in viscosity and short-term material supply or variable subsurface topography, collectively inducing temporal and spatial variations in the flow regime during deposition of outer suevite.

The shape-preferred radial and concentric orientations of elongate Aumühle and Seelbronn suevite clasts and their preferred plunge direction toward the crater center indicate that the outer suevites may not have formed only as a consequence of fall-back from a collapsing ejecta plume. A transport mechanism of the suevites by horizontal flow away from the crater center under viscous conditions may well be considered as well. This hypothesis is corroborated by the lack of sorting in the outer crater suevite, which suggests that the suevites underwent horizontal transport under a highly turbulent flow regime. Moreover, the polarity of viscous flow is indicated by the plunge of elongate particles toward the crater, e.g., at Aumühle, pointing to outward directed, surface-parallel shearing upon deposition of outer

suevite.

In volcanic settings, fall-out deposits from ejecta plumes are typically well-sorted, fine-grained, and display normal gradation (e.g., Fisher and Schmincke 1984). Suevite deposits similar to such volcanogenic ones were observed in core samples from the upper graded unit of the inner crater suevite (1973 research drilling project: Stöffler 1977) and in the Bosumtwi crater (Koeberl et al. 2007). Based on this information, Osinski et al. (2004) proposed that the fine-grained, sorted basal layers of the outer suevite represent "true" fall-out suevite overlain by a main mass of "surficial" suevites. We propose that suevite clasts were transported away from the crater by viscous flow after falling back to the surface, akin to the viscous flow regime in pyroclastic flows. A combination of initial fall-back followed by viscous basal flow can account for the structural characteristics of the outer suevite of the Ries crater.

5. Quantitative stereometric analysis of Suevite drill cores from the Ries impact crater

5.1. Abstract

For a further differentiation of the emplacement modes of fall-back and horizontal transport, the grain shape, grain size distribution, and content of particles in several drill core sections inside and outside the crater were investigated. These stereometric results imply a secondary comminution process after the shock wave passage, pressure release, and transient cavity formation, where the clasts were comminuted and sorted as a function of their size, density, and distance from the crater center, and where particle-particle interactions can occur. A secondary milling and sorting process, in a gas dominated suspension, seems to be likely, similar to a pyroclastic flow - or surge - like process as proposed by Newsom et al. (1986), 1990, and Bringemeier (1994). Only the upper most part of the inner crater suevite seems to be fall out from the ejecta plume as proposed by Stöffler (1977).

Photo prints were produced by H. J. Nier, A. Dittmann (MfN) and the author. Thin sections were prepared by R. Knöfler (MfN) and J. Jacob (MfN) helped with the thin section templates for stereometric analyses. K. Born (MFN) assisted with the scanning electron microscopy (SEM) measurements. All scanning electron microscopy imaging, image analyses, processing of the data, text, and interpretation were performed by the author. Methods and results were discussed with Michel Jébrak and Dieter Stöffler. Richard Grieve helped with English correction.

All used drill core photographs, thin section photographs, secondary electron (SE) pictures and their corresponding image templates are summarized in Appendix 1. All plotted grain size distributions of suevite for lithic clasts and melt particles of all drill cores are summarized in Appendix 2. All corresponding cumulative frequency diagrams of grain size distribution are summarized in Appendix 3.

5.2. Introduction

The only highly energetic observable geological processes on earth are volcanoclastic eruptions. Knowing that the P-T conditions are lower than at the moment of an impact and that the mass and mass flux of the ejected particles is different, we propose that volcanic eruptions can be considered for comparison of the late phases of the transport and sedimentation processes of the clastic material during impact. Pyroclastic depositions can be differentiated in three mechanisms: fall, flow, and surge (e.g., Sparks and Walker 1973, Francis and Oppenheimer 2004). Pyroclastic fall is the fall-out of ejected material out of the ejection column or from convective clouds rising from a flow or a surge. Pyroclastic flow and surge involve the lateral transport of hot fragmental material and gas in ground-hugging density flows. Whereas pyroclastic surges are dilute pyroclastic density currents in which collisions between particles play a limited role, the overlying pyroclastic flow is a granular fluid-based pyroclastic density current, where particle collisions become important (Branney and Kokelaar 2002). However, transitions and interactions between fall, flow, and surge complicate the interpretation of the resulting deposits. Whereas fall-out deposits are usually well sorted, flow and surge deposits are mainly poorly sorted, with the initial grain size distribution being modified by superimposing transport-related sorting (Francis and Oppenheimer 2004). Furthermore, in pyroclastic flow and surge depositions the grain size decreases with distance from the source, while the sorting increases (e.g., Moore 1981; Allen and Cas 1998). In total, the crystal components become less sorted and more abraded from fall-out to pyroclastic surge to pyroclastic flow, consistent with increasing particle concentration in the transporting currents (Taddeucci and Palladino 2002).

In this Chapter, stereometric parameters of lithic clasts and melt particles of different suevite units are used to reconstruct the evolution of the Ries crater suevite. In order to differentiate between the different emplacement modes of suevite deposits, the shape and size distribution of particles in several drill core sections was measured: Nördlingen, inside the inner ring; Enkingen, at the inner ring; Wörnitzostheim, between inner ring and crater boundary; and Otting, outside the crater (Fig. 3.1). Until now, the most common assumption was that, upon collapse of the ejecta plume, the plume material fell back into the crater and outside the crater forming the suevite (e.g., Stöffler 1977; von Engelhardt and Graup 1984; von Engelhardt 1997). This Chapter shows that the genesis of the suevite cannot be explained by such a simple fall-out process.

5.3. Analytical Methods and sample selection

Throughout the whole cores of Enkingen and Otting, the plane surfaces of the half cores were photographed in high resolution (2 x magnifications with 240 dpi). For FBN73 and

Wörnitzostheim half cores, each suevite subtype was photographed. The maximum size of the photographed core pieces was 10 times 50 cm. Polished thin sections were produced at various sampling depths, summarized in Table 3.1. The thin sections were first scanned by using a film scanner, with transmitted light, and afterwards scanned using two crossed polarization foils (10 x magnifications with 240 dpi). The maximum size of the photographed thin sections was 2.2 times 4 cm.

The photographs of the half cores were used to identify rock and melt particles in the suevite over a representative area of 10 times 10 cm in each photograph. The characterization of the particles was based on macroscopic observations. The particle outlines were manually traced in standard image software, using different coloring for rock and melt particles respectively. These templates were then processed by image analyses software "ImageJ" for analyzing particle geometrie. A minimum particle size of 1 mm could be captured. For a complete grain size analysis, particles with diameters of 1 to 63 mm (0 to -6 ϕ), which covers the best detectable grain sizes, were taken into account (Fig. 5.1a, Appendix 1).

The scanned photographs of the thin sections were printed and the lithic clasts and melt particles were colored by different overhead markers on an overlain foil. The characterization of the particles was based on optical microscopy. The foil was scanned and prepared for image analyses by using standard image software. The particle size range covered by this analysis was 0.1 to 10 mm. For a complete grain size analysis, particles with diameters of 0.25 to 4 mm (2 to -2 ϕ) were taken into account (Fig. 5.1b, Appendix 1).

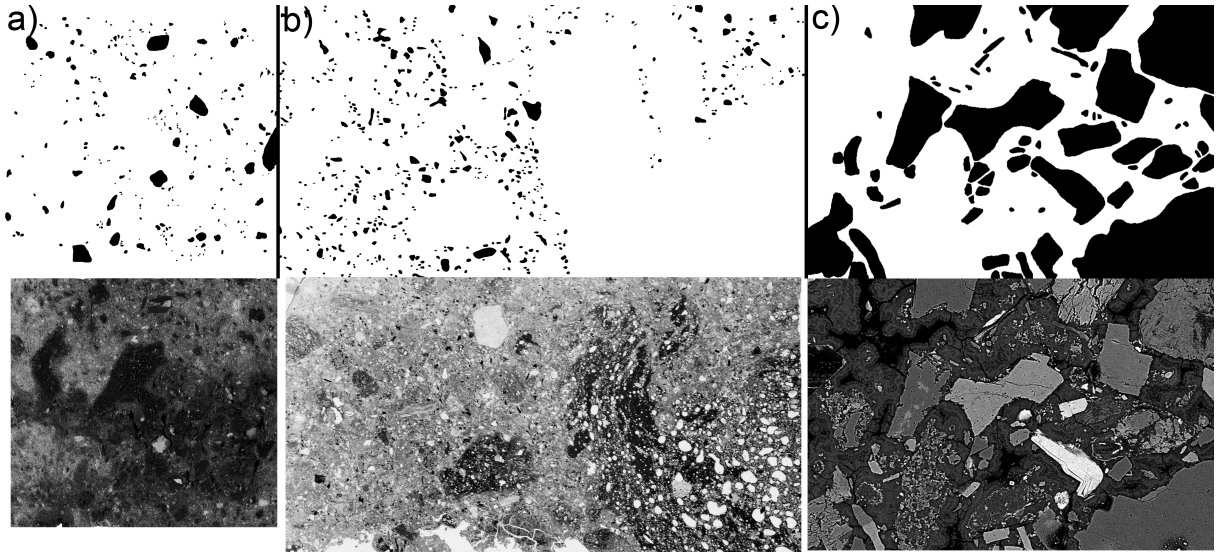

Fig. 5.1.: Example of image templates of colored particles used for processing by image analysis software "ImageJ". Lithic clasts detected from Otting drill core on a) plane surface of half core 0.2 - -0.3 m depth. Picture width = 10 cm; b) thin section of 0.3 m depth. Picture length = 3.4 cm; c) SEM pictures of 0.3 m depth. Picture width = 0.7 mm. Large white areas represent melt particles, matrix, and cavities. All image templates are summarized in Appendix 1.

Additionally, SEM studies were performed on samples from various depths in the drill cores. For this study, a JEOL JSM-6300 Scanning electron microscope equipped with a

Bruker AXS EDX detector, operating at 15kV and a beam current between 1 and 10 nA was used. The SEM pictures at 250 times magnification were also analyzed by Adobe Photoshop and ImageJ, with different coloring of lithic clasts and melt particles. The characterization of the particles was also based on optical microscopy. The minimum captured particle size was 5 - 10 μm. For a complete grain size analysis, particles with diameters of 0.016 to 0.25 mm (-2 to -6 ϕ) were taken into account (Fig. 5.1c, Appendix 1).

Particle parameters determined by the image analysis software are:

- area of all particles and total area of the sample for analyzing the content of matrix, lithic clasts, and melt particles larger than 1 mm by percentage;

- major and minor axis of the best fitting ellipse to the particles (from particles not intersected by image boundary) for analyzing the maximum particle size (mean value of grain sizes of 10 largest particles (Tucker 1996)), aspect ratio of particles larger than 1 mm (ratio of the minor axis to the major axis of a particle), and grain size distribution of lithic clasts and melt particles (0.016 - 63 mm).

Reworking of ejected material of an impact process likely affects the clast population of the ejecta. The original ejected clast shapes are no longer recognizable due to transportation processes. However, the grain sizes and shapes, which were modified by transport and sedimentation processes, can be analyzed by the mentioned stereometric methods. From these data, conclusions to the nature of the transport and sedimentation processes can be drawn (Kokelaar and Romagnoli 1995).

5.4. Results of stereometric analysis and comparison between drill cores

5.4.1. Content of lithic clasts and melt particles

The result of the analyses of the melt and lithic clast content of all drill cores is shown in Fig. 5.2.

The FBN73 shows the lowest content of melt particles larger than 1 mm. The melt content, as well as the lithic clast content, increase in each cycle of the sedimentary unit (296 - 314 m) from almost zero up to 15% melt content and 35% lithic clast content. In the graded suevite (314 - 330 m), the melt and lithic clast contents are almost equal and increase with depth from 4% up to about 30%. In the upper part of the melt-rich suevite unit (330 - 380 m), the contents of the melt and lithic clasts are constant highly at about 15% and 10%, respectively. From 380 to 450 m, the clast content becomes highly variable and varies from 5 up to 25%. Below 450 m the melt content decreases with depth up to the transition to the melt-poor suevite at 520 m, where the melt content is almost not detectable by macroscopic investigations. The lithic clast content increases with depth up to 40% and decreases from 520 m to the bottom of

the suevite unit to about 15%. In the suevitic dike at 642 m, the melt and lithic clast contents are 6% and 10%, respectively.

The melt content of Enkingen shows an exponential increase with increasing depth down to 40 m, with a maximum of 60% melt. At 40 m, the melt content decreases abruptly and increases again with depth down to 66 m to 60%. Below 66 m, the suevite is increasingly intersected by coherent melt layers and passes into a compact impact melt rock below 85 m. The lithic clast content is constant throughout the core, varying between 5 and 20%, and is always lower than the melt content.

Down to 80 m, the melt content of Wörnitzostheim is higher than the lithic clast content. It increases down to 40 m and remains at about 30 to 40% down to 80 m. At the transition to the Bunte Breccia below 80 m, a melt-poor zone can be observed, where the melt content decreases to 5 to 10%. However, the melt content becomes highly variable due to rare but large melt particles. The lithic clast content is slightly increasing throughout the whole core.

For the Otting drill core, down to 6 m depth the melt content of about 20% is higher than the lithic clast content (5%). Below 6 m, the melt content decreases slightly with depth down to 10% at the transition to the Bunte Breccia. The lithic clast content is rather constant throughout the whole core.

5.4.2. Aspect ratios of lithic clasts and melt particles

The result of the analyses of the aspect ratio (ratio of the minor axis to the major axis of a particle) of the lithic clasts and melt particles of all drill cores is shown in Fig. 5.3. For all drill cores, the aspect ratio of the lithic clasts is always higher than for the melt particles. The lithic clasts show similar aspect ratios between 0.6 and 0.7 for all drill cores and all depths. The aspect ratio of the melt particles is for FBN73 $\sim$ 0.6, for Enkingen $\sim$ 0.5, for Wörnitzostheim between 0.5 and 0.6, and for Otting 0.6. Whereas the aspect ratio of the melt particles of Wörnitzostheim is with 0.5 smaller between 40 and 80 m compared to the rest of the drill core, the aspect ratio for the other drill cores is always constant with depth.

5.4.3. Maximum grain size of lithic clasts and melt particles

The result of the analyses of the maximum grain size (mean value of grain sizes of 10 largest particles) of the lithic clasts and melt particles of all drill cores is shown in Fig. 5.4.

The maximum grain size of the lithic clasts and melt particles in the sedimentary units (296 - 314 m) and the graded suevite (314 - 330 m) of FBN73 increases with depth, varying between 5 and 20 mm. Whereas in the upper part of the melt-rich suevite (330 - 1 380 m) the maximum grain size is constant at $\sim$ 15 mm, it becomes highly variable between 380 and 520 m, with variations from 10 to 25 mm grain size for the lithic clasts and 5 to 20 mm for the melt particles. However, a decreasing trend of the maximum grain size for the melt particles

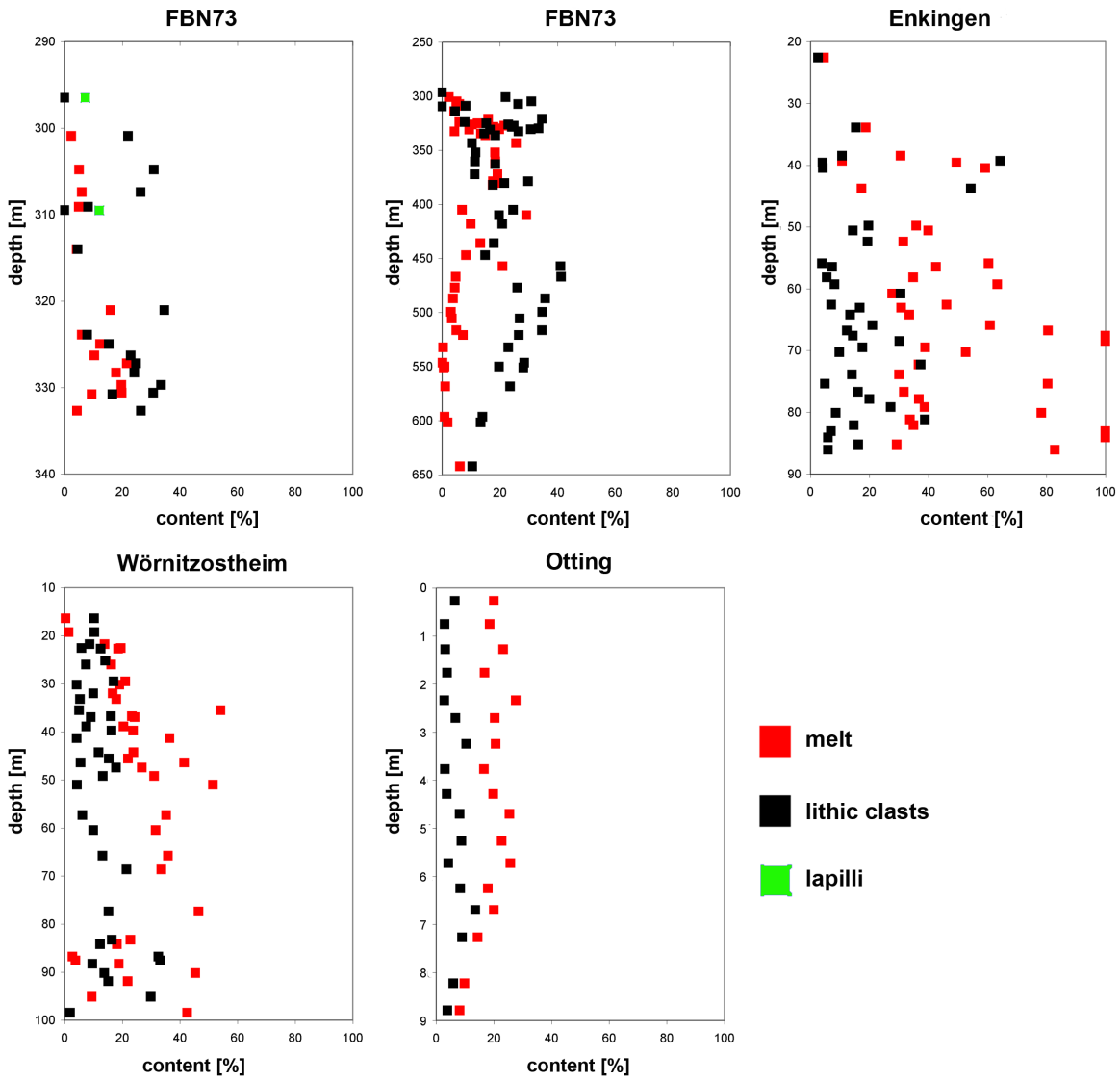

Fig. 5.2.: Melt and lithic clasts content of drill cores FBN73 (296 - 332 m), FBN73 (296 - 642 m), Enkingen, Wörnitzostheim, and Otting. Sampling width: 1 to 63 mm (0 to -6 ϕ).

is detectable. Below 520 m, almost no melt particles can be macroscopically detected. The maximum grain size of the lithic clasts decreases from 25 to 10 mm with depth, until 600 m. The range and maximum grain size of the lithic clasts and melt particles in the suevitic dike at 642 m is similar to the overlying suevite units.

For Enkingen the maximum grain size for all particles increases from 5 to 45 mm with depth down to 40 m and further down decreases down to 66 m depth to 10 mm for the lithic clasts and 15 mm for the melt particles. Below 66 m, with the beginning of occurrence of the coherent melt layers, the maximum grain size is constant for the lithic clasts, at 10 to 30 mm, but shows high variations for the melt particles, ranging between 15 and 60 mm grain size. The maximum grain size of the melt particles always exceeds the maximum grain size of the lithic clasts.

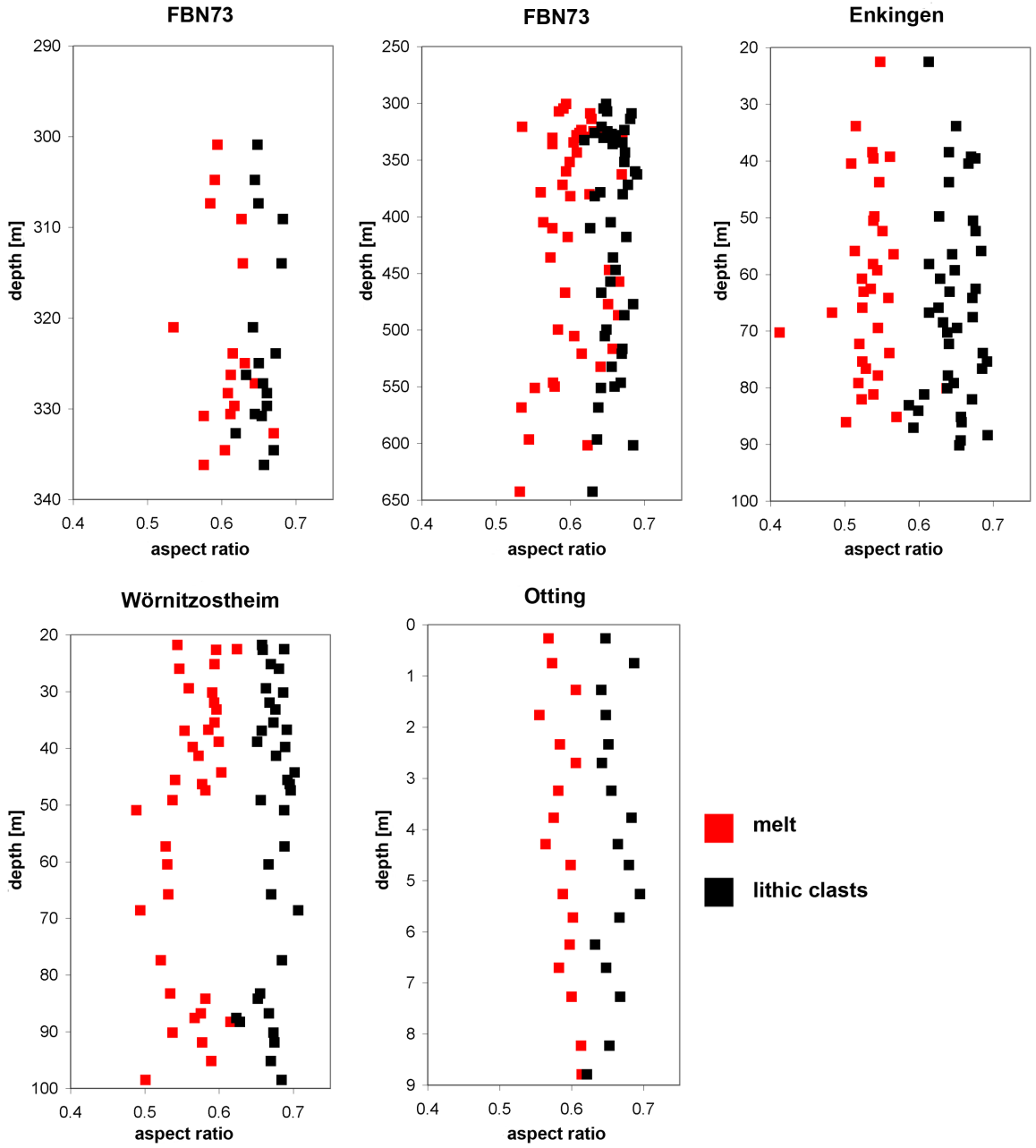

Fig. 5.3.: Aspect ratio of lithic clasts and melt particles of drill cores FBN73 (296 - 332 m), FBN73 (296 - 642 m), Enkingen, Wörnitzostheim, and Otting. Sampling width: 1 to 63 mm (0 to -6 ϕ). Aspect ratio equals ratio of the minor axis to the major axis of a particle.

For Wörnitzostheim, the maximum grain size of the lithic clasts (5 to 10 mm) and melt particles (1 to 15 mm) is slightly increasing with depth down to 80 m, with the largest increase observed in the upper-most layers down to 25 m. Below 80 m, to the transition to the Bunte Breccia, the maximum grain size decreases down to 5 mm for the lithic clasts and 10 mm for the melt particles; except in samples with rare, but large, melt particles, which can partially increase the maximum grain size up to 30 mm.

The maximum grain size of the melt particles of the Otting drill core is between 10 and 20

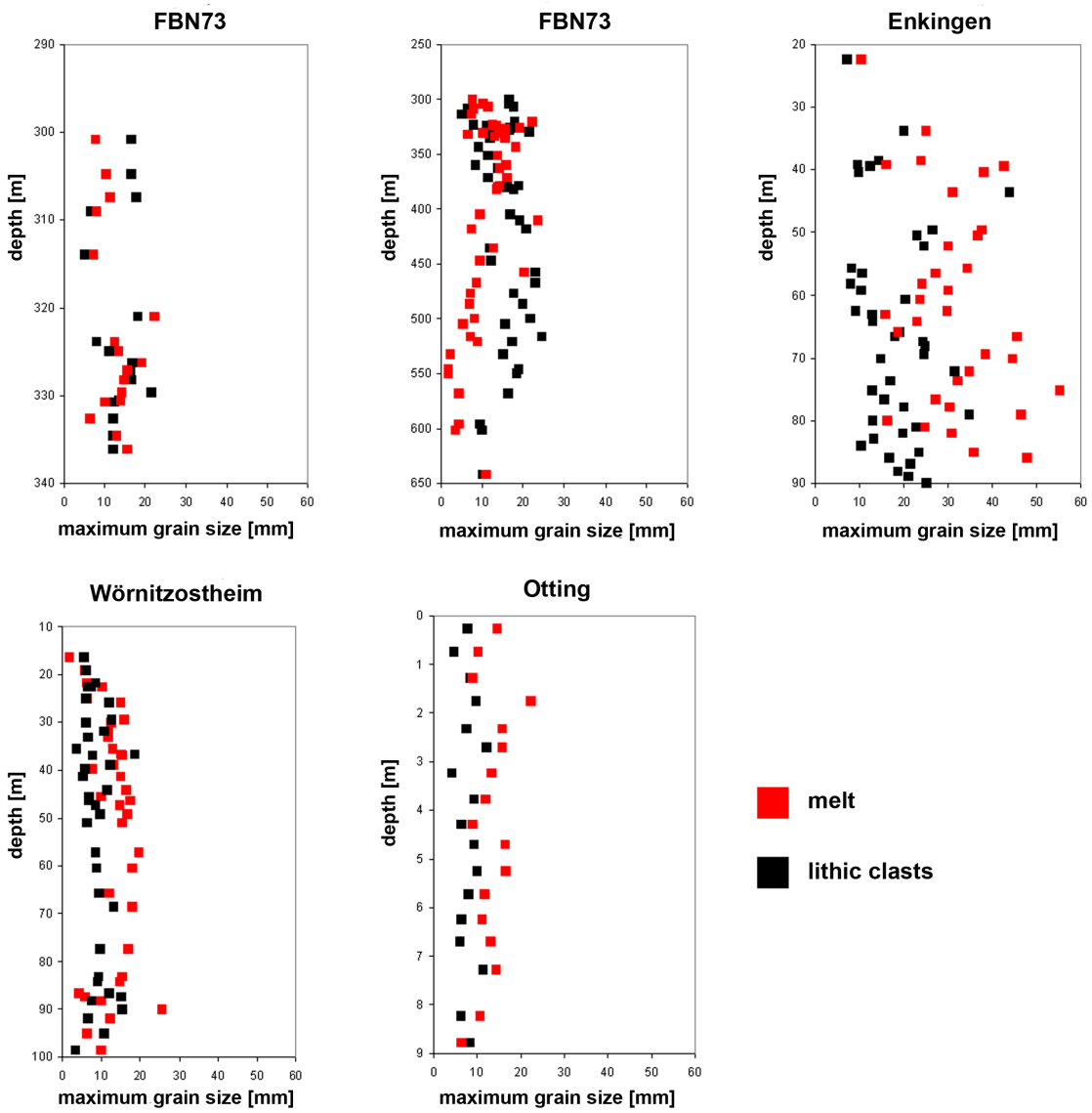

Fig. 5.4.: Maximum grain sizes of lithic clasts and melt particles for drill cores FBN73 (296 - 332 m), FBN73 (296 - 642 m), Enkingen, Wörnitzostheim, and Otting applied to data up to 63 mm size.

mm and constant down to 7 m depth and below 7 m slightly decreases with depth to 5 mm. The maximum grain size of the lithic clasts is between 5 and 15 mm and constant throughout the core. The maximum grain size of the melt particles always exceeds the maximum grain size of the lithic clasts.

5.4.4. Grain size distribution of lithic clasts and melt particles and fractal dimension

Almost all investigated samples show a log normal grain size distribution (an example is shown for Otting at 2.71 m depth in Fig. 5.5a). Due to the fact that common sedimentological parameters as mean and median grain size, and sorting coefficient are not defined for log

normal grain size distributions, a different statistical parameter must be considered. The fractal dimension can be used for quantitative comparison of log normal distributed grain sizes (Bashkirov and Vityazev 1996). The fractal dimension is based on a size distribution which follows a power law ($N_r \cdot r^{-D} = N_c$) where N_r is a constant, which depends on the number of measurements, r equals $\sqrt{(A \cdot B)}$ (A=length of the major axis, B=length of minor axis) and functions as the grain size parameter, D is the fractal dimension, and N_c number of particles with sizes larger than r. By plotting log r against N_c the slope D of the curve represents the fractal dimension (Fig. 5.5b). High D values imply processes of high energy, whereas lower D values can result either from lower energy fragmentation process or are a result of fragmentation of a large body of fragile material. Differences of fractal dimensions on a microscopic and a macroscopic scale are interpreted as a result of different fragmentation processes (Rousell et al. 2003).

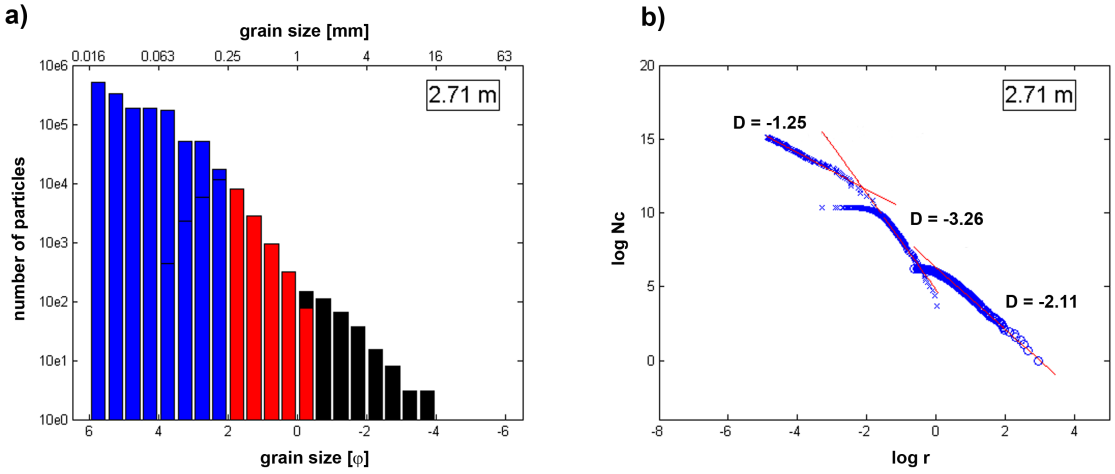

Fig. 5.5.: a) Grain size distribution of suevite of Otting (2.71 m) for lithic clasts. Grain size equals $r = \sqrt{(A \cdot B)}$ where A = length of clast major axis and B = length of minor axis. Black bars: from macroscopic analysis with sampling width of 1 to 63 mm (0 to -6 ϕ), red bars: from thin section analysis with sampling width of 0.25 to 4 mm (2 to -2 ϕ), blue bars from SEM analyses with sampling width of 0.016 to 0.25 mm (6 to 2 ϕ). At 0 to -0.5 ϕ the red bar of thin section analysis overlies the black bar of macroscopic analysis. Grain-size distributions for all samples are summarized in Appendix 2. b) Cumulative frequency diagram of grain size distribution of suevite of Otting (2.71 m) for lithic clasts. Right line: from macroscopic analysis with sampling width of 1 to 63 mm, middle line: from thin section analysis with sampling width of 0.1 to 1 mm, right line: from SEM analyses with sampling width of 0.01 to 0.25 mm. $r = \sqrt{(A \cdot B)}$ where A = length of clast major axis and B = length of minor axis. N_c = number of particles whose sizes are greater than r. D = slope of red line, $-D$ equals "fractal dimension". All cumulative frequency diagrams are summarized in Appendix 3.

The result of the grain size distribution represented by fractal dimension of all drill cores of the lithic clasts is shown in Fig. 5.6 and of the melt particles in Fig. 5.7. All grain size distribution and cumulative frequency diagrams of all investigated samples are given in Appendix 2 and 3. Macroscopic scale represents grain sizes between 2 and 63 mm, microscopic scale grain sizes between 0.25 and 2 mm, and SEM scale between 0.016 and 0.25 mm.

For FBN73, as well as for all other dill cores the fractal dimension of microscopic scale is

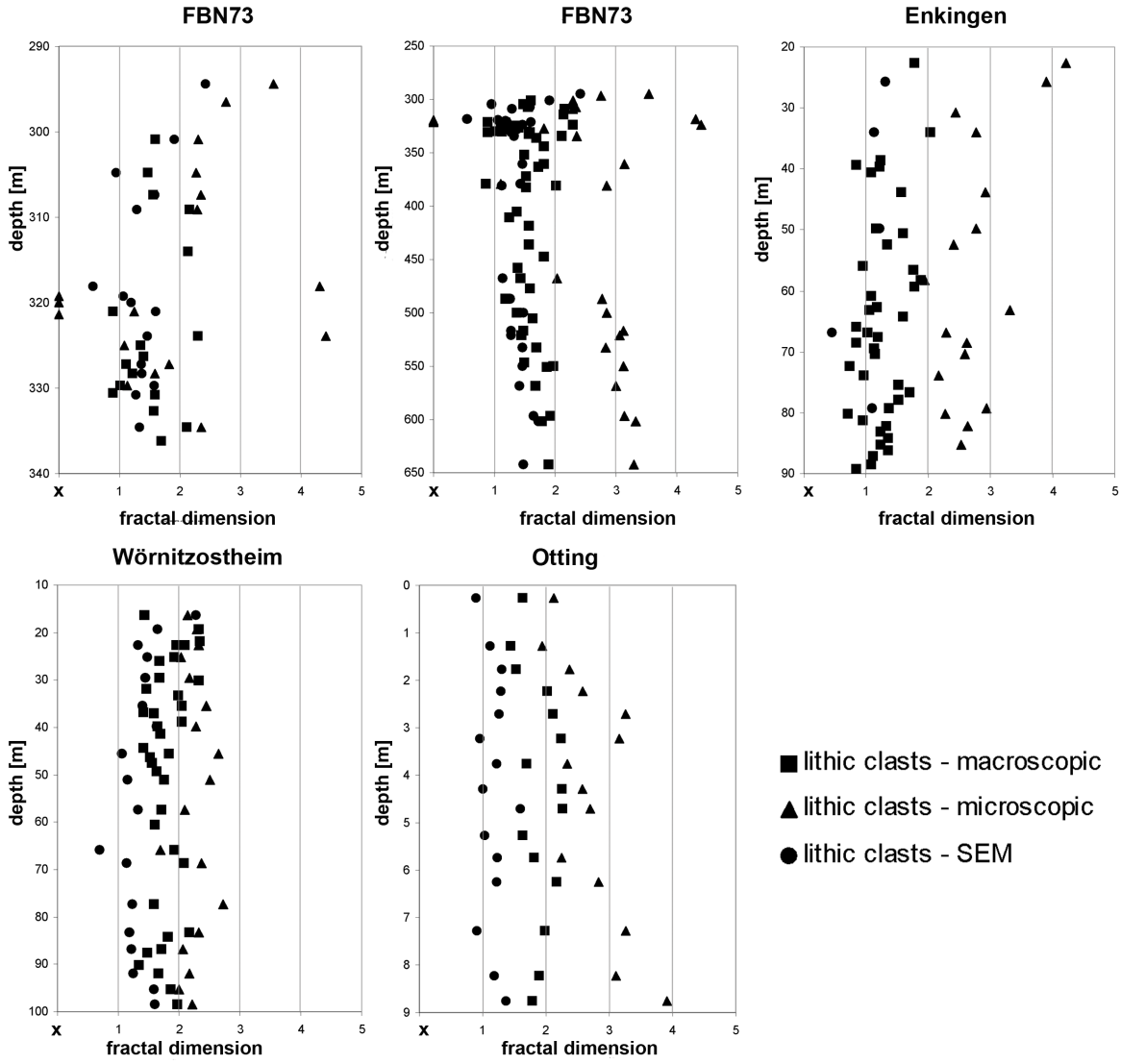

Fig. 5.6.: Fractal dimension of lithic clasts for drill cores FBN73 (296 - 332 m), FBN73 (296 - 642 m), Enkingen, Wörnitzostheim, and Otting from cumulative frequency diagrams. Distinguished between fractal dimension measured on macroscopic (4 to 63 mm (-2 to -6 ϕ)), thin section (0.25 to 4 mm (2 to -2 ϕ)) and SEM scale (0.016 to 0.25 mm (6 to 2 ϕ)) scale. X means no log normal grain size distribution.

generally higher than for macroscopic scale. The fractal dimension of SEM scale is always similar to the macroscopic scale or smaller. In the sedimentary units of FBN73 (296 - 314 m), the fractal dimension of the lithic clasts decreases with depth. The highest value of the fractal dimension in the whole core can be observed in the upper part of the graded suevite (314 - 330 m). Down to 324 m, the fractal dimension of the microscopic scale is either very high, with about D = 4.4, or the grain sizes are so well sorted that a determination of the fractal dimension is not possible (represented as x in Fig. 5.6). Note that from mathematical definition (e.g., Tucker 1996), the terminus “sorting coefficient” is just defined for grain size distributions showing a normal distribution. For log normal distributions, the fractal dimension must exclusively be used for comparison. The fractal dimension of the macroscopic and SEM scale

is almost constant throughout the graded suevite, with D = 1.5 to 2. From 330 m to 520 m, the fractal dimension of macroscopic and SEM scale is constant and similar to the graded suevite. The fractal dimension of the microscopic scale drops down to about D = 3. Below 520 m, the fractal dimensions in all scales are slightly increasing with depth and become similar for the suevitic dike at 642 m.

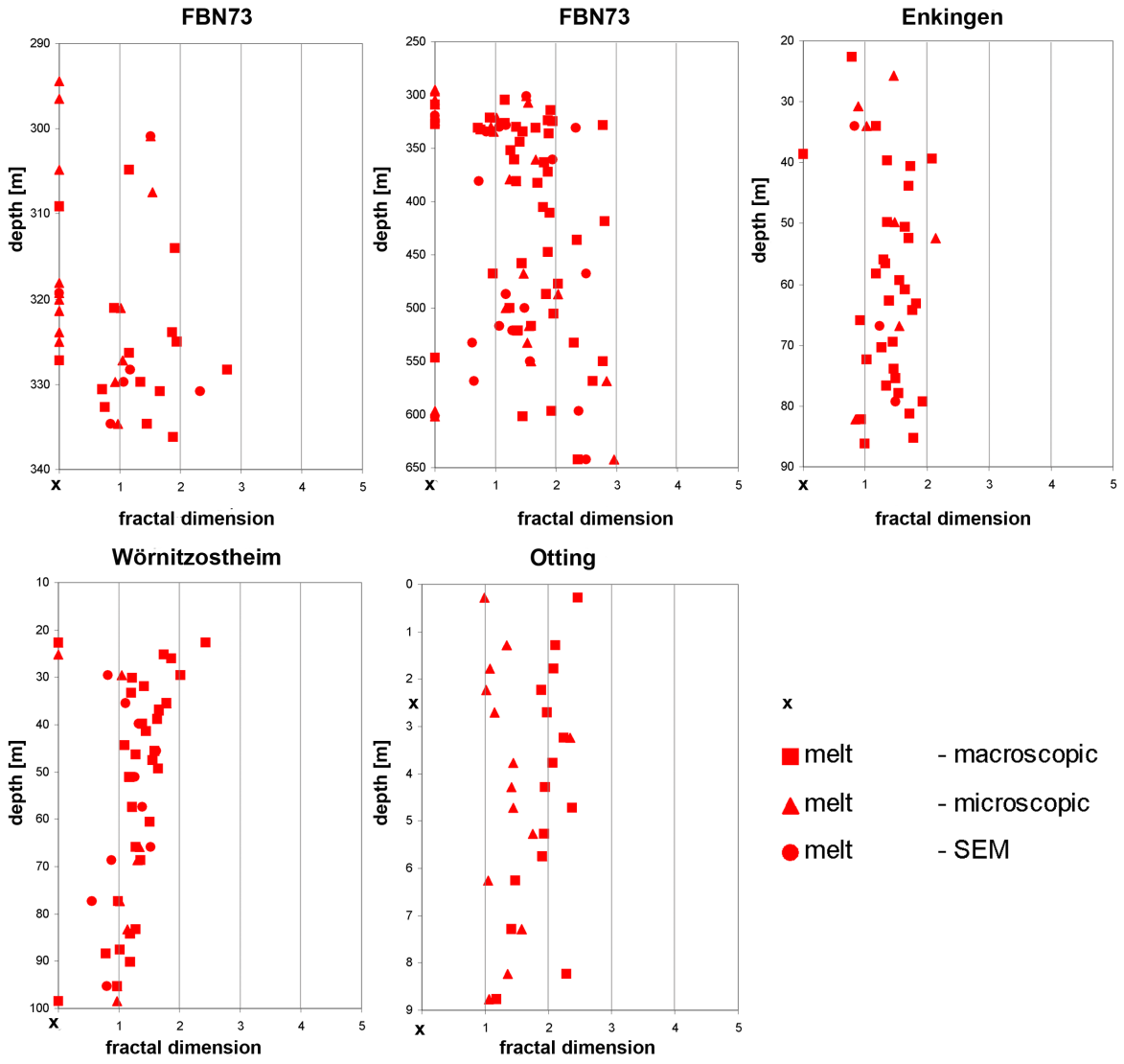

Fig. 5.7.: Fractal dimension of melt particles for drill cores FBN73 (296 - 332 m), FBN73 (296 - 642 m), Enkingen, Wörnitzostheim, and Otting from cumulative frequency diagrams. Distinguished between fractal dimension measured on macroscopic (4 to 63 mm (-2 to -6 ϕ)), thin section (0.25 to 4 mm (2 to -2 ϕ)) and SEM scale (0.016 to 0.25 mm (6 to 2 ϕ)) scale. X means no log normal grain size distribution.

The grain size distribution of the melt particles of FBN73 is mostly well sorted at the microscopic scale. Due to this fact the fractal dimension in microscopic scale cannot be determined and is represented by x in Fig. 5.7. The fractal dimension for macroscopic and SEM scale is homogenous throughout the core, varying between D = 1 and 2, down to 520 m and slightly increasing below 520 m.

At Enkingen, the fractal dimensions of the lithic clasts show also the highest value in microscopic scale at the top of the suevite, with D $\sim$ 4. Below 30 m, the fractal dimension in microscopic scale is constant throughout the core, with D $\sim$ 2.5. The fractal dimensions of macroscopic and SEM scale slightly decreases with depth, from D $\sim$ 2 to D $\sim$ 1. The fractal dimension of the melt particles is rather similar with D = 1 to 2.

The fractal dimension of the lithic clasts of Wörnitzostheim is rather homogenous throughout the whole core. The fractal dimension of the macroscopic scale varies between D = 1.5 and 2, for the microscopic scale between D = 2 and 2.5, and for the SEM scale between D = 1 and 1.5.The fractal dimension of the melt particles is rather similar for all scales and slightly decreases with depth, from about D = 2 to about D = 1.

At Otting, the fractal dimension of the lithic clasts is rather homogenous throughout the whole core for the macroscopic and SEM scales. The fractal dimension at the macroscopic scale varies between D = 1.7 and 2.2, and for the SEM scale between D = 0.9 and 1.4. At the microscopic scale, the fractal dimension increases down to 3 m from D = 2 to 3, decreases down to 6 m from D = 3 to 2, and increases again down to the transition to Bunte Breccia at 9 m to D = 4. An exception to the other cores is the fractal dimension of the melt particles, where the fractal dimension at the microscopic scale is lower than at the macroscopic scale. The fractal dimension at the macroscopic scale slightly decreases with depth, from about D = 2.5 to 1.2, whereas the fractal dimension at the microscopic scale slightly increases, from about D = 0.9 to 1.2. At the SEM scale almost no melt particles can be detected.

5.4.5. Comparison of the characteristics of drill cores

The Ries suevites can be divided into stratigraphic subtypes. They differ in maximum grain size, melt content, fractal dimension, and grading. These subtypes are distinctly different for the central part (FBN 73) and the outer part of the inner crater (Enkingen, Wörnitzostheim). The results of aspect ratio, maximum grain size, and grain size distribution in lateral comparisons are shown in Fig. 5.8. Due to the strong variations of the lithic clasts and melt content with depth, this kind of diagram is not meaningful for a comparison of this parameter between the drill cores. For comparison of the content, Fig. 5.2 is used.

The suevite inside the inner ring (FBN73) of the crater shows the lowest content of melt particles. In contrast, in the suevites at the inner ring (Enkingen) and between inner ring and crater boundary (Wörnitzostheim), the maximum grain size and content of melt particles increase with depth. At the inner ring, the suevite passes into a compact impact melt rock, whereas in the suevite between inner ring and crater boundary a melt-poor zone of suevite can be observed at the transition to the Bunte Breccias. In total, the maximum grain size of the melt particles decreases and the roundness increases with distance to the crater center (from Enkingen to Otting). Whereas the fractal dimension of the melt particles increases with depth

for FBN73, it decreases at Enkingen, Wörnitzostheim and Otting site. Only at Otting, the fractal dimension at the microscopic scale is lower than at the macroscopic scale. The highest values of fractal dimension, up to well sorted, can be observed in the inner part of the crater (FBN73).

The lowest content of lithic clasts is shown by the outer crater suevite (Otting). In total, the content of lithic clasts decreases with distance from the crater center (from FBN73 to Otting) and therewith the maximum grain size (from Enkingen to Otting). However, the mean roundness of the lithic clasts is similar for all drill cores. The fractal dimension of the lithic clasts for the macroscopic scale increases from Enkingen to Otting. The fractal dimension at the microscopic scale is always higher than at the macroscopic scale. The highest fractal dimension at the microscopic scale could be observed in the uppermost layer for FBN73 and Enkingen; whereas, at Otting, it is in the lowermost layer. While the fractal dimension of FBN73 increases with depth, it decreases for Enkingen and Wörnitzostheim.

5.5. Discussion

Deposition from lateral transport

The clast size distribution of impact ejecta is usually interpreted by the cumulative number N(m) of particles equal or greater than a grain size r (e.g., Gault et al. 1963, Bashkirov and Vityazev 1996). The impact fragmentation provides a fractal size distribution function of fragments $N_r\ r^{-D}=N_c$ as described in sub-Chapter 5.4, and the fractal number D falls within the range between 1.5 and 4.5.

As shown in Fig. 5.6, the D values of the lithic clasts are on average almost always higher at the microscopic scale than at the macroscopic scale. Regionally, the D value at the macroscopic scale increases from Enkingen to Otting and therefore increases with increasing distance from the crater center. A higher fractal dimension at the microscopic scale, as observed in most of the samples, can also be observed for the grain size distribution of the Vredefort pseudotachylite (Hisada 2004). Such variations of the D values are reached if fragmented and ejected particles are subjected to further fragmentation processes (Burgisser and Gardner 2006; Kaminski and Jaupart 1998). Usually abrasion and refragmentation of the larger particles results in an increase in the D value. Due to the fact that this fragmentation process is less important for smaller particles, the D value will rise more at the microscopic scale than at the macroscopic scale as a result of the fragmentation process (Fig. 5.5b). This bifractality could be related to the two-stage nature of impact fragmentation processes itself (Martelli et al. 1994). The first stage leads to the formation of the crater in the target and the second stage is the total destruction of the target. The fractal dimensions of both stages are different, resulting in a shape turned grain size distribution with a lower D in the first stage

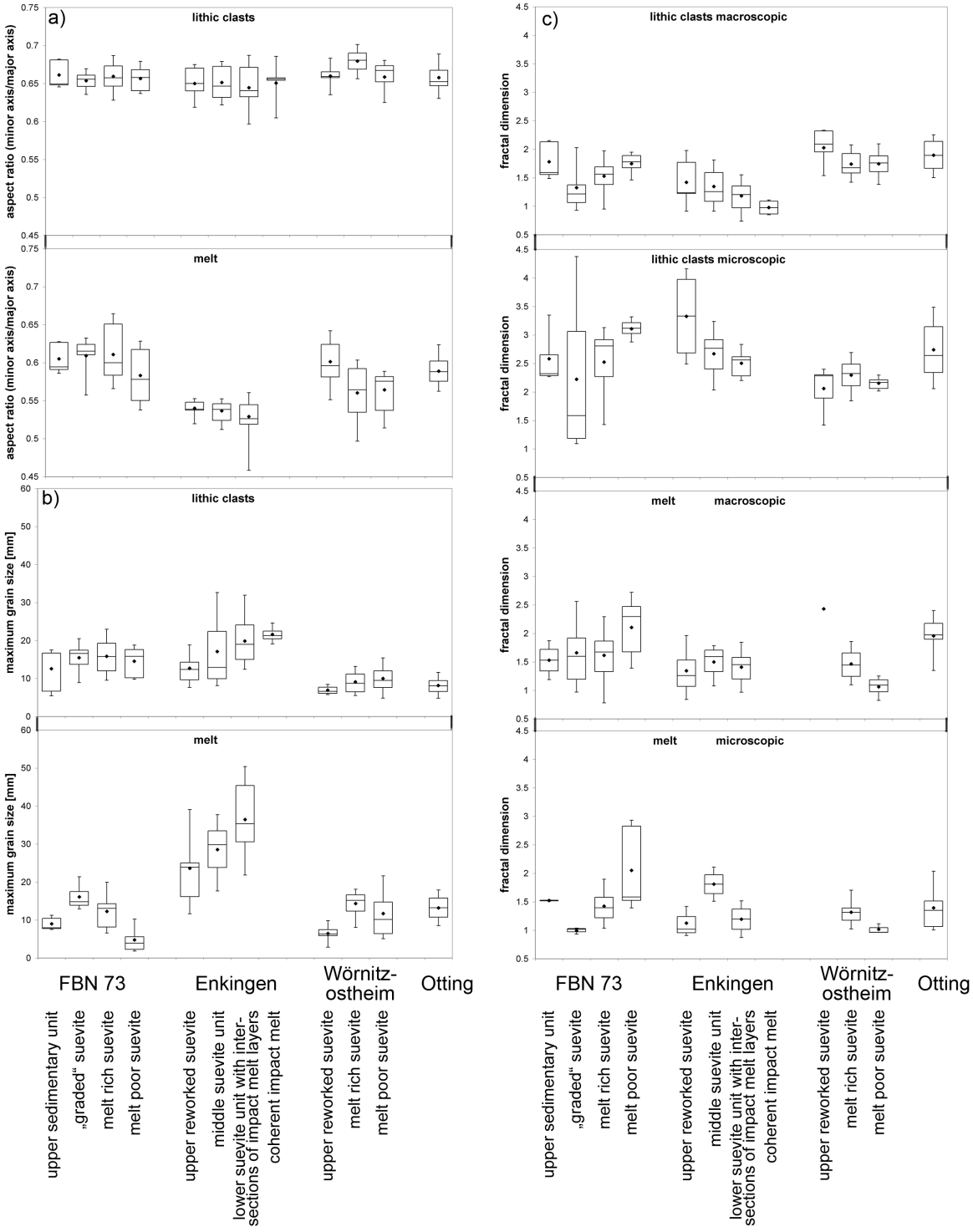

Fig. 5.8.: Comparison of stereometric results from FBN73, Enkingen, Wörnitzostheim, Otting separately for lithic clasts and melt particles: a) aspect ration, b) maximum grain size, c) fractal dimension. Each drill core is divided in its subunits as described in Chapter 3. Boxplots showing the 5, 25, 50, 75, and 95 Quantiles, points are the mean values.

than in the second (Bashkirov and Vityazev 1996).

Further fragmentation processes for the impact ejecta will be ejection, further transportation and sedimentation. If the late stage breakage is the dominant process, as happens for a fall-out

deposit from an ejecta plume, the total grain size distribution in a deposit will not depend on the distance to the center. As the D values of the suevites increase with distance from the crater center a gas-dominated suspension is required for transport in which particle-particle interactions can occur. Abrasion and refragmentation affect the grain size of the particles over the whole time of transportation (Kaminski and Jaupart 1998). A suspended-load fall-out occurs when particles carried mainly by turbulent motions of hot gases sediment form a pyroclastic cloud. This sedimentation process sorts clasts, as a function of size and density to the distance from the center. Due to the fact that this sorting process is more marked for larger clasts with distance from the center, the maximum grain size of clasts decreases accordingly, as observed in the Ries suevite (Fig. 5.4) (Burgisser and Gardner 2006). The particle-particle interaction and, therefore, the abrasion process during the transport out of the crater will result in a rounding process, at least for the fragile material, as observed in an increase of the aspect ratio of the melt particles with distance from the crater center (Fig. 5.3).

As shown for the pseudotachylites of Vredefort (Hisada 2004) and Sudbury (Rousell et al. 2003), the total D values decrease as a result of losing finer particles. The total D values become lower as the loss process affects more strongly the smaller grains than bigger grains and is negligible for large grain sizes (Ray 1999). Additionally, the D values of the finer grain scale decrease more rapidly compared to the macroscopic scale. The strong flattening of the cumulative frequency curve at the SEM scale, at least for Otting (Fig. 5.5), imply an additional process, before, during and/or after the transportation and refragmentation of the larger clasts, where only the finer grains of the Ries ejecta were lost. The lost finer fraction of the particles will either settle in well sorted layers, as observed in the FBN73 drill core between 296 and 314 m depth and at Wörnitzostheim between 16 and 19 m depth (Burgisser and Gardner 2006), or will be solved or transformed to secondary clay minerals by hydrothermal alteration processes effecting the suevite after its deposition (e.g., Osinski 2005, Muttik et al. 2008).

Differentiation between flow and surge deposition

Having proven that the particles of the suevite were transported with a lateral component from the inner ring outside of the crater, there remains the question if they were transported in a dilute suspension current like a pyroclastic surge or in a high concentrated, massive density current like a pyroclastic flow? In the comparison of surge and flow deposits from volcanic eruption, the crystal components become less sorted and more abraded from pyroclastic surge to pyroclastic flow, consistent with increasing particle concentration in the transporting current (Taddeucci and Palladino 2002).

Comparing the lower suevite unit of Wörnitzostheim (80 - 100 m) with the suevite of Otting shows several similarities: both have a gray to yellow color, the melt and lithic content is almost constant through the core, the finer fraction is completely transformed into secondary clay minerals (Förstner 1967, Osinski 2005). The stereometric results of these suevite units

(Fig. 5.8) show a weakly increasing aspect ratio, a decrease of the maximum grain size, and an increase of the fractal dimension from the lower Wörnitzostheim to Otting.

In contrast, the drill core of Enkingen is similar to the upper and middle part of Wörnitzostheim: they have the reworked suevite on top, reddish to brown color of the middle suevite, increasing melt content with depth, and slightly increasing lithic clast content. The only difference is that the Enkingen suevite passes below 86 m into an impact melt rock; whereas the Wörnitzostheim suevite is below 80 m underlain by the above described melt-poor suevite. The stereometric results of these suevite units (Fig. 5.8) show an increasing aspect ratio from Enkingen to Wörnitzostheim, a strongly decreasing maximum grain size, and a strongly increasing fractal dimension.

Compared to lateral transport systems, it appears that the particles of the suevite from the lower Wörnitzostheim and Otting were transported in a more dilute, less density stratified, turbulent suspension, travelling at high velocities and forming a wide-spread deposition similar to a pyroclastic surge deposit. In contrast the particles from Enkingen to Wörnitzostheim have to be transported in a density stratified current, where grain-grain interactions occur, travelling at lower velocities, similar to a pyroclastic flow deposit (Druitt 1998). Additionally, the high melt content of the Enkingen suevite implies a special kind of pyroclastic flow deposition: an ignimbrite. Pyroclastic flows, which are incipiently to densely welded, are called ignimbrites (Druitt 1998). Ignimbrites are composed of lithic clasts and volcanic glass. Due to the fact that hot glass is soft, the hot clasts sinter and flatten to form a denser, more coherent rock. It can be so extensive that the ignimbrite can be a dense mass of glass as observed in the lower part of the Enkingen drill core (Francis and Oppenheimer 2004). To produce a densely welded zone, the ignimbrite has to remain at high temperature and pressure long enough for welding. Thus, densely welded ignimbrites are typically found towards the bottom of thick deposits. The rest of the deposition typically forms an overlying partly welded zone that grades upward into unwelded pyroclastic flow deposition (Ross and Smith 1961). Whether the lower melt-rich part of the Enkingen drill core is an ignimbrite or a coherent impact melt rock can be solved by additional microscopic observation. The ignimbrite model is re-enforced by the embedding of the impact melt unit of Enkingen and the nature of the impact melt composed of a densely packed unit of centimeter to decimeter sized melt particles (Pohl et al. 2010).

Deposition out of the ejecta plume

The well-sorted grain size distribution of the melt particles in the upper part of the FBN73 suevite (296 - 330 m) cannot be explained by a simple impact process, as impact processes always result in log-normal grain size distributions (summarized by Turcotte, 1986). The increase with depth of the maximum grain size of the lithic clasts and melt particles in each sedimentary unit (296 - 314 m) and the graded suevite (314 - 330 m) (Fig. 5.4) imply that

this part of suevite of the FBN73 drill core records a sedimentation process out of a low velocity, density-stratified system, where particles can be sorted by their size and density (Kaminski and Jaupart 1998). Additionally to this fact, accretionary lapilli were observed on top of each sedimentary unit (296 and 309 m). These lapilli can be described as an inner ash aggregate, with no internal structure surrounded by a layer of very fine ash. Similar lapillis could also be observed in the Deiningen drill core, also located in the inner crater, 3 km from the crater center to SE (Graup 1981). An ash aggregate is formed by agglomeration of ash inside a rising plume. During the dropping down of the aggregates to lower levels of the plume, the aggregates grow and accrete finer ash material, forming accretionary lapilli. Due to the fact that the accretionary lapilli of the FBN73 core show just one layer of accreted fine ash material and lacks further concentric laminations, the conclusion is that the lapilli fell out directly from an upward rising plume (Brown et al. 2010). Therefore, it seems plausible that the upper part of the FBN73 suevite (296 - 330 m) results from deposition out of an ejecta plume, according to Stöffler (1977) and Jankowski (1977b).

However, according to Artemieva et al. (in preperation), a simple settling through atmosphere would result in a well-mixed deposition. All particles in all grain sizes would be equally present through the whole depth, with a deficiency of the largest particles at the very top (Fig.5.9a). In contrast, settling out of 50 m thick water layer would give well-graded deposits, with the largest particles at the bottom in mixture with smaller particles and the smallest particles at the top (Fig. 5.9b). In comparison to the observation data of FBN73, it is obvious that in the upper sedimentary unit (296 - 314m) and the graded suevite (314 - 330) that the larger particles can be found at the bottom in each unit, overlain by the finer fraction (Fig. 5.9c). Thus, it is possible to conclude that the upper sedimentary unit and the graded suevite result from two different sedimentation regimes, with a hiatus in between. Furthermore, the two units must have been reworked by water, after their sedimentation out of the ejecta plume.

5.6. Conclusion

As demonstrated in this Chapter, the suevite was transported in different processes and including later sedimentation:

1. Particles of the suevite from the lower Wörnitzostheim and Otting were transported in a more dilute, less density stratified, turbulent suspension, travelling at high velocities and forming a wide-spread deposition similar to a pyroclastic surge deposit.

2. Particles from the Enkingen and upper Wörnitzostheim suevite were transported in a density stratified current, where grain-grain interactions occur, travelling at lower velocities, similar to a pyroclastic flow deposit.

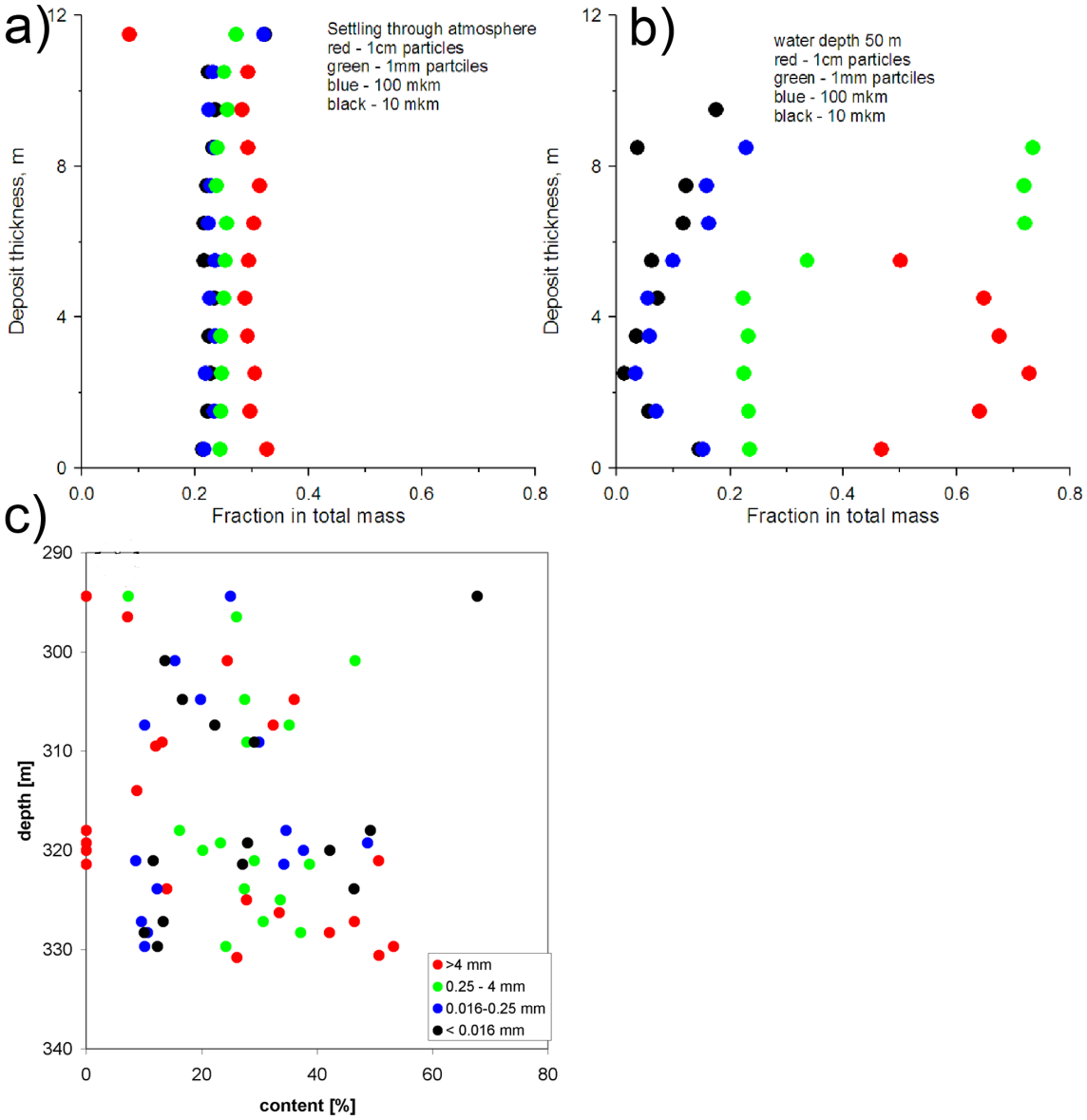

Fig. 5.9.: Content of particle fractions of different grain sizes. a, b) Results of numerical modeling from sedimentation through atmosphere (a) and through 50 m water layer (b) (Artemieva et al. in preperation). c) Measured content of particle fractions of upper sedimentary unit (296 - 314 m) and graded suevite (314 - 330 m) of FBN73.

3. Particles of the upper part of the FBN73 suevite (296 - 330 m) result from deposition out of an ejecta plume and must have been reworked by water, after their sedimentation.

However, the process that leads to the formation of the pyroclastic flow-like and surge-like transport system remains unknown. Only the presence of volatiles can initiate such a mass flux (Artemieva et al. 2009). Was the water bounded in the sediments, overlying the crystalline basement, enough to trigger a “pyroclastic” flow? Or, as proposed by Artemieva et al. (2009), the result of a later water entry into the crater and a second explosion of the impact melt pool, similar to a phreatomagmatic explosion that initiated the “pyroclastic” flow? This Chapter shows that at least surface water played an important role in the crater formation process.

The question of the role of water in the suevite formation process can only be solved by detailed geochemical and microscopic analyses of the melt particles of the inner crater suevite and its matrix compared to the melt particles of the suevite beside the inner ring of the Ries crater. Only then, together with numerical models, can the crater mechanics be reconstructed completely.

6. Chemical analysis of the suevite matrix and melt particles and calculation of the melt content of the suevite

6.1. Abstract

Today, the hydrothermal alteration of the suevite matrix is widely accepted. However, which primary material was transformed into the clayey matrix is still a matter of discussion. This Chapter compares the chemical composition of the melt particles of suevites at four different drill cores inside and outside the crater, with their corresponding matrix, to identify the original composition of the suevite matrix. Finally, the primary melt content of the Ries suevite is estimated. The results show that the suevite can be distinguished into the following subunits: 1) Strongly altered suevite, with similar melt and matrix composition, 2) Inhomogeneous suevite, with differentiation into K-poor and K-rich melt, with either silicate matrix similar in chemistry to the melt or non-existent silicate matrix, 3) Chemical homogeneous suevite, with similar melt and matrix composition, which can be considered as original impact melt, and 4) Chemical homogeneous suevite, with different melt and matrix composition. The volume of the impact melt of the Ries crater can be estimated to ~ 4 km^3, which is still less compared to impact craters similar in size to the Ries crater.

Thin sections were prepared by R. Knöfler (MfN). K. Born and P. Czaja (MfN) assisted with the electron microprobe (EMPA) and scanning electron microscopy (SEM) measurements. All scanning electron microscopy imaging and mapping, optical microscopy, processing of the data, text, and interpretation were performed by the author. Methods and results were discussed with Michel Jébrak. Richard Grieve helped with English correction.

All modal analyses of suevite matrix < 0.25 mm for all drill cores are summarized in Appendix 4. All ternary diagrams and points of EMPA measurements are summarized in Appendix 5. All isocone diagrams for average analyses of melt particles and suevite matrices are summarized in Appendix 6.

6.2. Introduction

Although suevite deposits have been studied extensively (e.g., Hörz 1965; Förstner 1967; Stöffler et al. 1977; von Engelhardt et al. 1995; Wittmann et al. 2004; Stöffler et al. 2004), there is no consensus on their formation, transportation, and deposition. In particular, the composition and formation of the suevite matrix have been a matter of discussions over decades. As mentioned above, suevite is defined as a breccia with a particulate matrix (Stöffler and Grieve 2007). At the Ries, this matrix is composed on average of 80 - 90% montmorillonite, minor quartz, feldspar, biotite, carbonate and, in some places, zeolites (Engelhardt and Graup 1984, Engelhardt et al. 1995). In contrast, it has been also proposed that the suevite represents a series of impact-generated melts that were molten at the time of and after deposition. Liquid immiscibilities were identified and the montmorillonite in the matrix is interpreted as the original impact glass, which would explain the lack of impact melt in the crater (Osinski et al. 2004).

Today, the hydrothermal formation of the suevite matrix is widely accepted (Allen 1982, Engelhardt and Graup 1984, Newsom et al. 1986, Osinski 2005). The mean temperature of suevite at the time of deposition was in the order of 580°C to 750°C (Pohl et al. 1977, Engelhardt et al. 1995). Upon cooling, the heat was quickly removed by convection and as soon as the temperature dropped below the boiling point of water, slower conductive heat transfer occurred. The main late stage of hydrothermal alteration at less than 100°C to 130°C was associated with the formation of the observed low-temperature Fe-rich montmorillonite (Newsom et al. 1990). Which material was transformed into the montmorillonite is still a matter of discussion. On one hand, the montmorillonite can be derived from the average glass composition by removing alkali silicate and some Ca, and by adding Fe and Mg by the action of neutral or weakly alkaline solutions. On the other hand, due to the fact that most of the coarse components of the suevite derive from crystalline basement, it also seems to be likely that the same holds true for the matrix. Therefore, possible source materials for the montmorillonite in the suevite matrix are finely comminuted gneiss, small glass particles, or condensates from vaporized crystalline rocks (Engelhardt and Graup 1984). However, the question which primary material was transformed into the clay mineral remains unclear.

At the Ries crater, there is one obvious fact: The total volume of observed impact melt is two orders of magnitude smaller compared to the amounts deduced from crater scaling laws and observed art other craters of similar size (Cintala and Grieve 1994, Grieve 1975). Impact melt occurs in two main forms within the Ries crater: a few isolated bodies of minor volume of coherent impact melt rocks, tens of meters in size, and, as up to decimeter-sized, melt particles within the groundmass of the suevite (e.g., Hüttner and Schmidt-Kaler 1999). Estimates of the total melt volume in the Ries crater range from 0.1 - 0.2 km^3 (Stöffler and Ostertag 1983) to about 1.5 km^3 (Engelhardt and Graup 1984). Based on crater scaling laws a

total melt volume of 15 km^3 would be expected for the Ries impact (Cintala and Grieve 1994), which is in the range of the total volume of the Ries suevite (Stöffler et al. 1977). Hence, one of the main questions of the Ries crater is: what happened to the "missing" impact melt during crater modification.

This Chapter compares the chemical composition of the melt particles of suevites at four different sites inside and outside the Ries crater with that of the corresponding matrix. The gains and losses, compared to the melt, necessary to produce the altered matrix are studied to determine to original suevite matrix. Finally, the primary melt content of the Ries suevite is estimated. Samples for this work have been obtained from the four drill cores drilled through the suevite inside and outside of the Ries crater, which were also used for stereometric analysis (Chapter 5) (Fig. 3.1).

6.3. Analytical methods

The suevite matrix and melt particles were examined petrographically using a LEITZ DM RXP polarization microscope. A total of 29 thin sections of samples from drill core FBN73, 6 thin sections of samples from Enkingen, 18 thin sections of samples from Wörnitzostheim, and 15 thin sections of samples from Otting, covering all suevite sub-units, were inspected. SEM (scanning electron microscopy) analysis was carried out on a JEOL JSM-6300 instrument equipped with a tungsten cathode and a Bruker AXS EDX detector at the Museum of Natural History Berlin, operating at 15kV and a beam current between 1 and 10 nA. Element mapping was performed with Bruker QUANTAX software, at a working distance of 39 - 42 mm. Backscattered electron (BSE) imagery was used to investigate the micro-texture of the matrices. The settings for generating BSE images were the same as mentioned above, except for a reduced working distance of 8 mm.

The modal mineral composition of the finer fraction ($<$ 0.25 mm) of the suevite was determined by image analysis. Element mappings for 10 FBN73, 6 for Enkingen, 5 for Wörnitzostheim, and 2 for Otting samples were done. The mapped elemental distribution for Al, Si, Na, K, Ca, Mg, Fe, Ti, and P were superimposed using standard image software. Minerals detected on the corresponding secondary electron (SE) image were outlined and colored, depending on their chemical composition. From the chemical composition of the minerals and their morphology, the mineral type was deduced (Appendix 4).

Fifteen thin sections of FBN73, 6 thin sections of Enkingen, 6 thin sections of Wörnitzostheim, and 2 thin sections of Otting samples were investigated at the Museum of Natural History Berlin with a JEOL JXA-8800 electron microprobe (EMPA) operating at 20 kV, 20 nA, counting times of 30 s, and a beam diameter of 3 μm. Energy-dispersive (EDX) and wavelength-dispersive spectrometry (WDX) were used to determine the chemical compositions of matrices and melt particles. Analyses were calibrated using Smithsonian and Astimex

international mineral standards. The calibrated elements and respective average detection limits [in ppm] are: Si [360], Na [100], Cr [40], Cl [10], Ti [70], Al [170], Mg [100], Fe [270], K [20], Mn [30], P [20], and Ca [70].

6.4. Results

6.4.1. Composition of the finer fraction of the Ries suevite

The finer fraction of the Ries suevite comprises mineral fragments distributed in the fine clay mineral matrix. The images of the modal analyses of all drill cores can be seen in Appendix 4. All results of the modal analyses are summarized in Table 6.1.

Quartz and feldspars are the main components of all suevite units. Whereas, in the FBN73 suevite particles of calcite can be detected as one of the main compounds in the groundmass, in the Enkingen and Wörnitzostheim suevites calcite frequently can be observed as homogenous matrix fillings. Commonly, phyllosilicates and mafic silicates also occur as major phases, seldom as minor phases. Sulfide (pyrite), phosphate (apatite), and ilmenite can be usually detected as minor components in the groundmass.

6.4.2. Chemical composition of melt particles and of the suevite matrix

The chemical composition of the suevite matrix, which comprises the clay mineral filling (phyllosilicates, felsic and mafic minerals) of the suevite, was determined. Melt particles were detected by optical microscopy and the chemical composition of their interior, as well as the melt rims, was determined. The A-CN-K diagrams (e.g., Fig. 6.1a, points of EMPA measurements are given in Fig. 6.2) give the "chemical index of alteration" (CIA). Ca, Na, and K can be lost during the alteration process until the formation of kaolinite or chlorite, with an in-between stage of smectites. This means that the stronger the alteration process is the closer the data points plot to the Al apex of the diagram (Nesbitt and Young 1984). In the FM-CN-K diagrams (e.g., Fig. 6.1b), most analyzed phases and target rocks have distinguishable locations on the diagram. This separation among phases makes this diagram useful for visualizing mixing relationships and for tracking alteration pathways. The mean values of the electron microprobe analyses of each plotted melt particles and suevite matrices are given in Table 6.2. All ternary diagrams of the average chemical composition of melt particles and matrix and points of EMPA measurements of all drill cores are given in Appendix 5.

The composition of the melt particles is very inhomogeneous. Whereas in the Otting suevite and the melt low suevite of Wörnitzostheim, the composition of the melt particles corresponds

to a chemical mixture of all target rocks, as described by Stähle (1972), with decreasing distance from the crater center (from Wörnitzostheim to FBN73) the melt composition becomes more and more differentiated into a K-rich and a K-poor melt, and the Fe, Mg concentrations decrease. In the lower part of FBN73 (below 380 m), almost no K could be detected in the melt particles. Additionally, these melts show the lowest Fe, Mg concentration of all melt particles. K rich melts are restricted to melt veins in partially melted rock clasts (melt 2 of Fig. 6.3), to inclusion rich melt particles (melt 2 of Fig. 6.4) or to highly altered melt particles or melt rims (melt 2 of Fig. 6.5).

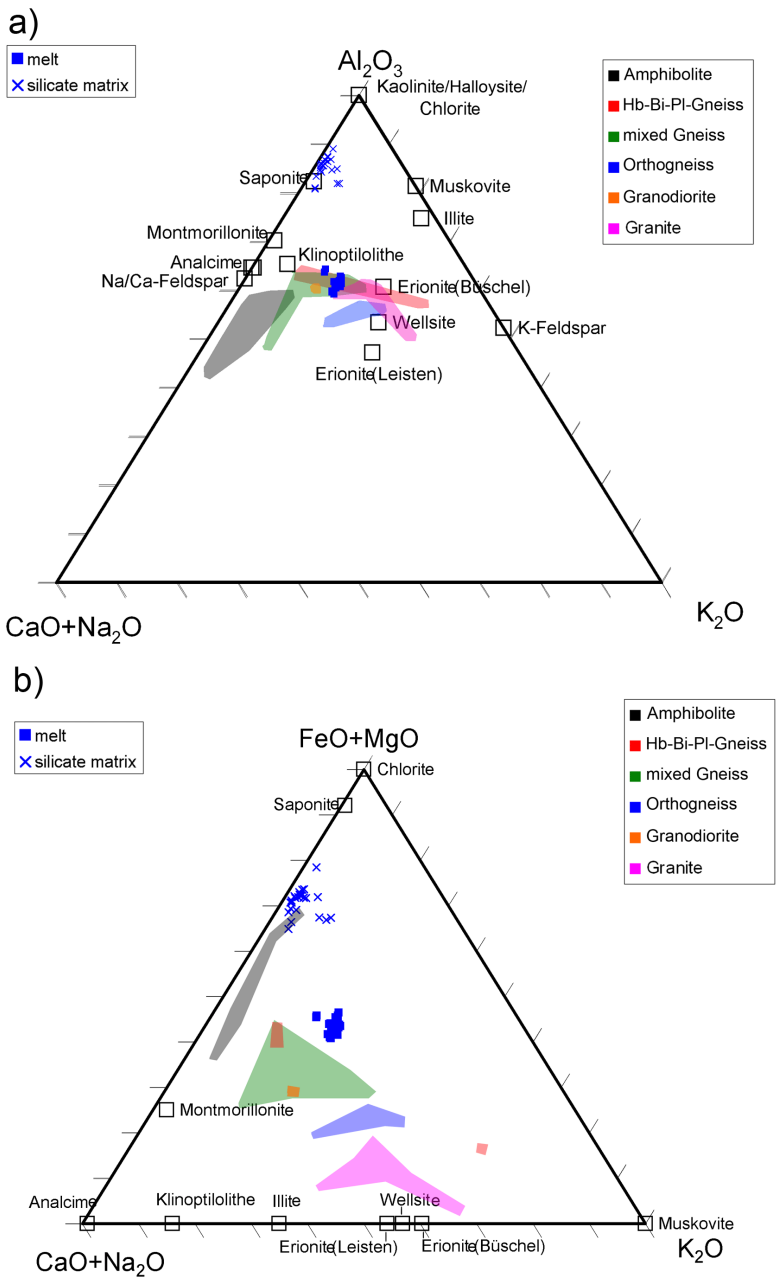

Fig. 6.1.: a) Ternary diagrams of Otting; data plotted in weight percent: a)Al_2O_3 (A) – $CaO+Na_2O$ (CN) –K_2O (K) diagram; b) FeO+MgO (FM) – $CaO+Na_2O$ (CN) –K_2O (K) diagram. Chemical compositions of target rocks are from Graup (1977), chemical compositions of clay minerals and zeolites are from Osinski (2005), Stähle (1972), Stähle and Ottemann (1977). All ternary diagrams of the average chemical composition of melt particles and matrix and points of EMPA measurements of all drill cores are given in Appendix 5.

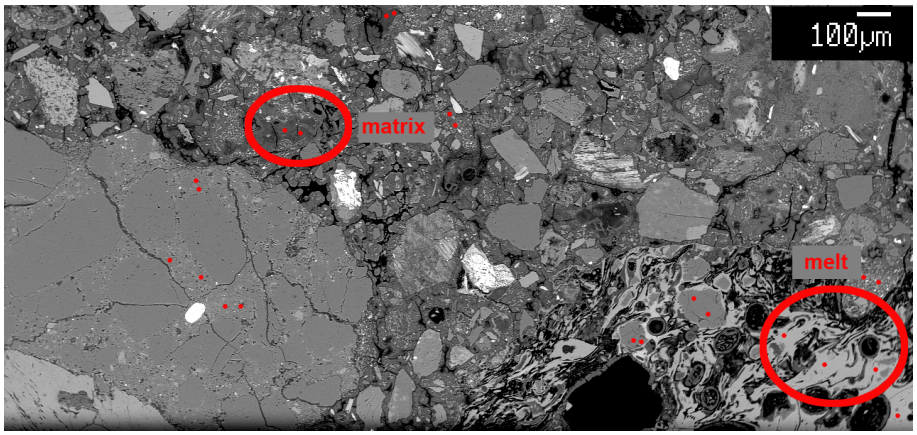

Fig. 6.2.: Points of EMPA measurements of melt particles and suevite matrix drawn in BSE (backscattered electron) images of Otting sample from 1.8 m depth.

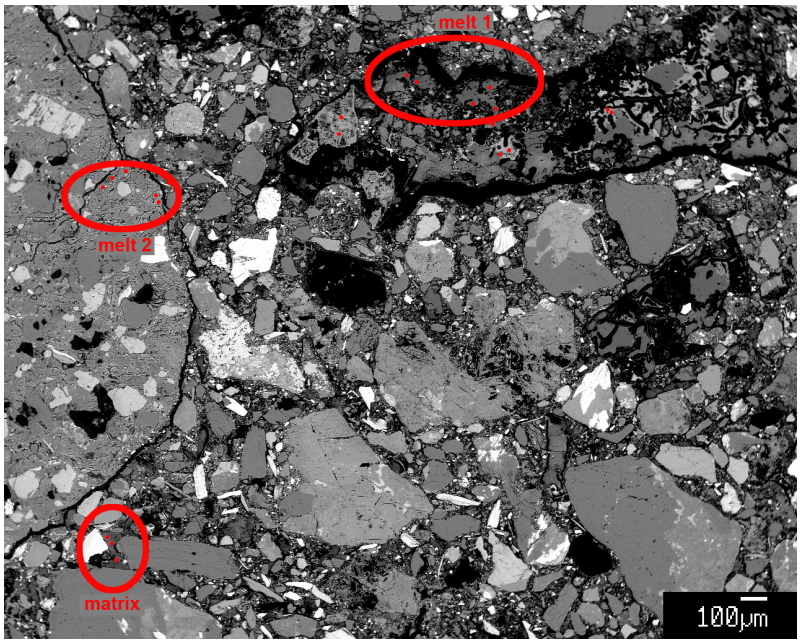

Fig. 6.3.: Points of EMPA measurements of melt particles and suevite matrix drawn in BSE images of FBN73 sample from 309.1 m depth.

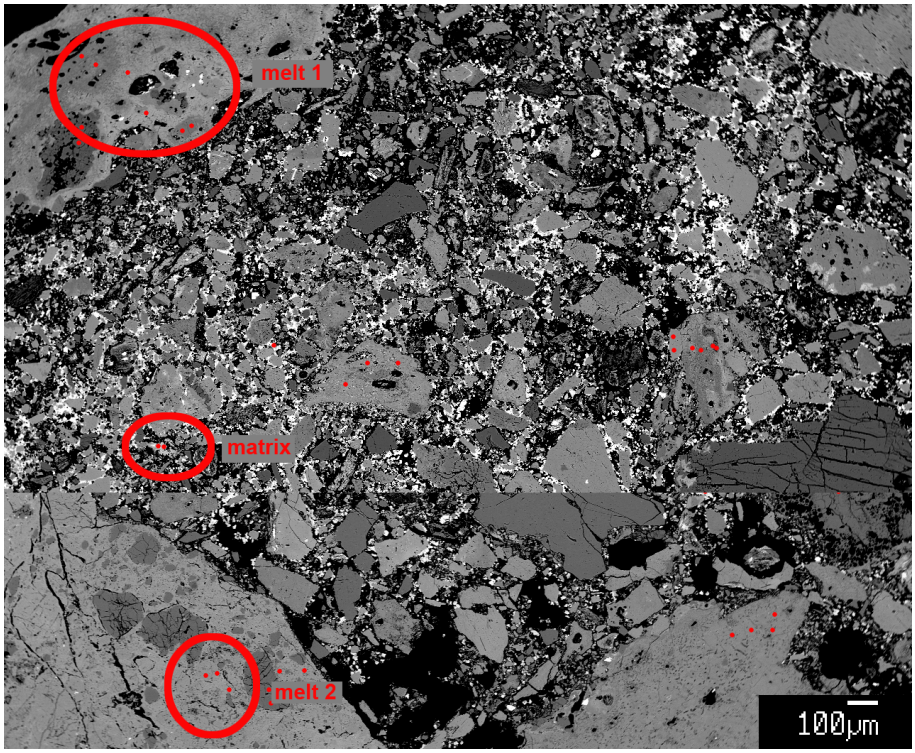

Fig. 6.4.: Points of EMPA measurements of melt particles and suevite matrix drawn in BSE images of Wörnitzostheim sample from 36.9 m depth. Sulfide impregnation can be seen as bright points.

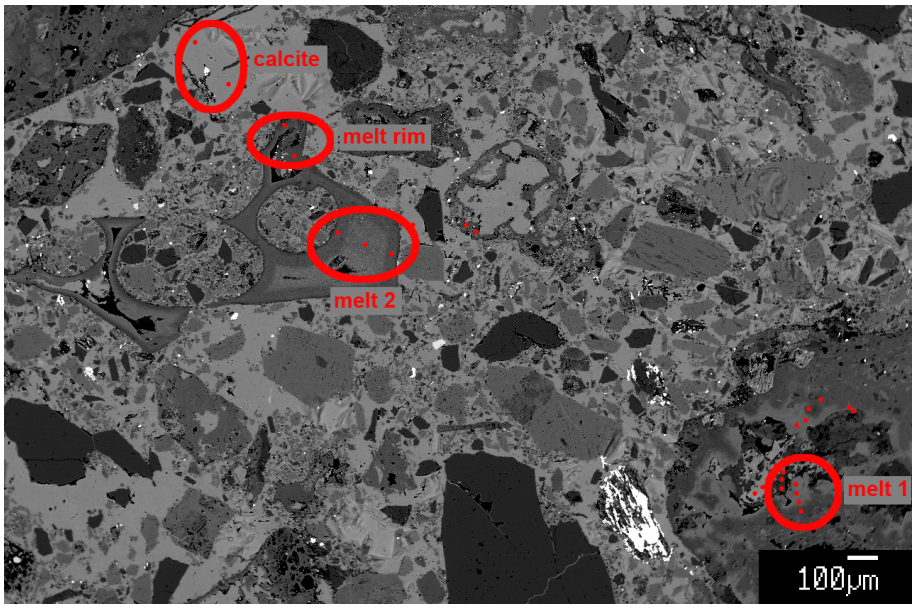

Fig. 6.5.: Points of EMPA measurements of melt particles and suevite matrix drawn in BSE images of Enkingen sample from 33.8 m depth.

6.4.3. Comparison of melt und suevite matrix

In studying the alteration of the suevite matrix, an immediate question concerns the nature of the original suevite matrix and the gains and losses of material necessary to produce the altered matrix. The chemical data of the melt particles were plotted against the chemical data of the suevite matrix, recrystallized melt, or filled melt cracks, rims, and bubbles. Under the assumption that the melt has the same origin as the matrix, the immobile components would generate a straight line through the origin, which is the fundamental ratio of equivalent masses before and after alteration. This line is called an "isocon" (Gary et al. 1974). The relative gains and losses of the mobile components are given by the displacement of these data points from the reference isocon (e.g., Fig. 6.6). The slope of the best-fit isocon is (M_{melt}/M_{matrix}), which equates to a mass increase from melt to matrix of (M_{matrix}/M_{melt}). The isocon diagrams of all drill cores can be seen in Appendix 6. All results of the isocon diagrams are summarized in Table 6.3.

A general characteristic, which can be observed in all drill cores, is the enrichment of Al, Fe and Mg and the depletion of the alkaline elements (Na, K) in the silicate matrices, compared to the melt particles. An exception to this can be observed in the FBN73 suevite below 380 m, in some parts of the lower suevite unit of Enkingen, and in the lower parts of the melt-rich suevite of Wörnitzostheim, where the composition of the silicate matrix is almost identical to the composition of the melt particles.

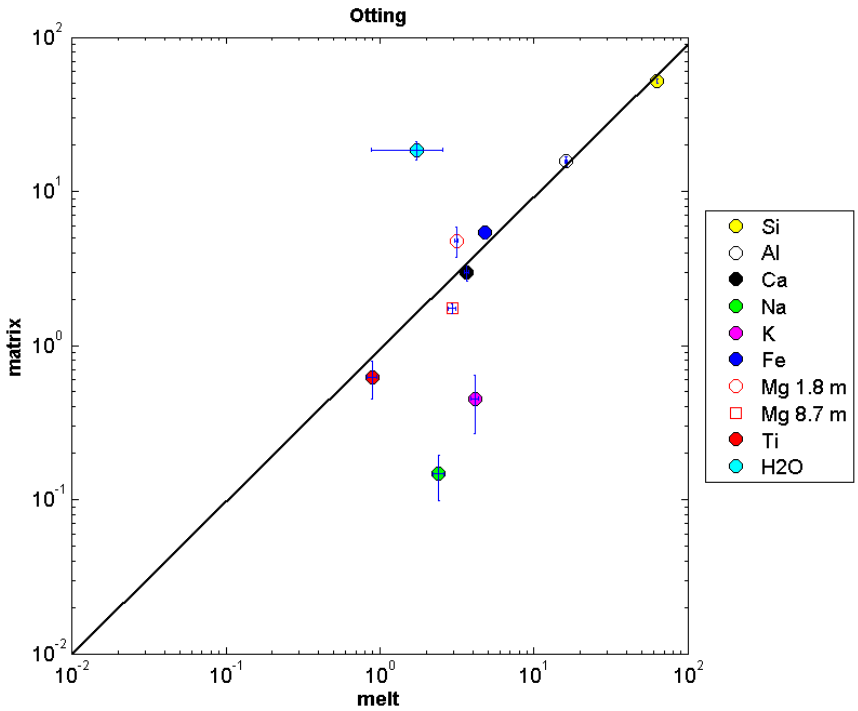

Fig. 6.6.: Isocon diagram for average analyses of melt particles and suevite matrices of Otting drill core. Oxides are plotted in weight%. Isocon is shown according to hypotheses of constant alumina and silica. The isocon diagrams of all drill cores can be seen in Appendix 6.

Table 6.1.: Summarized results of modal composition of the suevite matrix <0.25 mm.

	Major minerals	Minor minerals	Matrix	Matrix characteristics compared to melt
		FBN73		
Sedimentary unit	quartz, feldspars, phyllosilicates, calcite	sulfides, phosphates	siliceous	- enriched in Fe, Mg, depleted in Na, Si
Graded suevite	quartz, feldspars, phyllosilicates, calcite	sulfides, phosphates, dolomite, zeolites, ilmenite	calcitic to siliceous	
Melt rich suevite (331-378 m)	quartz, feldspars, ,mafic silicates	calcite, sulfides, phosphates	siliceous	- enriched in K, depleted in Na, Si - melt rims and interior bubbles are surrounded by Fe, Mg rich clay minerals
Sorted suevite	quartz, feldspars, phyllosilicates, mafic silicates, calcite	pyrite	siliceous	- enriched in Fe, Mg, depleted in Al, Si, Na
Melt rich suevite (380-520 m)	quartz, feldspars, calcite, phyllosilicates	dolomite, pyrite	siliceous	at 380 m: - enriched in K, Mg, Fe, depleted in Na, Si at lower units: - matrix comparable to melt
Melt poor suevite	quartz, feldspars, phyllosilicates, mafic silicates	ilmenite, phosphates	siliceous	- matrix almost identical to melt
		Enkingen		
Reworked suevite	quartz, kalifeldspars, mafic silicates	pyrite, phosphates	calcitic, siliceous	
Middle suevite	quartz, kalifeldspars, phosphates		calcitic	- melt particles are enriched in Na at the rim and enriched in Mg in the strongly altered interior part
Intersected suevite	quartz, feldspars, phyllosilicates	mafic silicates, pyrite, ilmenite, phosphates	calcitic, siliceous, no matrix	- matrix almost identical to melt
		Wörnitzostheim		
Reworked suevite	quartz, feldspars	zeolites	calcitic, siliceous	- calcitic matrix contains fibers of dolomite - silicate matrix almost identical to melt
Melt rich suevite	quartz, feldspars	mafic silicates, pyrite	calcitic, siliceous	3 types of melt (enrichments compared to matrix): - melt enriched in Na, Si - melt enriched in Na, Ca, Mg - melt enriched in K
Melt poor suevite	quartz, feldspars, phyllosilicates, mafic silicates	phosphates	siliceous	- enriched in Fe, Mg, depleted in Na, K, Ca - with large inclusions of calcite
		Otting		
	quartz, feldspars	ilmenite, phosphates	siliceous	- enriched in Al, depleted in Na, K - melt rims and interior bubbles are surrounded by Fe, Mg rich clay minerals - Mg, Ca highly variable

Table 6.2.: Mean values of electron microprobe analyses of different kinds of melt particles and suevite matrices [weight%]. Volatile content is determined as remaining weight% to 100%.

FBN73	SiO2	Na2O	TiO2	Al2O3	MgO	FeO	K2O	CaO	volatiles
Sedimentary unit									
304.8 m Na rich melt	64.62	12.36	0.03	17.82	0.54	0.61	0.70	0.28	3.05
304.8 m Fe, Mg rich melt	54.49	3.20	0.47	16.47	5.34	8.52	1.30	1.84	8.28
304.8 m Al rich melt	62.84	5.27	0.03	22.57	0.12	0.31	1.77	3.30	3.85
304.8 m Recrystallized melt	61.82	7.31	0.31	23.73	0.45	1.07	2.05	3.80	0.16
309.1 m melt 1	61.14	4.85	0.02	14.80	0.37	0.17	0.59	0.65	17.37
309.1 m melt 2	53.75	0.99	0.85	16.53	3.05	3.73	5.08	0.29	15.63
Silicate matrix	52.46	3.18	0.35	14.87	2.73	4.00	2.04	0.47	19.80
Graded suevit									
Melt	63.49	5.35	0.01	17.63	0.31	0.06	1.25	0.68	11.20
Silicate matrix 1	64.06	6.08	0.17	21.68	0.83	1.02	1.40	1.81	2.97
Silicate matrix 2	48.62	1.06	0.61	13.63	2.80	3.13	2.30	2.43	25.21
Recrystallized melt	60.98	3.86	0.02	16.53	0.36	0.07	2.75	0.81	14.61
Altered melt	62.90	1.31	0.08	8.74	0.91	1.14	1.14	0.61	23.12
Melt rim	50.13	1.45	0.03	11.95	6.17	1.12	1.56	1.44	17.10
Melt rich suevite (331-378 m)									
Melt 1	60.39	8.15	0.01	19.79	0.20	0.39	0.04	0.03	10.99
Melt 2	56.24	3.65	0.25	18.80	0.93	2.70	4.85	4.28	8.07
Melt rim	28.55	1.19	0.16	5.68	7.51	11.10	0.25	0.88	44.39
Silicate matrix	60.73	4.01	0.03	18.10	0.48	0.79	1.09	0.31	14.41
Sorted suevite (378.5 m)									
Melt 2	64.10	3.96	0.38	19.73	0.43	0.46	2.77	3.51	4.62
Schliere	53.07	1.24	1.02	14.41	5.35	7.58	1.74	1.29	14.11
Recrystallized melt	63.81	2.84	0.01	15.48	0.61	0.12	1.40	1.10	14.62
Silicate matrix	52.86	1.60	0.67	13.97	3.13	4.65	1.96	1.59	19.44
Melt rich, melt poor suevite (380 – 600 m)									
Melt	58.00	8.04	0.01	22.45	0.03	0.12	0.02	0.02	11.28
Silicate matrix	58.41	6.73	0.03	20.93	0.27	0.41	0.12	0.31	12.77
Melt cracks and bubbles	31.89	1.24	1.10	11.59	13.88	21.18	0.08	0.40	18.04
Dike suevite									
Melt	29.96	0.35	0.22	17.66	16.77	20.77	0.49	0.39	13.03
Silicate matrix	58.01	9.81	0.02	21.95	0.08	0.17	0.02	0.09	9.82

Enkingen	SiO2	Na2O	TiO2	Al2O3	MgO	FeO	K2O	CaO	volatiles
25.7 m silicate matrix	54.14	1.09	0.15	16.71	2.72	3.92	0.48	0.30	20.41
33.8 m melt rim	51.28	0.53	0.27	12.27	3.12	8.97	0.28	1.75	21.42
78.8 m silicate matrix	48.59	0.76	0.37	4.86	1.39	3.49	0.17	1.04	39.15
Melt 1	60.66	5.91	0.71	18.73	0.53	1.49	1.06	4.64	5.93
Melt 2	60.17	2.13	0.47	17.99	1.14	1.96	6.98	1.35	7.57

Wörnitzostheim	SiO2	Na2O	TiO2	Al2O3	MgO	FeO	K2O	CaO	volatiles
19.1 m melt 1	48.26	0.98	0.66	16.40	5.04	6.33	2.67	2.91	16.45
19.1 m silicate matrix	52.79	0.32	0.48	15.63	2.28	4.55	0.67	1.64	21.49
25 – 80 m melt 1	59.70	4.79	0.45	21.30	1.18	2.60	2.40	3.07	4.51
27.1 m melt 2	50.63	1.40	0.03	32.02	1.93	4.72	10.47	0.09	0.00
27.1 m silicate matrix	50.65	0.31	0.19	13.83	2.39	6.49	0.94	1.62	23.49
36.9 m melt	62.89	2.37	0.02	20.68	0.45	0.77	12.55	0.23	0.08
36.9 m silicate matrix	45.90	2.95	4.79	18.70	6.01	9.98	4.90	3.68	2.97
80 – 100 m melt	65.14	2.20	0.68	15.87	2.37	4.20	3.83	3.34	2.10
80 – 100 m silicate matrix	55.76	0.83	0.28	15.88	3.45	5.42	0.27	0.60	7.67

Otting	SiO2	Na2O	TiO2	Al2O3	MgO	FeO	K2O	CaO	volatiles
Melt	62.78	2.40	0.89	16.11	4.81	4.12	3.65	1.72	1.72
Silicate matrix	52.05	0.15	0.62	15.62	5.39	0.45	2.99	18.62	18.62

Table 6.3.: Summarized results of gains and losses of the suevite matrix compared to the melt particles from best-fit-isocons.

	Best-fit isocon			Gains	Losses
	Elements	**Slope**	**Mass increase**		
			FBN73		
Sedimentary unit - matrix	Si, Al, $Na_{Fe\text{-}melt\text{-}304.8m}$, $Ti_{Fe\text{-}melt\text{-}304.8m}$, $Fe_{melt2\text{-}309.1m}$, $Ca_{melt1\text{-}309.1m}$	0.87	14.9%	H(w-s), Fe(s), $Na_{melt2\text{-}309.1m}$(s), Mg(s), K(w-s), $Ca_{Na\text{-}melt\text{-}304.8m}$(w), $Ca_{melt2.309.1m}$(w)	$Fe_{Fe\text{-}melt\text{-}304.8m}$(w), Na(w-s), $Mg_{Fe\text{-}melt\text{-}304.8m}$(w), $K_{melt2\text{-}309.1m}$(s), $Ca_{Fe,Al\text{-}melt\text{-}304.8m}$(s)
Sedimentary unit – recrystallized melt	Si, Al, $Ca_{Al\text{-}melt\text{-}304.8m}$, $K_{Al\text{-}melt\text{-}304.8m}$, $Mg_{Na\text{-}melt\text{-}304.8m}$, $Mg_{melt1\text{-}309.1m}$	1.06	-5.7%	Na(w-s), Ca(w-s), K(w-s), $Fe_{Na,Al\text{-}melt\text{-}304.8m}$(w-s), $Fe_{melt1\text{-}309.1m}$(s), $K_{Al\text{-}melt\text{-}304.8m}$(w), $Ti_{Na,Al\text{-}melt304.8m}$(s), $Ti_{melt1\text{-}309.1m}$(s)	H(s), $Na_{Na\text{-}melt\text{-}304.8m}$(w), $K_{melt2\text{-}309.1m}$(s), $Fe_{Fe\text{-}melt\text{-}304.8m}$(s), $Fe_{melt2\text{-}309.1m}$(s), $K_{Fe\text{-}melt\text{-}304.8m}$(s)
Graded suevite	Si, Al, $Na_{matrix1}$, $K_{matrix1,altered\ melt,melt\ rim}$, $Ca_{altered\ melt}$	0.88	13.6%	Fe(s), K(w-s), Ca(w), $K_{matrix2}$(w), $H_{matrix2,altered\ melt,melt\ rim}$(w), Ti(w)	$H_{matrix1}$(s), Na(s)
Melt rich suevite – matrix	Matrix: Si, Al, Na Cracks: Si, Al, Na	1.03 0.83	-3% 20%	H(w), melt1: Fe(s), K(s), Mg(s), Ca(s) Fe(s), Mg(s), K(w), Ca(w)	melt2: Fe(s), K(s), Mg(w), Ca(s), Ti(w) H(w)
Sorted suevite - matrix	Schliere: Si, Al, K, Na, Ca, Ti Melt: Si, Al, K_{melt2}	0.99 0.83	1% 20.5%	H(w), Fe(s), Mg_{melt2}(s), Ti(w-s), melt1: Fe(s), Ca(s), K(s)	Fe(w), Mg(w) Na(w-s), Ca_{melt2}(w)
Sorted suevite - recrystallized melt	Schliere: Si, Al, H, K, Ca Melt: Si, Al, Na_{melt2}	1.18 0.99	-15.3% 1%	Na(w) H(w), Mg_{melt2}(w), melt1: K(s), Fe(s), Ca(s)	Mg(s), Fe(s), Ti(s) Na_{melt1}(s), melt2: K(w), Ca(w), Fe(w), Ti(s)
Melt poor suevite	Matrix: Si, Al, H, Na, Ti Cracks: Si, Al, K	0.99 0.55	1% 82%	Ca(w), Fe(w), Mg(w), K(w) H(w), Fe(s), Mg(s), Ca(w), Ti(s)	Na(s)
Dyke suevite	Al	1.24	-19.4%	Si(w), Na(s)	H(w), Fe(s), Mg(s), Ca(w), K(s), Ti(w)
			Enkingen		
Reworked suevite	melt2: Si, Al, H, Fe, Mg, Na, K, Ti	0.99	1%	melt 1: Fe(s), Mg(s), H(w)	melt 1: Na(s), Ca(s), K(w), melt 2: Ca(w)
Middle suevite	Al, Si	0.8	25%	Fe(s), Mg(s), H(s), Ti_{melt2}(s), Ca_{melt2}(w)	Na(w-s), K(w-s), Ca_{melt1}(w)
Intersected suevite	Ti, Ca_{melt2}, Al Ti, Si	0.27 0.78	270% 28%	Si(s), Mg(s), Fe(s), H(s) Mg(w), Fe(w), H(s)	K(w-s), Na(w), Ca_{melt1}(w) Al(s), K(s), Na(w), Ca(w)
			Wörnitzostheim		
Reworked suevite	Ti, Al, Si	1.08	-7.4%	H(s)	Ca(w), Na(w), K(w), Fe(w), Mg(w)
Melt rich suevite	Al, Si	0.8	25%	Fe(s), Mg(s), H(s), Ca_{melt2}(s), $Na_{melt2\text{-}36.9m}$(w), $K_{melt2\text{-}27.1m}$(w), $K_{melt1\text{-}36.9m}$(s), $Ti_{36.9m}$(s)	Ca_{melt1}(w), $Na_{27.1m}$(s), $Na_{melt1\text{-}36.9m}$(w), $K_{melt1\text{-}27.1m}$(w), $K_{melt2\text{-}36.9m}$(s)
Melt poor suevite	Al, Si	0.86	16.3%	Mg(w), Fe(w), H(s)	Ca(s), K(s), Ti(w), Na(w)
			Otting		
	Ti, Ca, Fe, Al, Si	0.84	19%	$Mg_{1.8m}$(w), H(s)	Na(s), K(s), $Mg_{8.7m}$(w)

6.4.4. Estimation of the melt content of the suevite before alteration process

As mentioned in the introduction, the total volume of observed impact melt of the Ries crater is abnormally low compared to crater-scaling laws and other craters of similar size (Cintala and Grieve 1994, Grieve 1975). One problem of the former estimations of the melt volume calculation results from the neglection of the melt particles with grain sizes < 0.25 mm. The volume of melt, which is altered to clay minerals, is uncertain.

In Chapter 5, the grain-size distribution and fractal dimension of the melt particles of all drill cores was measured from 0.016 to 63 mm. It could be frequently observed that the fractal dimension of the particles at the SEM scale (0.016 - 0.25 mm) is lower than that of the thin section scale (0.25 - 4 mm). It seems likely that the grain sizes at both scales had been distributed similarly before alteration occurred. If we assume that the lack of the finer-grained particles results from the alteration process, as proposed by Engelhardt and Graup (1984), we are able to correct the melt content of the SEM scale by using the fractal dimension of the thin section scale as explained here after:

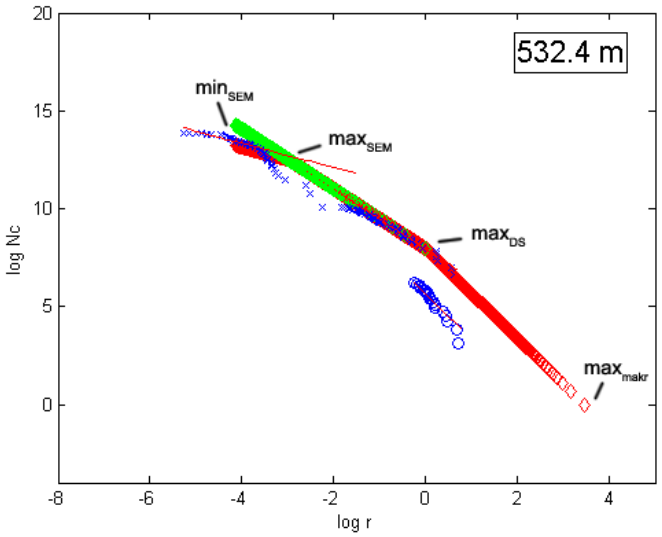

Fig. 6.7.: Cumulative frequency diagram of grain size distribution of suevite of FBN73 at 532.4 m depth for melt particles: blue: measured data, red: recalculated data using measured fractal dimension, green: recalculated data with using fractal dimension of thin section scale ($0.25 < r < 1$ mm) for SEM scale ($0.016 < r < 0.25$ mm). $\max_{makr}$, $\max_{DS}$, $\max_{SEM}$, $\min_{SEM}$ represent maximum grain size, transition point between macroscopic and thin section scale, transition point between thin section and SEM scale, minimum grain size = 0.016 mm, r functions as grain size parameter, N_c = number of particles whose sizes are greater than r.

The grain sizes of the transition from lower to higher (or vice versa) fractal dimension, represented by a knee in the curve, were determined from cumulative frequency diagrams (Fig. 6.7). The maximum detected grain size was set to $\max_{makr}$, the transition points to $\max_{DS}$ (as transition between macroscopic grain sizes and grain sizes in DS scale) and to $\max_{SEM}$ (as transition between grain sizes at the thin section scale and SEM scale), and the minimum grain size was set to $\min_{SEM} = 0.016$ mm. N_c = number of particles with sizes larger than r, of each transition point can be found by simple linear calculation, r functions as the grain size parameter, and D

is the fractal dimension (subscriptions $_makr$, $_DS$, $_SEM$ symbolize macroscopic, thin section, and SEM scale):

$$\ln N_{c-makr} = -D_{makr} \cdot \ln \max_{DS} + D_{makr} \cdot \ln \max_{makr} \tag{6.1a}$$

$$N_{c-makr} = e^{\ln N_{c-makr}} \tag{6.1b}$$

$$\ln N_{c-DS} = -(-D_{DS} \cdot (\ln \max_{DS} - \ln \max_{SEM}) - \ln N_{c-makr}) \tag{6.1c}$$

$$N_{c-DS} = e^{\ln N_{c-DS}} \tag{6.1d}$$

$$\ln N_{c-SEM} = -(-D_{SEM} \cdot (\ln \max_{SEM} - \ln \min_{SEM}) - \ln N_{c-DS}) \tag{6.1e}$$

$$N_{c-SEM} = e^{\ln N_{c-SEM}} \tag{6.1f}$$

The axis intercept n of each linear function can be obtained by:

$$n_{makr} = D_{makr} \cdot \ln \max_{makr} \tag{6.2a}$$

$$n_{DS} = \ln N_{c-DS} + D_{DS} \cdot \ln \max_{SEM} \tag{6.2b}$$

$$n_{SEM} = \ln N_{c-SEM} + D_{SEM} \cdot \ln \min_{SEM} \tag{6.2c}$$

The grain size parameters can be calculated by

$$r = e^{\frac{\ln N_c - n}{-D}} \tag{6.3}$$

for each integer between 0 and N_{c-SEM}, using the respective N_c, D, and n values at the transition points.

Now the surface area of each of the assumed circular particles can be obtained by

$$area = r^2 \cdot \frac{\pi}{4} \tag{6.4}$$

The surface areas of the particles will be summed to obtain the total surface area of all particles.

The same procedure will be repeated with using D_{DS} instead of D_{SEM}. The loss of the finer fraction of the melt particles can be calculated by comparing the sum of the surface area of the first and second run (Fig. 5.7).

A second correction was used for the Otting suevite and the melt-poor suevite from Wörnitzostheim. In these suevites, almost no melt particles could be observed at the SEM scale. The minimum size of the melt particles was found to be 100μm. Additionally dissolution patterns on melt rims of up to 50 - 100 μm can be frequently observed (Fig. 6.8).

Under the assumption that a minimum of a 50 μm thick rim of each melt particle was altered into clay minerals, we added to each grain size parameter r 100 μm. The new grain

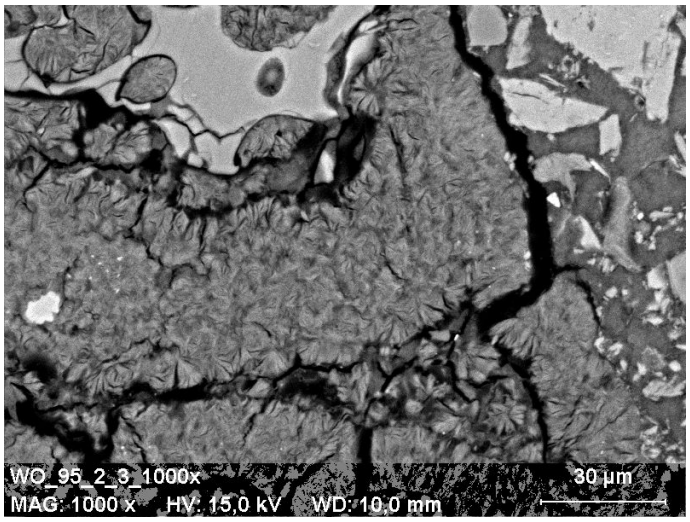

Fig. 6.8.: SE (secondary electron) image of a Wörnitzostheim sample from 95.2 m depth: upper left: melt particle with dissolution rim (fine phyllosilicate matrix from lower left to middle part of the image), right: typical suevite matrix with lithic clasts.

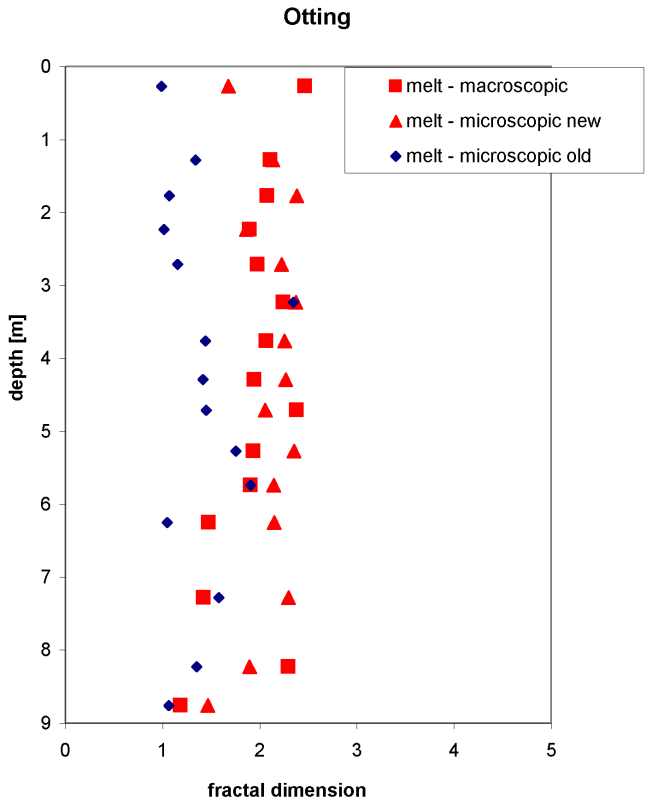

Fig. 6.9.: Fractal dimension of melt particles of the Otting suevite before and after correction of the melt particle sizes by an alteration rim; macroscopic = $2 < r < 63$ mm, microscopic = $0.25 < r < 2$ mm; r functions as grain size parameter.

size parameters were plotted in a cumulative frequency diagram and a new fractal dimension was calculated, as described in Chapter 5. Whereas before the fractal dimension of these suevite units were lower at the thin section scale than at the macroscopic scale, the fractal dimension of thin section and macroscopic scale is similar after correction, as observed for all other suevite units (Fig. 6.9). The surface area and the total loss of melt particles were obtained, as described above.

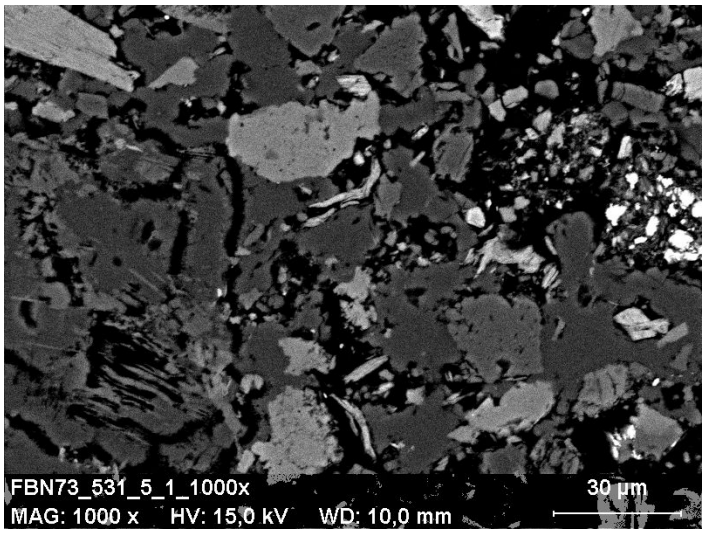

Fig. 6.10.: SE image of FBN73 sample from 532 m depth showing voids between melt matrix and lithic clasts.

A third correction was done for the FBN73 suevite, below 330 m. It has been proposed that immediately after the impact the inner Ries crater was filled by a 270 m thick melt sheet (Grieve et al. 2010). Under the assumption that the unfilled voids of the inner crater suevite below 330 m (Fig. 6.10) were formerly filled by melt, the void content was added to the melt content of the FBN73 suevite.

The results of the melt content calculations are given in Fig. 6.11. In all drill cores, the melt content increases with depth with a maximum value of 40% for FBN73, 90 % of Enkingen in coherent melt layers, 60% for Wörnitzostheim, and 70% for Otting. With the exception of Enkingen, where the suevite merges into an impact melt rock at 86 m depth, at a distinct depth the melt value decreases again up to the transition to the underlying target rocks or Bunte Breccia.

6.5. Discussion

Chemical relations between the melt particles and suevite matrices in the suevite drill cores of the Ries crater

Homogenous melts can be detected for the crater suevite below 380 m, the lower most suevite unit of Wörnitzostheim, for the Otting suevite, and from Stähle (1972) for all outcrop suevites. Inhomogeneous melts occur in the upper part of Wörnitzostheim, in the Enkingen drill core, and in the melt-rich suevite above 378 m of the crater suevite.

While the glasses of the outer crater suevite are quenched at the bottom of the deposits and in a few places also at the top, elsewhere the glasses are devitrified and commonly

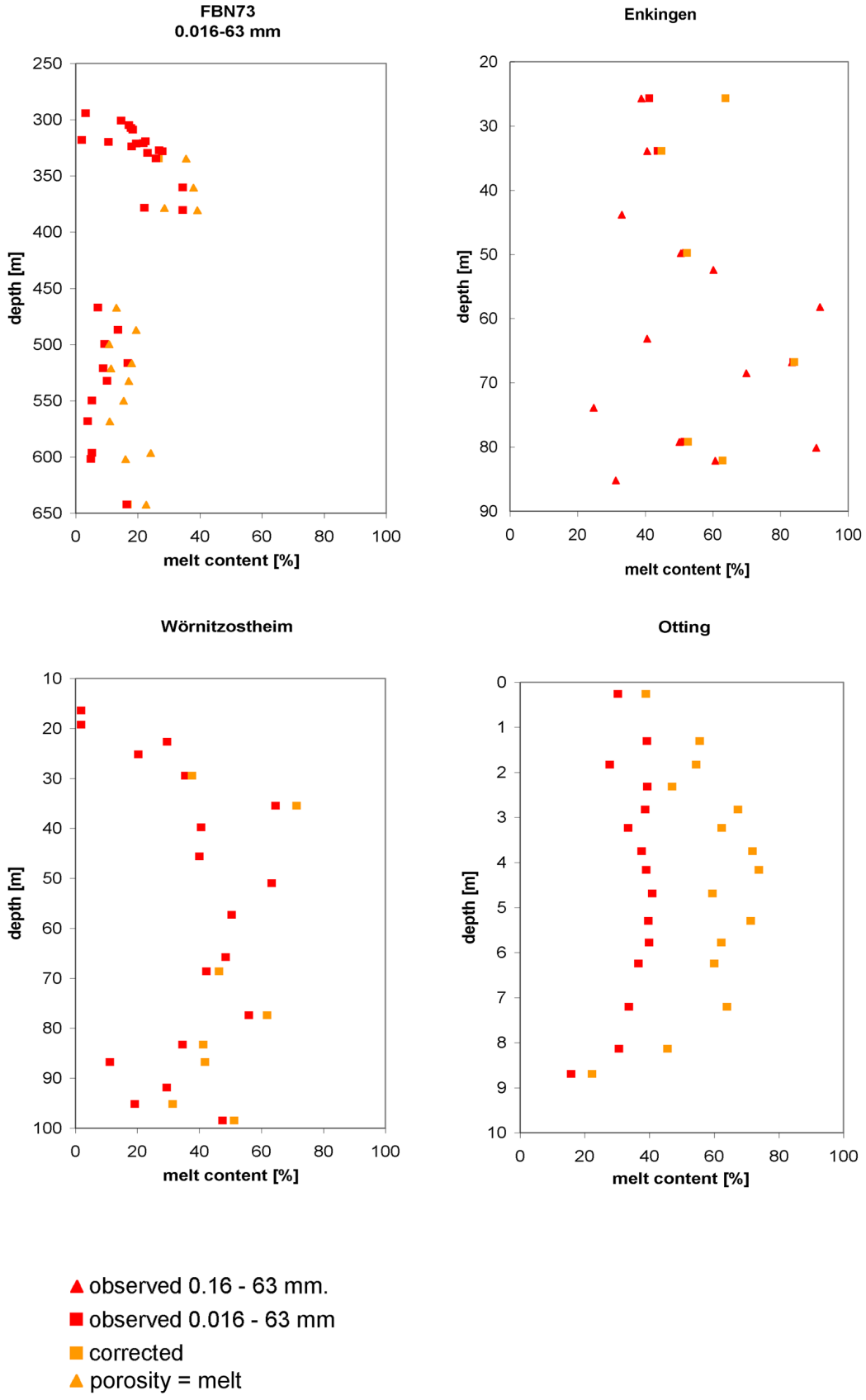

Fig. 6.11.: Melt content of FBN73, Enkingen, Wörnitzostheim, and Otting drill core measured and corrected by grain size characteristics.

altered (Engelhardt et al. 1995). One characteristic of the melt particles of the outer crater suevite is their uniform bulk composition (Stähle 1972), which was also observed for the lowest suevite layer of Wörnitzostheim. However, pure silica glass and schlieren of different colors have chemical compositions different from the bulk composition, which appears not to be significant as the color differences are mainly caused by oxidation from Fe^{2+} to Fe^{3+} (Engelhardt 1967).

In contrast, the chemical composition of the upper Wörnitzostheim suevite and Enkingen suevite is rather inhomogeneous. The detected chemical composition varies from K-poor to K-rich melt particles and in the degree of Fe, Mg depletion. Due to the fact that the hydrothermal alteration results in an increase in K and Fe (Osinski 2005), it seems likely that the different melt particles were affected by different intensities of several alteration processes, depending on their primary composition. The chemical composition of the melt particles of the melt-rich unit of FBN73 above 378 m and of the sorted suevite at 378 m is also inhomogeneous. However, in contrast to Enkingen and Wörnitzostheim the melt particles are differentiated into melts of lower and higher K concentration, but the K concentration is in total lower than for Wörnitzostheim and Enkingen.

Three possibilities could explain these compositional variations between the melt particles of the suevite rocks. It could be the result of incomplete mixing and homogenization of melts, from different compositions of target rocks, of unmixing of immiscible melts, or of post-impact modifications such as hydrothermal alteration. Whereas the composition of the silicate matrices of the outer suevite and the melt-rich suevite of the crater suevite above 380 m are mainly composed of Fe-rich montmorillonite of similar compositions, but distinct from melt composition, the chemical composition of the suevite matrix of the crater suevite below 380 m is almost identical to the composition of the melt particles and chemically homogeneous. Thus, it can be concluded that the crater suevite below 380 m represented a coherent impact melt, before alteration, with a high content of lithic clasts up to block sizes. Apparently, the composition changed greatly, during the alteration processes, due to the fact that the current composition is completely different to any described host rock compositions (Graup 1977).

Alteration processes in the Ries suevite

The most dominant mineral assemblages, the clay-silica-K feldspar-zeolites indicate hydrothermal alteration at low pressures and temperatures of 100 - 300°C at the Ries crater. The post-impact alteration of the Ries suevite started with an early high temperature alteration (200 - 300°C), which was restricted to thick suevite depositions (FBN73, Enkingen and Wörnitzostheim) and was characterized by K-metasomatism and minor albitization of lithic clasts. These early hydrothermal fluids were controlled by the interaction of ground waters with feldspars or impact melts. The circulation of the hydrothermal fluids resulted in an increase in K and Fe and in a decrease of Si, Ca, and Na of impact glasses (Osinski 2005).

Due to the fact that glass is very susceptible to fluid rock interaction, the melt particles started to crystallize and the intensity of alteration increased in the glassy melt compared to the lithic clasts (Hecht et al. 2004).

The main stage of hydrothermal alteration was characterized by argillaceous alteration and zeolitization, associated with a progressive cooling of the inner and outer suevites. At this stage, all impact glasses in the crater suevite were replaced by clay minerals, analcite, and zeolites and alteration of the lithic clasts occurred. The presence of alkali and calcic zeolites is indicative of weakly alkaline hydrothermal solutions at this alteration stage (Osinski 2005). The alteration of the outer suevite is mainly characterized by montmorillonite and phillipsite formation. The lack of illite interlayers in the montmorillonite constrains the alteration to $<$100 - 130°C (Newsom et al. 1986). The final stage resulted in deposition of calcite and of clays in cavities and fractures.

The presence of an overlying crater lake played a critical role in determining the level of hydrothermal alteration of the suevites. The alteration of the outer suevites occurred under undersaturated conditions, with the main source of water being from precipitation of meteoric water (Newsom et al. 1986). Additionally, higher alteration intensities of the FBN73, Enkingen, and Wörnitzostheim suevites are due to their greater thickness, allowing circulation to continue for a longer period of time.

Total melt volume in the Ries suevite

The estimation of the total volume of suevite in the inner crater is uncertain, due to the fact that suevite lens in the crater has a quite irregular shape. However, based on geophysical data the total volume of the crater suevite was estimated to 9 - 11 km^3 (Pohl et al. 1977, Stöffler 1977). The volume of the outer suevite was estimated to 0.2 - 0.4 km^3 (Stöffler 1977). This estimation was based on geological distribution of the outcrop suevites. This volume contains large uncertainties, due to the fact that the degree of erosion, which affected present suevite distribution, is almost unknown. Furthermore, recently, several drill cores between the inner ring and crater boundary have been undertaken by the Bayrisches Geologisches Landesamt, with suevite occurrences ranging from 1 to 80 m thickness in almost all drill cores (Poschlod, 2010, personal communication). Thus, the volume estimation of the outer suevite by Stöffler (1977) seems to be an underestimate.

Comparing the results of the melt content of the crater suevite with the total volume of the crater suevite, a melt estimate in the inner crater of $\sim$2 km^3 can be calculated. Under assumption of more or less continuous suevite deposition between inner ring and crater boundary of just 5 m thickness, the total volume of the outer suevite will increase to $\sim$2 km^3. Comparing with the results of the melt content the total melt volume would be 1.2 km^3 in the outer suevites.

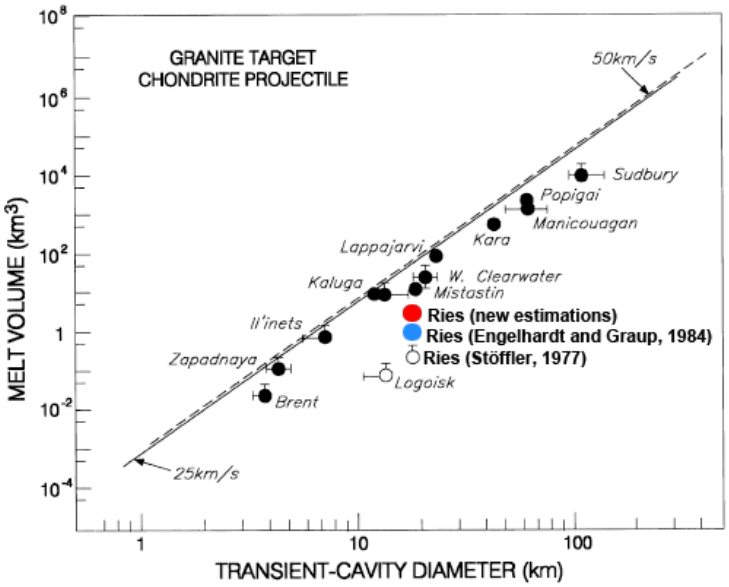

Fig. 6.12.: Impact melt volume of the Ries crater versus transient cavity diameter for impacts of 25 km/s and 50 km/s in comparison with estimates from other terrestrial impact structures (after Cintala and Grieve 1994, Dressler and Reimold 2001)

For an estimate of the total melt volume of the Ries crater, the impact melt occurrences have to be taken into account and, additionally, the evidence for carbonate melt which has been predicted to be 0.4 km^3 (Graup 1999, Stöffler et al. 2002). In a rough estimate, the melt occurrence in the inner crater seems to be similar to the melt occurrences outside the inner ring and the total melt volume seems to be still less but comparable to the Mistastin and West Clearwater craters, both of similar size to the Ries crater (Fig. 6.12) (Cintala and Grieve 1994, Dressler and Reimold 2001). However, the impact melt volume of the Ries crater will only be a rough estimate until the exact volume of the Ries suevite and the coherent impact melt occurrences is known.

6.6. Conclusion

The results of this Chapter show that the suevite can be chemically distinguished in the following subunits:

1. Strongly altered suevite, with similar melt and matrix composition in the upper most part of the crater suevite, of the Enkingen and Wörnitzostheim suevite resulting of lake water circulation.

2. Inhomogeneous suevite, with differentiation in K-poor and K-rich melt with either silicate matrix similar in chemistry to the melt or non existing silicate matrix. This type of suevite can be found in the inner crater suevite above 380 m and, in the Enkingen suevite, and in the upper part of the Wörnitzostheim suevite (above 80 m). The alteration intensity of these suevites decreases with distance from the crater center, which results either from the shallowing of the overlying crater-lake and/or from transportation processes out of the inner crater.

3. Chemical homogeneous suevite, with similar melt and matrix composition, which can be considered as the original impact melt in the inner crater suevite below 380 m. This suevite unit is strongly altered by hydrothermal processes.

4. Chemical homogeneous suevite, with different melt and matrix composition. This type can be found in the lower part of the Wörnitzostheim suevite (below 80 m), the Otting suevite, and is described by Stähle (1972) for all outer crater suevites. This suevite type was transported and sedimented in a different process compared to the overlying inhomogeneous suevite.

Clearly, water appears to play a major role in the suevite formation process (explosion efficiency, transportation, and alteration). Hence, understanding the role of water during the formation of suevite should be one of the major questions for future studies. Such studies could provide important clues for the whole process of suevite formation. For understanding the role of water according the suevite and therewith the original composition of the suevite matrix, which is still one of the most puzzling questions, it is essential to understand the different alteration processes of all suevite units. Therefore, a detailed clay mineral analysis of all suevite drill cores is absolutely necessary and key to identify the role of water during and after the impact.

7. Summary and Reconstruction of suevite genesis

7.1. New subdivision of the suevite units of the Ries crater

Based on the structural, petrological, and geochemical characteristics of the various investigated suevite units of the Ries drill cores, it is necessary to propose a new subdivision of the suevite units of the Ries crater. The following parameters are used for this subdivision:

1. Chemical composition of the melt particles, in particular regarding inhomogeneity and homogeneity,

2. Chemical and mineralogical composition of the suevite matrix, in comparison to the melt particles,

3. Specific properties determined through stereometric parameters, such as grain size, grain shape, and content of components.

The suevite subdivision is given by an overall view in Fig. 7.1. The localities of all drill cores are given in Fig. 3.1.

The drill core of Nördlingen is subdivided in the sedimentary units from 296 to 331 m depth, in the melt-rich suevite from 331 to 378 m depth, and in the melt-poor suevite from 380 to 602 m depth, which is separated from the overlain unit by a layer of sorted suevite between 378 and 380 m depth.

Sedimentary units (296-331 m): The sedimentary units can be divided in 3 subunits: from 296 to 309 m, from 309 to 314 m, and from 314 to 331 m. Whereas the two upper subunits are covered by a decimeter thick lapilli layer, respectively, the sample recovery of the upper layer of the lower sedimentary unit is too small to exclude a lapilli layer. Each sedimentation cycle is indicated by an increase in grain-size with depth and a simultaneously increase in the content of lithic clasts and melt, which abruptly drops down at the transition to the underlying

cycle. The upper layers of each cycle are mostly well-sorted. The melt particles are strongly altered and similar to the surrounding silicate matrix in composition .

Melt-rich suevite (331-380 m): Between 331 and 380 m, the melt content reaches 40%, the highest value of the whole drill core. Here, the grain-size distribution is constant with depth and passes between 378 and 380 m into a well sorted interlayer. The composition of the melt particles is differentiated into a K-rich and K-poor melt. However, the melt particles are strongly altered and, above the sorted interlayer, the composition of the melt particles is similar to their surrounding silicate matrix.

Melt-poor suevite (380-602 m): Below 380 m, the melt content decreases to 20% and continues to decrease down to 5% to the transition to the basement at 602 m depth. Whereas the grain sizes of the suevite particles decrease with depth, the content of crystalline blocks, which interrupt the suevite, increases. The composition of the melt particles is homogenous and K-poor in this core section and corresponds almost exactly to the composition of the silicate matrix. Hence, it can be assumed that this suevite unit represents the primary continuous impact melt, which is strongly interrupted by crystalline basement rocks.

The suevite of the Enkingen drill core can be considered as a uniform suevite unit, with the upper meters strongly reworked after deposition and passing into an impact melt rock below 86 m depth. The Enkingen suevite shows, with its coherent melt layers between 66 and 86 m depth, the highest content of impact melt of all drill cores. The composition of the melt is strongly differentiated in a K-poor and K-rich melt, which have a higher Fe and Mg content compared to the melt-rich unit of the Nördlingen drill core. In the lower units of the Enkingen drill core, matrix fillings are either carbonaceous or the suevite cavities are not filled. Frequently, the suevite particles are sintered to a large mass. The grain sizes increase slightly with depth.

The suevite of Wörnitzostheim is similar to the Enkingen suevite, until 80 m depth. The upper meters of the suevite are strongly reworked and the composition of the melt particles is differentiated in a K-poor and K-rich melt. The grain-sizes also slightly increase with depth but are, in total, smaller than in Enkingen and the grains are more rounded. Matrix fillings of the lower units are also either carbonaceous or do not exist. In contrast to Enkingen, below 80 m depth, the Wörnitzostheim suevite passes into a suevite with completely different optical and chemical properties. Whereas the color of the suevite of the upper part is rather yellow to reddish, the color of the suevite of the lower part is grey. The melt particles of this section are chemically homogenous, corresponding to a mixture of the chemical composition of the basement rocks. The composition of the silicate matrix is distinctly different from the melt

particles and formed by secondary clay minerals. The melt content and the grain-sizes of the lower suevite are constant with depth but grains are smaller than the particles of the overlying upper part, where larger melt fragments can be observed occasionally.

The Otting suevite is similar in its optical and chemical properties to the lowest Wörnitzostheim suevite. The melt particles show a homogenous chemical composition, which corresponds to a mixture of the chemical composition of the basement rocks. The composition of the silicate matrix is also distinctly different from the composition of the melt particles and is formed by secondary clay minerals. The melt content and grain-size are almost constant with depth, but lower than for Wörnitzostheim, and more rounded. In the lowest meter, at the transition to the Bunte Breccia, the grain sizes decrease strongly with depth.

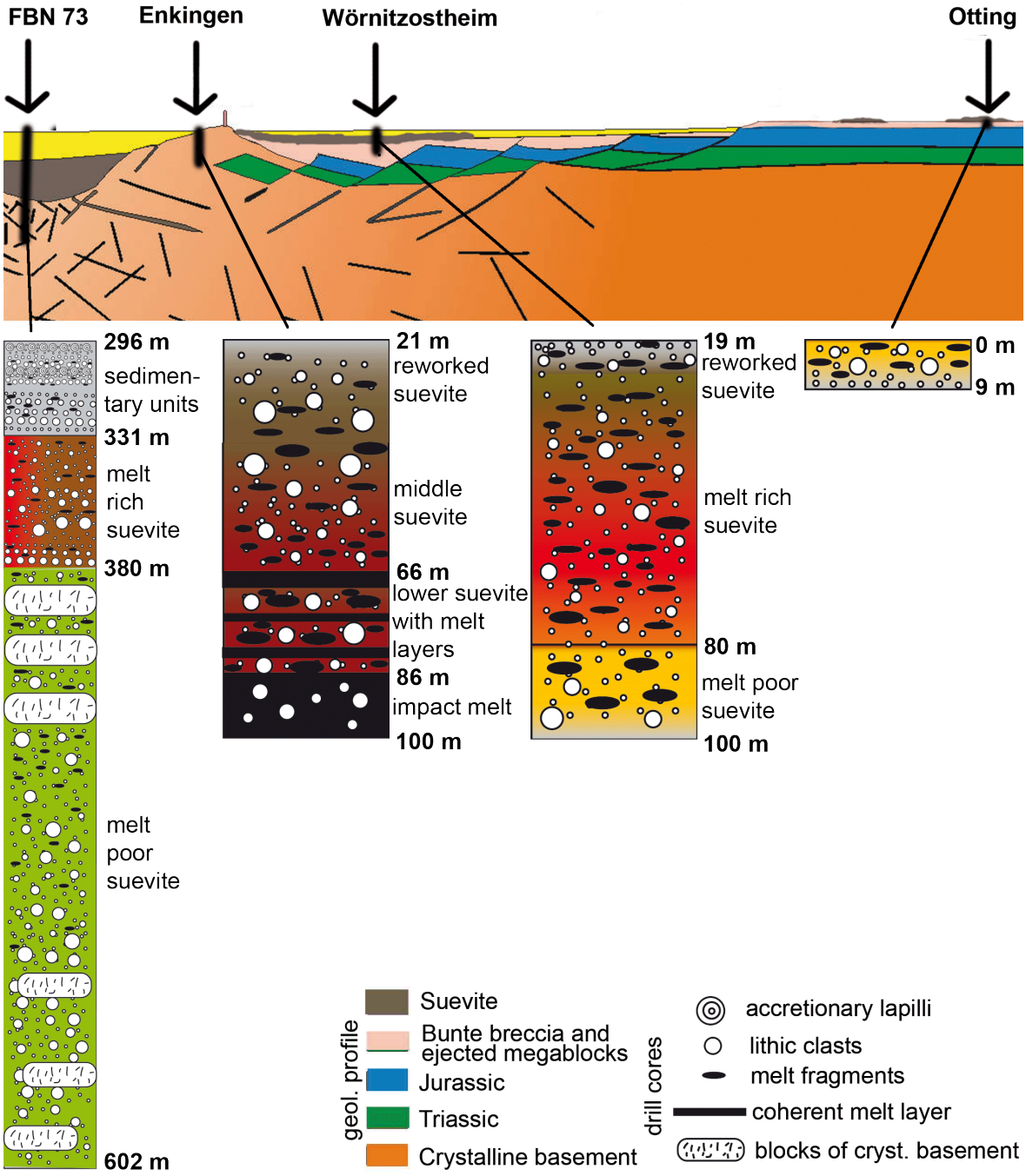

Fig. 7.1.: Profiles of suevite drill cores of research drilling Nördlingen 1973 (FBN73), Enkingen, Wörnitzostheim, and Otting. The subdivision of the suevite units is based on chemical, mineralogical, and stereometric aspects. Grey: strongly altered suevite, brown-red: suevite with differentiated melt in K-poor and K-rich, green: suevite with homogenous melt and same composition of melt and matrix, yellow: suevite with homogenous melt and different composition of melt and matrix. Geological profile after Pohl (1977).

7.2. Processes of the suevite genesis of the Ries crater

Processes of the suevite genesis of the Ries crater are concluded from textural, petrographical, and chemical observations as well as numerical modeling.

To-date, it is widely accepted that during the compression stage of the crater formation a melt zone was formed in the primary crater, which is underlain by fine to coarse broken, compressed, and mainly crystalline rock material. During the excavation stage the target rocks were set in motion radially outwards. Due to the fact that in the lower central crater the target material could not laterally in response to this motion results in a strong compression. During the following refraction, the crater floor expanded upwards and the former comminuted rocks intruded as a polymict breccia into the newly opened up fractures. The refraction wave supplied the radial material flow at the crater margin with an additional upward movement, and the Bunte Breccia was ballistically ejected at the crater rim. The Bunte Breccia consists primarily of sedimentary rocks and was deposited outside the crater, where it stirred up and mixed in unconsolidated rocks of the impacted surface. At the end of the excavation stage, the crater size had extend to almost its final size, because of the ejection of the Bunte Breccia. The rebound of the crater floor led to a slumping of large slabs from the crater rim. This movement in the opposite direction to the ejecta produced a torsional moment, which generated the terraced crater rim zone and the inner ring of the Ries crater (French 1998, Hüttner and Schmidt-Kaler 2003).

In accordance with crater-scaling laws (Cintala and Grieve 1994) and the newest modeling (Artemieva et al. in preperation), approximately 15 km^3 melt were formed during the Ries crater event with 25% of the melt emanating from sedimentary cover layer. During the excavation stage, 1/3 of the melt, mainly sedimentary melt, was ejected, so that the remaining melt pool in the crater was distinctly depleted in sediment melt up to 2% (Artemieva et al. in preperation).

In the literature mainly two different possibilities have been discussed how, when, and out of what the suevite was formed during the crater formation process:

1. A mixture of vapor, melt, and lithic clasts was engulfed in an upwards rising, turbulent, conical ejecta plume and a mixture of melt fragments and lithic clasts was deposited after the plume collapsed inside the crater and outside on top of the Bunte Breccia (e.g., Stöffler 1977, Engelhardt and Graup 1984, Engelhardt 1997).

2. After the collapse of the ejecta plume the suevite was deposited out of an outwards flowing pyroclastic flow (Newsom et al. 1986, Newsom et al. 1990, Bringemeier 1994). Osinski et al. (2004) even concluded a deposition out of a melt-like flow as a special case.

According to the modeling of Artemieva et al. (in preperation), an ejecta plume was formed in the early stages of the crater formation, before the transient cavity reached its final size.

This ejecta plume consisted initially of vaporized and molten projectile and sedimentary material. Later, crystalline material, mainly melt particles, were also included. In total the ejecta plume had a volume of ~ 4 km^3 sedimentary materials and 0.02 km^3 material from the crystalline target (Fig. 7.2). After several minutes, the plume dispersed beyond the crater rim and was deposited in the inner crater with a maximum thickness of 1 - 2 m and outside the crater on top of the Bunte Breccia, with probably a smaller thickness. Osinski et al. (2004) interpreted the lowermost fine-grained layer at the base of the outer suevites at the transition to the Bunte Breccia (Engelhardt et al. 1995) as the true fall-back suevite of this early ejecta plume (Fig. 7.3)

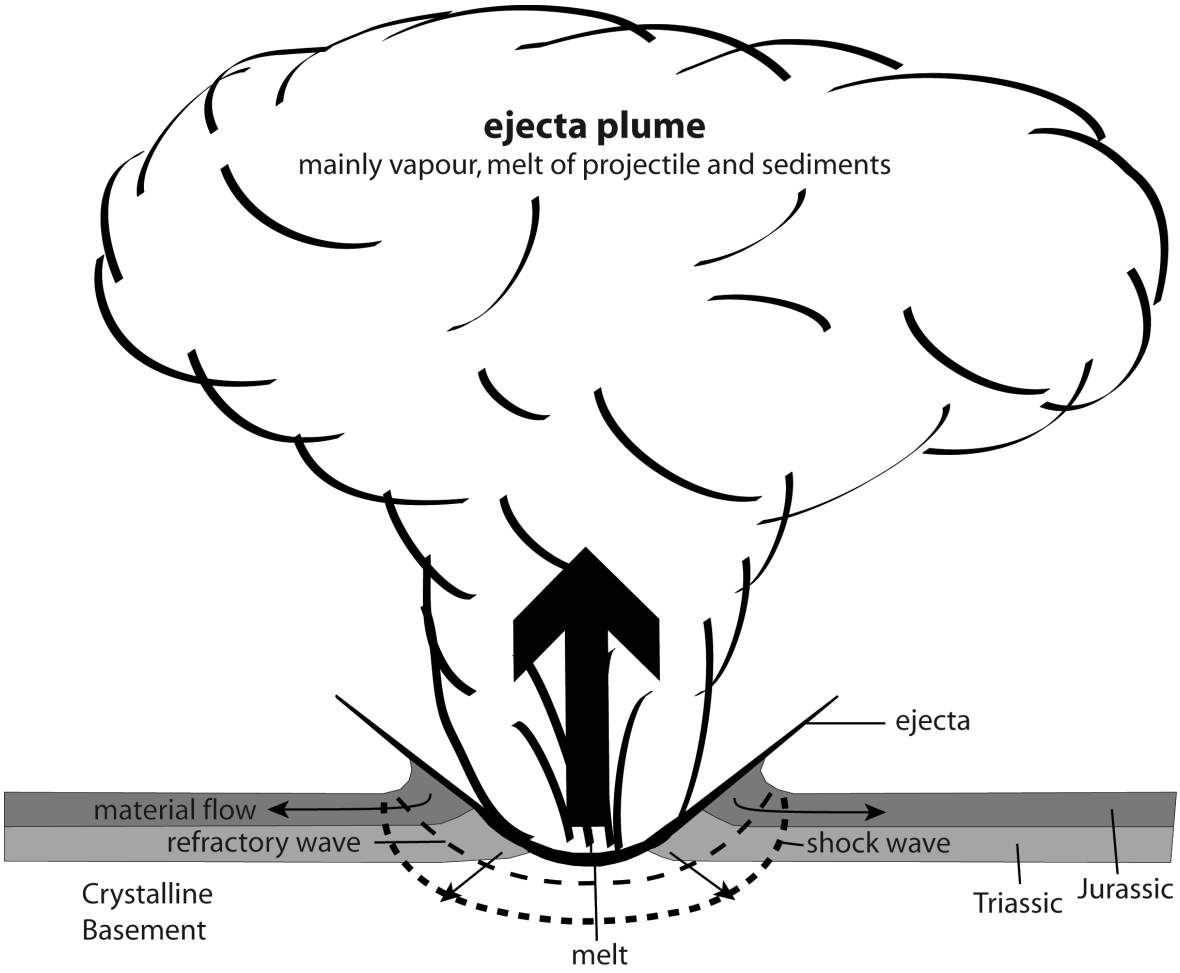

Fig. 7.2.: Schematic illustration of the early ejecta plume formation during the excavation stage (modified from French (1998) and Pohl et al. (1977)). Geological profile is vertically exaggerated.

There still remains the unanswered question how the remaining up to 80 m thick suevite deposits outside the inner ring was formed. According to Artemieva et al. (in preperation), an ejecta plume cannot carry enough material to generate such massive deposits. The present work also shows that the particles of the outer suevite were transported with a lateral component, similar to a pyroclastic flow or surge. However, to trigger such a movement volatile elements in the melt are necessary. Due to the fact that the amount of natural volatiles

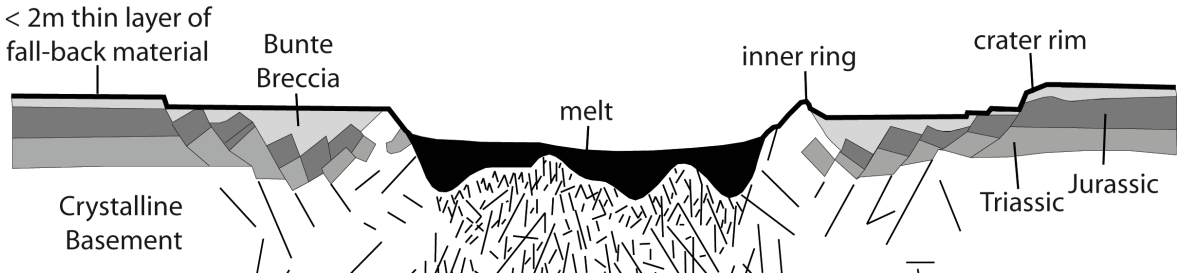

Fig. 7.3.: Ries profile after deposition of the early ejecta plume (modified from Pohl et al. (1977)). Geological profile is vertically exaggerated.

in the remaining melt lake is too low for an explosive mixture further volatiles had to be delivered into the system (Artemieva et al. in preperation). A water-melt-ratio of 0.2 would maximize the explosion power of the melt. Such a phreatomagmatic explosion could generate a melt moving upwards into the rising ejecta column, with an expansion velocity of up to 700 m/s.

There are two possible activators for a phreatomagmatic explosion at the Nördlinger Ries:

1. Water from rivers, flowing back into the crater, or water from the crater lake reaching the melt through fractures (Artemieva et al. in preperation).The problem with this possibility is that as soon as surface water reaches the melt it vaporizes and an isolation layer between melt and water will be formed.

2. Ground water returning into the crater after the crater formation and reaching the melt. Newsom (1980) has discussed the presence of ground water in the context of hydrotherm activity. Extending his ideas, this water could have caused a phreatomagmatic explosion.

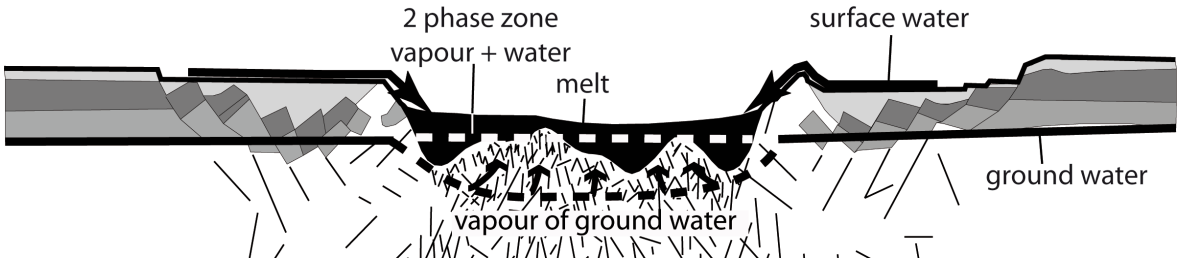

Fig. 7.4.: Interaction of groundwater and surface water with the melt lake. Below the melt surface a 2-phase-zone of vapour and water will be formed (modified from Pohl et al. (1977), Newsom 1980). Geological profile is vertically exaggerated.

Hence, the contact of melt and water alone could not initiate an explosion but first the isolation layer would need to be destroyed by further processes (Fisher and Schmincke 1984). In contrast, in the second case, the ground water would start to interact with the melt lake directly after its formation. The ground water level dropped due to crater formation to a level below the crater. Because of the high surrounding temperature in this volume of the target, the water vaporized and expanded. It escaped through the broken target rocks mainly upwards,

where it intermingled with the melt. Below the melt surface, a two face water-vapour-layer would be formed. Newsom (1980) concluded that all the water would escape upwards through melt fractures. If we follow the train of thoughts of Artemieva et al. (in preperation), this water could initiate a phreatomagmatic explosion as soon as it reaches a critical concentration, where only the upper part of the melt pool would be involved (Fig. 7.4). While crater formation finished in several minutes, the length of time of the phreatomagmatic reaction is uncertain. However, a distinct temporal hiatus seems to be probable.

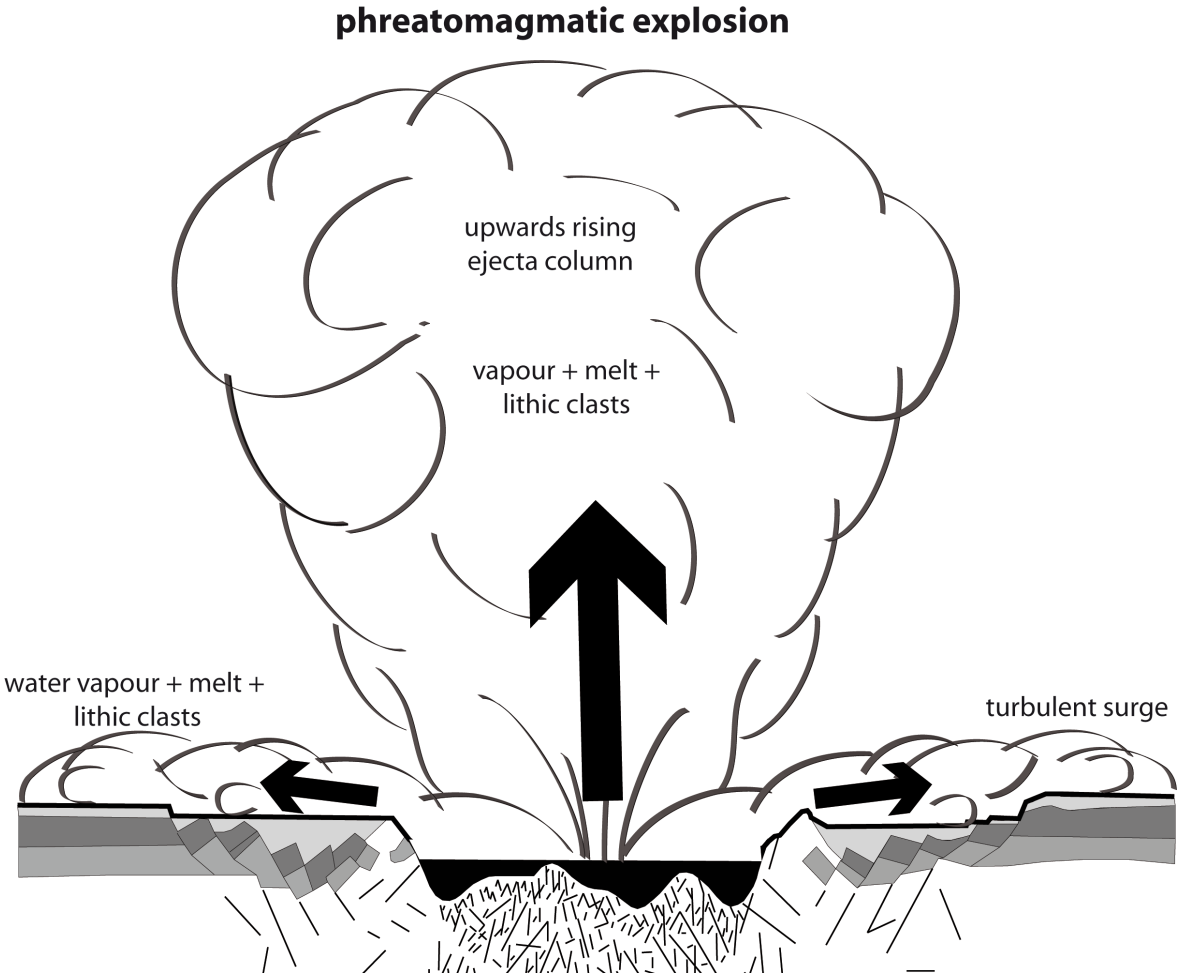

Fig. 7.5.: Schematic illustration of the phreatomagmatic explosion. An upwards rising ejecta column will be formed and contemporaneously a radially outwards moving basal surge (modified from Pohl et al. (1977), Branney and Kokelaar (2002). Geological profile is vertically exaggerated.

An ejecta column, generated in such a phreatomagmatic explosion, is always associated with a radial outwards spreading, basal, high turbulent pyroclastic surge (Fig. 7.5). Such surges are usually massive deposits, which replicate the surface relief without erosion (Francis and Oppenheimer 2004). Basal surges are loaded with melt particles, which are strongly fragmented by the water-melt-contact, and lithic clasts. Because of the high water vapor content, the following deposits are hydrous and the finer glass particles will be transformed into clay minerals immediately, which will cement the deposit. Due to this, the melt fragments

of basal surge deposits are not sintered (Fig. 7.6) (Branney and Kokelaar 2002, Francis and Oppenheimer 2004).

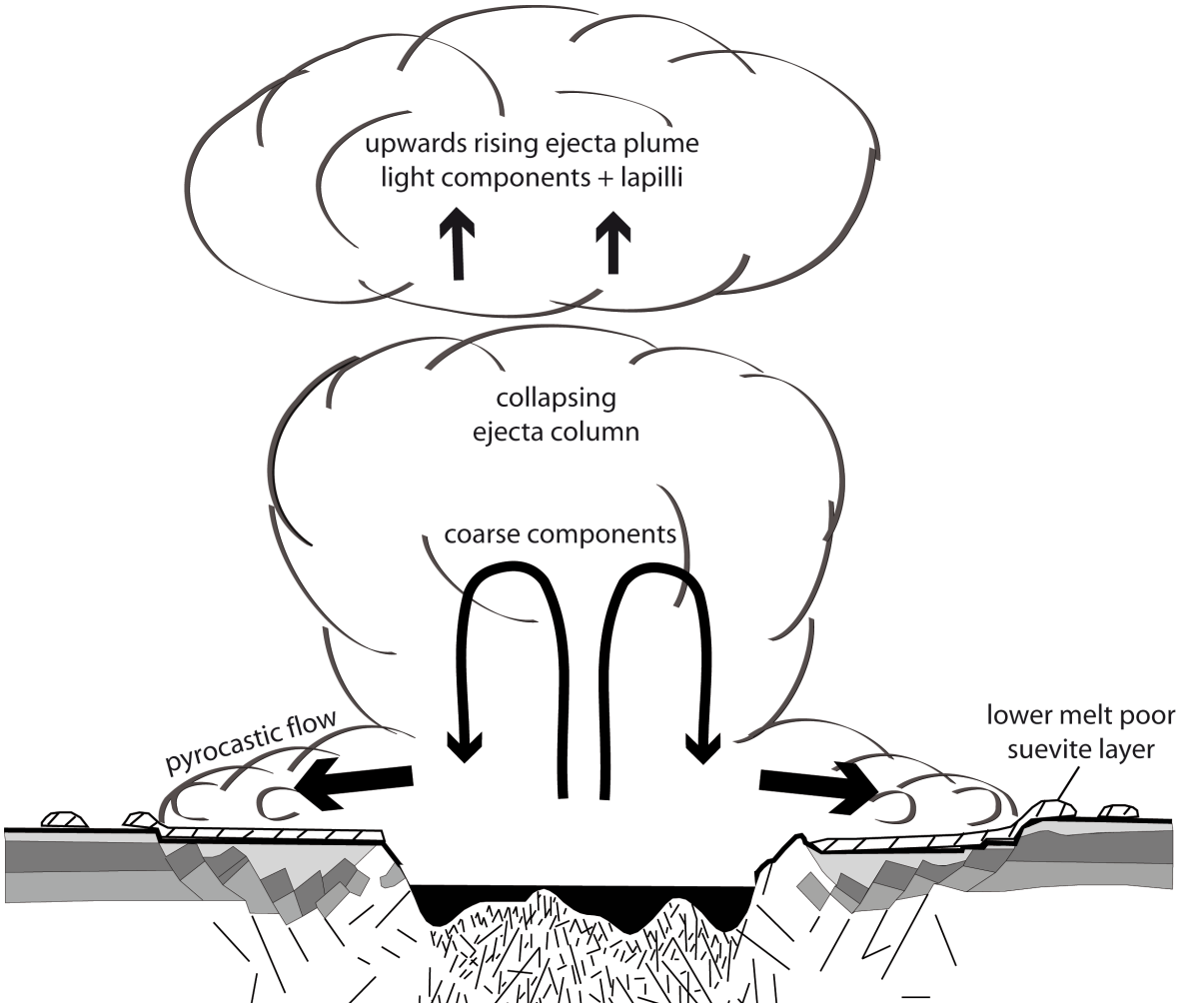

Fig. 7.6.: Schematic illustration of the upwards rising ejecta plume. The collapsing ejecta column initiates an outwards moving pyroclastic flow. Previously, the basal surge has been deposited on top of the Bunte Breccia with more and more patchy like distribution with distance from its source (modified from Pohl et al. (1977), Branney and Kokelaar (2002)). Geological profile is vertically exaggerated.

After a short time period the ejecta column starts to collapse due to the high content in melt fragments and lithic clasts and a pyroclastic flow spreads out, which is slower and denser than the surge. During the collapse of the ejecta column, surrounding air will be assimilated, which results in the descent of the heavy particles inside the forming pyroclastic flow and the ascent of the light components in the ejecta plume rising upwards above the pyroclastic flow (Fig. 7.6) (Woods and Wohletz 1991). This lighter material will be deposited as fall-back material later. Pyroclastic flows are density stratified and the melt and lithic particles will be carried in suspension by gases and turbulences. In very massive pyroclastic flow deposits with a high melt content a sintering of the melt particles can occur in such a way that pyroclastic flow deposits can be transformed into a coherent melt rock at their base (Ross and Smith 1961, Francis and Oppenheimer 2004). Because of their high density, pyroclastic flows are affected

by gravity. Indeed, they partly overlie the pyroclastic surge deposits but will be spread over much shorter areas (Druitt 1998). In the Nördlinger Ries, the movement of such a pyroclastic flow was probably restricted by the crater rim (Fig. 7.7).

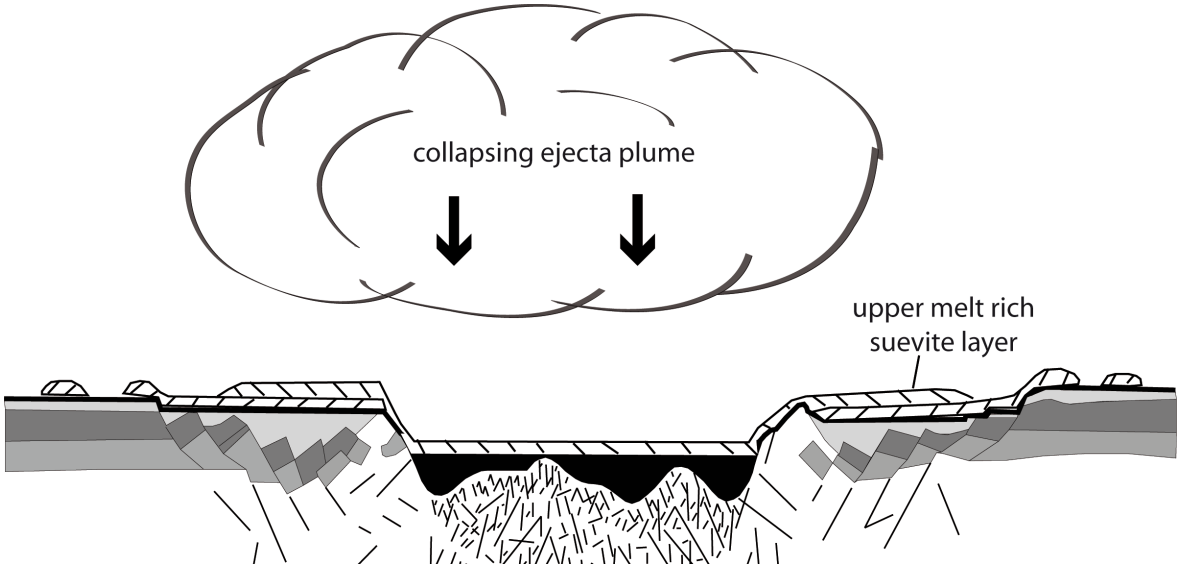

Fig. 7.7.: Schematic illustration of the collapsing ejecta plume. Previously, the pyroclastic flow has been deposited as melt-rich suevite in the inner crater and overlain the first suevite layer between inner ring and crater rim (modified from Pohl et al. (1977)). Geological profile is vertically exaggerated.

In the ejecta plume, which rises in the meantime and is still water vapor loaded, accretionary lapilli will form (Fig. 7.6). Due to the fact that the lapilli of the Ries crater show just one rim, it can be concluded that they were deposited directly out of the ejecta plume, together with the residual material on top of the former deposited units (Fig. 7.7) (Brown et al. 2010). According to Artemieva et al. (in preperation), the stereometric properties of the upper sedimentary units of the crater suevite can only be explained by deposition out of a water column. Hence, these units can be explained by two different possible sedimentation mechanisms:

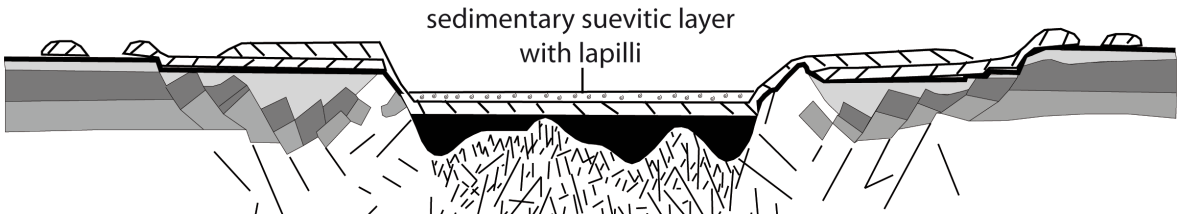

Fig. 7.8.: Ries profile after phreatomagmatic explosion. The components of the ejecta plume have been deposited by sedimentary processes above the melt-rich suevite inside the crater. Thicknesses of layers are not true to scale (modified from Pohl et al. (1977)). Geological profile is vertically exaggerated.

1. The sedimentary units resulted from several ejection events and the fall-back products of the ejecta plume were deposited directly in a existing water layer inside the crater,

2. The fall-back products of the ejecta plume were reworked by incoming water in the crater and were deposited inside the developing water layer (Fig.7.8)

8. Outlook

.

In this thesis, it can be demonstrated that the suevite of the Ries crater was transported in pyroclastic flow-like and surge-like processes. Only the upper most part of the inner crater suevite appears to have fallen out of the ejecta plume. The process that leads to the formation of the pyroclastic flow-like and surge-like transport system remains unknown. One explanation could be that a phreatomagmatic explosion from the interaction of impact melt with surface or ground water triggered such transport systems. To prove this idea, more data concerning the Ries suevite are necessary.

First, the idea of the pyroclastic flow-like and surge-like processes should be tested. Recently, more than 18 suevite drill cores have been sunk in the Ries crater outside the inner ring, with suevite thicknesses from 1 to 80 m by the Bayrisches Geologisches Landesamt. Beside the common grey suevite, in some of these drill cores a reddish melt-rich unit as described for Enkingen and Wörnitzostheim has been detected (Poschlod, personal communication). The drill cores should be investigated in detail with respect to their grain size distribution, modal composition and chemistry of the melt particles and matrices. All results should be evaluated according to the suevite thickness, depth, and distance from the crater center. If the suevite was transported in pyroclastic flow-like and surge-like systems, the stereometric results should show distinct lateral transportation patterns, as described in Chapter 5, depending on the distance from the crater center. Furthermore, the detected reddish melt-rich suevites should be different in the chemical composition of their melt particles and matrices, compared to the underlying grey, relatively melt-poor suevite. The melt particles of the grey suevite should be similar in composition for all drill cores and should represent a chemical mixture of all basement rocks. In contrast, the chemical composition of the melt particles of the reddish melt-rich suevite should vary from K-poor to K-rich melt particles and in the degree of Fe, Mg depletion, depending on their distance to the crater center.

Second, the flow direction of the possible flow and surge systems should be determined. Therefore, it would be desirable to have more three dimensional data on the suevite particles, as obtained in the thesis for the quarries Aumühle and Seelbronn (north and south direction to the crater center). Three-dimensional-analyses of outcrop suevites, as described in Chapter 4, should be also performed for suevite outcrops in east and west quadrants of the crater. Possible outcrops would be Otting (east), Altebürg (south west) or Zipplingen (north west).

More possible suevite outcrops can be found in Hüttner and Schmidt-Kaler (1999).

Third, the data of the Ries suevite should be compared to other suevite-bearing terrestrial impact craters. Several impact craters have suevite outcrops in the inner part of the crater, e.g., Haughton crater (Nunavut, Canada) (Osinski et al. 2005) or Slate Islands (Ontario, Canada)(Dressler and Sharpton 1997). These craters could potentially help to test the potential relationship between inner crater suevite and phreatomagmatic explosion processes.

Fourth, clearly, water appears to play a major role in the suevite formation process (explosion efficiency, transportation, and alteration). Hence, understanding the role of water during the formation of suevite should be one of the major questions for future studies. Such studies could provide important clues for the whole process of suevite formation and provide a major distinction between terrestrial and most non-terrestrial impacts. The exceptions are certain impacts on Mars. Therefore, a detailed clay mineral analysis of all suevite drill cores in this study is key to identify the role of water during and after the impact.

Fifth, one unsolved question of the thesis is the origin of dike suevites in the basement rocks below the inner crater suevite. For forming these suevite dikes Stöffler (1977) proposes a ground surging process, in which the crater suevite intruded in open fractures of the crystalline basement. Under assumption that the lower crater suevite resembles the former impact melt, the model of Stöffler (1977) becomes similar to recent studies of **Lieger2009** who proposes an similar allochthonous origin for pseudotachylite melts in the Vredefort Dome. However, at Slate islands impact structure melt poor breccias, similar to melt poor suevites of the inner crater suevite of the Ries crater, occur beneath pseudotachylites. Even, sometimes the breccias cut across pseudotachylites and contain inclusions of them (Dressler and Sharpton 1997). To determine the formation time of these various "melt bodies" the composition of the original melt, which is possibly represented by the inner part of the large pseudotachylites, with the melt particles of the suevite should be compared. Thus, with analyzing of alteration patterns, the time-scale of the suevite formation according to the time of the impact event can be determined.

References

Allen, J.R. (1982). *Sedimentary structures, their character and physical basis*. Amsterdam, New York, Elsevier:663.

Allen, S. R. and R. A. F. Cas (1998). Lateral variations within coarse co-ignimbrite lithic breccias of the Kos Plateau Tuff, Greece. In: *Bulletin of Volcanology* 59:356–377.

Alvarez, L. W. et al. (1980). Extraterrestrial cause for the Cretaceous-Tertiary extinction. In: *Science* 208:1095–1108.

Artemieva, N. A. et al. (2009). Ries crater and suevite revisited: Part II modelling. In: *40th LPSC, Houston*:abstract 1526.

Artemieva, N. A. et al. (in preperation). Ries crater and suevite revisited - Observations and modelling Part II: Modelling. In: *Meteoritics and Planetay Science*:to be submitted.

Bashkirov, A.G. and A.V. Vityazev (1996). Statistical mechanics of fragmentation processes of ice and rock bodies. In: *Planetary and Space Science* 44.9:909–915.

Bauberger, W. et al. (1974). Petrographische Profildarstellung der Forschungsbohrung Nördlingen 1973 (von Meter 263 an bis zur Endteufe im Massstab 1:200). In: *Geologica Bavarica* 72:33–34.

Best, J.L. (1992). Sedimentology and event timing of a catastrophic volcaniclastic mass flow, Volcan Hudson, Southern Chile. In: *Bulletin of Volcanology* 54:299–318.

Branney, M.J. and P. Kokelaar (1992). A reappraisal of ignimbrite emplacement: Progressive aggradation and changes from particulate to non-particulate flow during emplacement of high-grade ignimbrite. In: *Bulletin of Volcanology* 54:504–520.

Branney, M.J. and P. Kokelaar (2002). *Pyroclastic Density Currents and the Sedimentation of Ignimbrites*. Vol. 27. Geological Society Memoir, London:143.

Bringemeier, D. (1994). Petrofabric examination of the main Suevite of the Otting Quarry, Nördlinger Ries, Germany. In: *Meteoritics and Planetary Science* 29:417–422.

Brown, R. J. et al. (2010). Origin of accretionary lapilli within ground-hugging density currents: Evidence from pyroclastic couplets on Tenerife. In: *GSA Bulletin* 122:305–320.

Burgisser, A. and J.E. Gardner (2006). Using hydraulic equivalences to discriminate transport processes of volcanic flows. In: *Geology* 34.3:157–160.

Capaccioni, B. et al. (2001). Directional fabric measurements: an investigative approach to transport and depositional mechanisms in pyroclastic flows. In: *Journal of Volcanology and Geothermal Research* 107:275–292.

Chao, E.C.T. et al. (1977). Vertical section of Ries sedimentary ejecta blanket as revealed by 1976 drill cores from Otting and Itzing. In: *LPSC, VIII*:abstr 163C.

Cintala, M.J. and R.A.F. Grieve (1994). "The effects of differential scaling of impact melt and crater dimensions on lunar and terrestrial craters: some brief examples". In: *Large meteorite impacts and planetary evolution*. Ed. by B.O. Dressler et al. Vol. 293. Geological Society of America, Special paper:51–59.

Cnudde, V. et al. (2006). Recent progress in X-ray CT as a geosciences tool. In: *Applied Geochemistry* 21:826–832.

Cockell, C.S. and P. Lee (2002). The biology of impact craters - a review. In: *Biological Reviews of the Cambridge Philosophical Society* 77:279–310.

Davies, I.E. and R.G. Walker (1974). Transport and deposition of resedimented conglomerates: the Cap Enrage Formation, Cambro-Ordovician, Gaspé, Quebec. In: *Journal of Sedimentary Petrology* 44:1200–1216.

De Paor, D.G. (1990). Determination of the strain ellipsoid from sectional data. In: *Journal of Structural Geology* 12.1:131–137.

Dressler, B. and G. Graup (1974). Gesteinskundliche Untersuchungen am Suevit der Bohrung Wörnitzostheim im Nördlinger Ries. In: *Aufschluss* 25.7/8:404–411.

Dressler, B.O. and W.U. Reimold (2001). Terrestrial impact melt rocks and glasses. In: *Earth Science reviews* 56:205–284.

Dressler, B.O. and V.L. Sharpton (1997). Breccia formation at a complex impact crater: Slate Islands, Lake Superior, Ontario, Canada. In: *Tectonophysics* 275:285–311.

Druitt, T. H. (1998). "Pyroclastic density currents". In: *The Physics of Explosive Volcanic Eruptions*. Ed. by R. S. J. Gilbert; J.S. ND Sparks. Vol. 145. Geological Society, London, Special Publication:145–182.

Engelhardt, W. v. (1967). Chemical composition of Ries glass bombs. In: *Geochimica Cosmochimica Acta* 31:1677–1689.

Engelhardt, W. v. (1997). Suevite breccia of the Ries impact crater, Germany: Petrography, chemistry, and shock metamorphism of crystalline rock clasts. In: *Meteoritics and Planetary Science* 32:545–554.

Engelhardt, W. v. and G. Graup (1984). Suevite of the Ries crater, Germany: Source rocks and implications for cratering mechanics. In: *Geologische Rundschau* 73:447–481.

Engelhardt, W. v. et al. (1995). Suevite breccia from the Ries crater, Germany: Origin, cooling history, and devitrification of impact glasses. In: *Meteoritics and Planetary Science* 30:279–293.

Fisher, R.V. and H.U. Schmincke (1984). *Pyroclastic Rocks*. Berlin, New York, Springer Verlag:472.

Förstner, U. (1967). Petrographische Untersuchungen des Suevit aus den Bohrungen Deiningen und Wörnitzostheim im Ries von Nördlingen. In: *Contributions to Mineralogy and Petrology* 15:281–307.

Francis, P. and C. Oppenheimer (2004). *Volcanoes*. New York, Oxford University Press:521.

French, B. M. (1998). *Traces of Catastrophes: A Handbook of Shock-Metamorphic Effects in Terrestrial Meteorite Impact Structures*. Vol. 954. LPI Contribution, Lunar and Planetary Institute, Houston:120.

Füchtbauer, H. et al. (1977). Tertiary lake sediments of the Ries, research borehole Nördlingen 1973 - a summary. In: *Geologica Bavarica* 75:13–19.

Gall, H. et al. (1977). Erläuterungen zur Geologischen Karte des Rieses 1:50000. In: *Geologica Bavarica* 76:191.

Gary, M. et al. (1974). *Glossary of geology*. Washington, D.C., American Geological Institute:860.

Gault, D. E. et al. (1963). *Fluid impact craters and hypervelocity high velocity impact experiments in metals and rocks*. Tech. rep. NASA Technical Note D-1767.

Glen, J.W. et al. (1957). On the mechanism by which stones in till become oriented. In: *American Journal of Science* 255:194–205.

Grant, J.A. (1986). The Isocon Diagram A Simple Solution to Gresens Equation for Metasomatic Alteration. In: *Economic Geology* 81:1976–1982.

Graup, G. (1977). Die Petrographie der kristallinen Gesteine. In: *Geologica Bavarica* 75:219–230.

Graup, G. (1981). Terrestrial chondrules, glass spherules and accretionary lapilli from the suevite, Ries Crater, Germany. In: *Earth and Planetary Science Letters* 55:407–418.

Graup, G. (1999). Carbonate-silicate liquid immiscibility upon impact melting: Ries Crater, Germany. In: *Meteoritics and Planetary Science* 34:425–438.

Gresens, R.L. (1967). Composition-volume relationships of metasomatism. In: *Chemical geology* 2:47–55.

Grieve, R. A. F. et al. (2010). The Evolution of the Onaping Formation at the Sudbury Impact Structure. In: *Meteoritics and Planetary Science* 45.5:759–782.

Grieve, R.A.F. (1975). Petrology and chemistry of the impact melt at Mistastin Lake crater, Labrador. In: *GSA Bulletin* 86:1617–1629.

Grieve, R.A.F. et al. (1996). Shock metamorphism of quartz in nature and experiment: II. Significance in geoscience. In: *Meteoritics and Planetary Science* 31:6–35.

Hartmann, W.K. and G. Neukum (2001). Cratering Chronology and the Evolution of Mars. In: *Space Science Reviews* 96:165–194.

Hecht, L. et al. (2004). Composition of impact melt particles and the effects of post-impact alteration in suevitic rocks at the Yaxopoil-1 drill core, Chicxulub crater, Mexico. In: *Meteoritics and Planetary Science* 39:1169–1186.

Hisada, E. (2004). Clast-size analysis of impact-generated pseudotachylite from Vredefort Dome, South Africa. In: *Journal of Structural Geology* 26:1419–1424.

Hörz, F. (1965). Untersuchungen an Riesgläsern. In: *Beiträge zur Mineralogie und Petrographie* 11:621–661.

Hörz, F. et al. (1983). Bunte Breccia of the Ries: continous deposits of large impact craters. In: *Reviews of Geophysics and Space Physics* 21:1667–1725.

Hüttner, R. and H. Schmidt-Kaler (1999). *Geologische Karte 1:50000 Ries mit Kurzerläuterungen auf der Rückseite*. Tech. rep. Bayerisches Geologisches Landesamt, scale 1:50000, 1 sheet.

Hüttner, R. and H. Schmidt-Kaler (2003). *Meteoritenkrater Nördlinger Ries. Wanderungen in die Erdgeschichte.* 10. München, Pfeil Verlag:144.

Ivanov, B. A. (2005). Numerical modeling of the largest terrestrial meteorite craters. In: *Solar System Research* 39.5:426–456.

Jankowski, B. (1977a). Die Postimpakt-Sedimente in der Forschungsbohrung Nördlingen 1973. In: *Geologica Bavarica* 75:21–36.

Jankowski, B. (1977b). Die gradierte Einheit oberhalb des Suevits der Forschungsbohrung Nördlingen 1973. In: *Geologica Bavarica* 75:155–162.

Jeffery, G.B. (1922). The motion of ellipsoidal particles immersed in a viscous fluid. In: *Proceedings of the Royal Society London* 102:161–179.

Kamata, H. and K. Minura (1983). Flow directions inferred from imbrication in the Handa pyroclastic flow deposit in Japan. In: *Bulletin of Volcanology* 46-3:277–282.

Kaminski, E. and C. Jaupart (1998). The size distribution of pyroclasts and the fragmentation sequence in explosive volcanic eruptions. In: *Journal of Geophysical Research* 103.B12:29,759–29,779.

Kenkmann, T. et al. (2010). Experimental impact cratering in sandstone: the effect of pore fluids. In: *Proceedings of the 11th Hypervelocity Impact Symposium* 97:18 pages.

Ketcham, R.A. and W.D. Carlson (2001). Acquisition, optimization and interpretation of X-ray computed tomographic imagery: applications to the geosciences. In: *Computers and Geosciences* 27:381–400.

Koeberl, C. et al. (2002). High-resolution X-ray computed tomography of impactites. In: *Journal of Geophysical Research* 107.E10:19–1–19–9.

Koeberl, C. et al. (2007). Uppermost impact fallback layer in the Bosumtwi crater (Ghana): Mineralogy, geochemistry, and comparison with Ivory Coast tektites. In: *Meteoritics and Planetary Science* 42.4/5:709–729.

Kokelaar, P. and C. Romagnoli (1995). Sector collapse, sedimentation and clast population evolution at an active island-arc volcano: Stromboli, Italy. In: *Bulletin of Volcanology* 57:240–262.

Kring, D. A. (2005). Hypervelocity collisions into continental crust composed of sediments and an underlying crystalline basement: comparing the Ries (24 km) and Chicxulub (180 km) impact craters. In: *Chemie der Erde* 65:1–46.

Launeau, P. and P.-Y.F. Robin (2005). Determination of fabric and strain ellipsoids from measured sectional ellipses - implementation and applications. In: *Journal of Structural Geology* 27:2223–2233.

Major, J.J. (1998). Pebble orientation on large, experimental debris-flow deposits. In: *Sedimentary Geology* 117:151–164.

Martelli, G. et al. (1994). Catastrophic disruption experiments: recent results. In: *Planetary and Space Science* 42:1013–1026.

Melosh, H.J. (1989). *Impact cratering: A geologic process*. 11. Oxford Monographs on Geology and Geophysics, New York, Oxford University Press:253.

Meyer, C. et al. (2011). Shock experiments in support of the Lithopanspermia theory: The influence of host rock composition, temperature and shock pressure on the survival rate of endolithic and epilithic microorganisms. In: *Meteoritics and Planetary Science* 46.5:701–718.

Mileikowsky, C. et al. (2000). Natural transfer of viable microorganisms in space, part 1: from Mars to Earth and Earth to Mars. In: *Icarus* 145:391–427.

Moore, J. G.and Sisson T. W. (1981). "The 1980 eruptions of Mount St. Helens, Washington". In: ed. by P.W. Lipman and D.R. Mullineux. Chap. Deposits and effects of the may 18 pyroclastic surge:421–438.

Morgan, J. W. et al. (1979). Ries impact crater, southern Germany: Search for meteoritical material. In: *Geochimica and Cosmochimica Acta* 43:803–815.

Morris, W.A. et al. (2007). Clast fabric examination of impact-generated breccias, borehole LB-07A, Bosumtwi, Ghana. In: *Meteoritics and Planetary Science* 42:769–778.

Muttik, N. et al. (2008). Post-impact alteration of surficial suevites in Ries crater, Germany: Hydrothermal modification or weathering processes? In: *Meteoritics and Planetary Science* 43.11:1827–1840.

Nesbitt, H.W. and G.M. Young (1984). Prediction of some weathering trends of plutonic and volcanic rocks based on thermodynamic and kinetic considerations. In: *Geochimica and Cosmochimica Acta* 48:1523–1534.

Newsom, H. E. (1980). Hydrothermal Alteration of Impact Melt Sheets with Implications for Mars. In: *Icarus* 44:207–216.

Newsom, H. E. et al. (1990). The formation of the Ries crater, West Germany: Evidence of atmospheric interactions during a large cratering event. In: *Global Catastrophes in Earth History, Geological Society of America, Special Paper* 247:195–206.

Newsom, H.E. et al. (1986). Fluidization and hydrothermal alteration of the suevite deposit at the Ries crater, West Germany, and implications for Mars. In: *Journal of Geophysical Research* 91:E239–E251.

O'Connor, A. et al. (2009). WinDICOM: A program for determining inclusion shape and orientation. In: *Computers and Geosciences* 35:1358–1368.

Osinski, G. R. (2005). Hydrothermal activity associated with the Ries impact event, Germany. In: *Geofluids* 5:202–220.

Osinski, G.R. et al. (2004). The nature of the groundmass of surficial suevite from the Ries impact structure, Germany, and constrains on its origin. In: *Meteoritics and Planetary Science* 39:1655–1683.

Osinski, G.R. et al. (2005). Geological overview and cratering model for the Haughton impact structure, Devon Island, Canadian High Arctic. In: *Meteoritics and Planetary Science* 40:1759–1776.

Pierazzo, E. and H.J. Melosh (2000). Hydrocode modeling of oblique impacts: The fate of the projectile. In: *Meteoritics and Planetary Science* 35:117–130.

Pierazzo, E. et al. (1998). Hydrocode simulation of the Chicxulub impact event and the production of climatically active gases. In: *Journal of Geophysical Research* 103:28607–28626.

Pohl, J. et al. (1977). "Impact and Explosion Cratering". In: ed. by D.J. Roddy et al. Pergamon Press, New York. Chap. The Ries impact crater:343–404.

Pohl, J. et al. (2010). "Ries Crater, Germany: The Enkingen magnetic anomaly and associated drill core SUBO 18". In: *Large meteorite Impacts and Planetary Evolution IV*. Vol. 465. Geological Society of America Special Paper:141–163.

Ramsay, J.G. (2003 (original 1967)). *Folding and fracturing of rocks*. Caldwell, Blackburn Press:568.

Ray, S. K. (1999). Transformation of cataclastically deformed rocks to pseudotachylyte by pervasion of frictional melt: inferences from clast-size analysis. In: *Tectonophysics* 301:283–304.

Reimold, W. U. et al. (2009). Petrographic observations on the Exmore breccia, ICDP-USGS drilling at Eyreville, Chesapeake Bay impact structure, USA. In: *Geological Society of America Special Paper* 458:655–698.

Robin, P.-Y.F. (2002). Determination of fabric strain ellipsoids from measured sectional ellipses - theory. In: *Journal of Structural Geology* 24:531–544.

Ross, G. S. and R.L. Smith (1961). Ash flow tuffs, their origin, geological relations and identification. In: *US Geological Survey professional Paper* 366:1–77.

Rousell, D.H. et al. (2003). Sudbury Breccia (Canada): a product of the 1850 Ma Sudbury Event and host to footwall Cu-Ni-PGE deposits. In: *Earth-Science Reviews* 60:147–174.

Rusnak, G.A. (1957). A fabric and petrologic study of the Pleasantview sandstone. In: *Journal of Sedimentary Petrology* 27:41–55.

Schmid, B. (2009). *ImageJ 3D viewer*. URL: `http://rsb.info.nih.gov/ij/plugins/3d-viewer/`.

Schmincke, H.U. and D.L. Swanson (1967). Laminar viscous flowage structures in ash flow tuffs from Gran Canaria, Canary Islands. In: *Journal of Geology* 75:641–664.

Schultz, P. H. (1987). Experimental planetary impact research. In: *International Journal of Impact Engineering* 5:569–576.

Seaman, S.J. and M.L. Williams (1992). Center-to-center analysis and flow fabric characterization in ash-flow tuffs. In: *Bulletin of Volcanology* 54:319–328.

Sparks, R. S. J. and G. P. L. Walker (1973). Products of ignimbrite eruptions. In: *Geology* 1:115–118.

Sparks, R. S. J. et al. (1999). Dense welding caused by volatile resorption. In: *Journal of the Geological Society London* 156:217–225.

Stähle, V. (1972). Impact glasses from the suevite of the Nördlinger Ries. In: *Earth and Planetary Science Letters* 17:275–293.

Stähle, V. and J. Ottemann (1977). Ries-Forschungsbohrung 1973: Zeolithisierung der Gläser im Suevit und Petrographie der Beckensuevite und Gangbreccien. In: *Geologica Bavarica* 75:191–217.

Stevenson, D. J. (1987). Origin of the Moon. The collision hypothesis. In: *Annual Reviews Earth Planetary Science* 15:271–315.

Stöffler, D. (1975). Ries crater breccias and planetary impact formations. In: *Fortschritte der Mineralogie, Special Issue IMA-Papers, 9th Meeting* 52:385–387.

Stöffler, D. (1977). Research drilling, Nördlingen 1973: Polymict breccias, crater basement, and cratering model of the Ries impact structure. In: *Geologica Bavarica* 75:443–458.

Stöffler, D. and R. A. F. Grieve (2007). "Metamorphic Rocks: A Classification and Glossary of Terms". In: ed. by D. Fettes and J. Desmons. Recommendations of the International Union of Geological Sciences, Cambridge University Press, Cambridge, UK. Chap. Impactites, Chapter 2.11:82–242.

Stöffler, D. and F. Langenhorst (1994). Shock metamorphism of quartz in nature and experiment: I. Basic observation and theory. In: *Meteoritics and Planetary Science* 29:155–181.

Stöffler, D. and R. Ostertag (1983). The Ries impact crater. In: *Fortschritte der Mineralogie* 61.2:71–116.

Stöffler, D. et al. (1977). Research drilling Nördlingen 1973 (Ries): Composition and texture of polymict impact breccias. In: *Geologica Bavarica* 75:163–189.

Stöffler, D. et al. (2002). Modeling the Ries-Steinheim impact event and the formation of the moldavite strewn field. In: *Meteoritics and Planetary Science* 37:1893–1907.

Stöffler, D. et al. (2004). Origin and emplacement of the impact formations at Chicxulub, Mexico, as revealed by the ICDP deep drilling at Yaxcopoil-1 and by numerical modeling. In: *Meteoritics and Planetary Science* 39.7:1035–1067.

Stöffler, D. et al. (2009). Ries crater and suevite revisited: Part I observations. In: *40th LPSC, Houston*:abstract 1504.

Taddeucci, J. and D. M. Palladino (2002). Particle size-density relationships in pyroclastic deposits: inferences for emplacement processes. In: *Bulletin of Volcanology* 64:273–284.

Tucker, M. (1996). *Methoden der Sedimentologie*. Stuttgart, Enke Verlag:366.

Turcotte, D.L. (1986). Fractals and Fragmentation. In: *Journal of Geophysical Research* 91.B2:1921–1926.

Wittmann, A. (2007). "Formation and emplacement of impactites from drill core Yaxcopoil-1, Chicxulub crater, Mexico". PhD thesis. Humboldt University Berlin.

Wittmann, A. et al. (2004). Impact related dike breccia lithologies in the ICDP drill core Yaxcopoil-1, Chicxulub impact structure Mexico. In: *Meteoritics and Planetary Science* 39:931–954.

Woods, A. W. and K. H. Wohletz (1991). Co-ignimbrite eruption columns. In: *Nature* 350:225–227.

Wünnemann, K. et al. (2005). Is Ries crater typical for its size? An analysis based upon old and new geophysical data and numerical modelling. In: *Geological Society of America Special Paper* 384:67–83.

Wünnemann, S. and B. A. Ivanov (2003). Numerical modelling of the impact crater depth-diameter dependence in an acoustically fluidized target. In: *Planetary and Space Science* 51:831–845.